Theory of Dynamical Processes in Semiconductor Quantum Dots

Thesis by

Yun-Hua Hong

In Partial Fulfillment of the Requirements

for the Degree of

Doctor of Philosophy

California Institute of Technology

Pasadena, California

2017

June 30, 2016

Acknowledgments

Through the journey as a PhD student in Caltech, the time flies faster than I could have imagined. Along the way, there are a lot of things and people for me to be grateful.

First, I am honored to have Prof. Marcus as my advisor. His advices are not limited to the academic guidance, but also from his humbleness and his consideration to others. He is always available to my questions and always very passionate to help me solve the problems.

I would also like to thank the support from my thesis committee, Prof. Miller, Prof. Lewis, and Prof. Wang. I am very thankful to have the inspiring discussions with the former and the current group members, Evans, Kai, Maksym, Nathan, Nima, Sandor, Wei-Chen, and Zhaoyan. Special thanks to Wei-Chen for the generous sharing of his experience and knowledge on science and for being a great friend.

The friendship built within the Association of Caltech Taiwanese (ACT) makes my life in Caltech wonderful, and the Double-Ten tournaments played with the ACT softball team will always be the treasured memory.

My family's unconditional support and love from Taiwan makes the distance seems non-existing. Although my mother, Su-Hsiang, passed away in 2011, she will always be remembered in my heart.

Finally, I would like to express my gratefulness to my wife Alice, who has been a great support in both faith and family. If it were not her companionship along the whole journey, I could not have arrived the destination. I am fortunate to have her and our daughter Priscilla in my life.

Abstract

The focus of this dissertation is on the theory of the electronic dynamical processes in semiconductor quantum dots (QDs). The first part of the dissertation introduces the calculation method of electronic eigenstates used through the dissertation, the sp^3s^* tight-binding (TB) method, and the application of the symmetry-adapted linear combination (SALC) of atomic orbitals to the TB method. The combination of the SALC and TB method reduces the computational load, and generates reliable electronic eigenstates and eigenvalues of Wurtzite CdSe QDs. The second part of the dissertation uses the calculated eigenstates and eigenvalues of CdSe QDs, whose band gap states are removed by a passivation layer, to calculate various kinds of physical properties, such as the structure, the permanent dipole moment, the band gap, the molecular orbitals, the density of states (DOS), and the absorption spectrum. These calculated results are compared with the respective experimental measurements in further discussions. The last part of the dissertation focuses on the studies of the size-dependent trend of the Auger electron-hole recombination process that causes the semiconductor QDs to remain in the dark state, including the cases of a negative trion, a positive trion, and a biexciton, in semiconductor QDs. The rates of these Auger processes are expressed in the form of Fermi's golden rule, where the Coulombic interaction between the two electrons is the operator. Although the calculated results shows larger size dependence than that of the experimental findings, the literature of recent experiments and theories points out potential remedies to the discrepancy by modifying the current computational setting and theory in the dissertation.

Contents

List of Figures

List of Tables

Chapter 1

Introduction

Background

Semiconductor quantum dots (QDs), also known as nanocrystals (NCs), have attracted great attention both in academia and industry. They have opened a new perspective for studying the physics and chemistry of the materials whose scale of size, ranging from several tens to several tens thousand of atoms,[1] is between that of bulk semiconductors and molecules.[2] Semiconductor QDs show properties distinctly different from those of bulk semiconductors, including their adjustable band gaps and their corresponding optical properties, namely, the absorption and fluorescence spectra[2-3], the sparse and discrete energy levels[2, 4], and a large surface-to-volume ratio[5]. The adjustable optical properties provide potential applications to optoelectronic devices, such as light-emitting diodes (LED)[6,7,8], solar cells[9,10,11], and labeling or imaging for biological applications,[12,13] while the large surface area permits QDs to act as the carrier of active ligands for probing purposes[14,15] or catalysts[16].

However, it has been observed that the photoluminescence (PL) signal of semiconductor QDs under photo-excitation is not a stable and predictable response[17], and this unpredictability limits the semiconductor QDs' capability for optical applications[18]. A feature of this phenomenon is that while a QD is being steadily illuminated by light, the intensity of its fluorescence ranges from no detectable photons to several photons in a single time interval of measurement and, moreover, the distribution of duration of the light-dark time periods for the QD follows a power law. This phenomenon is referred to as “fluorescence intermittency” (or “blinking”)[18], and the temporal record of the fluorescence intensity is usually referred to as a “trajectory”. Typically, some value of the fluorescence light intensity is assigned as the threshold, for describing the fluorescent event as coming from a “light state” (an “ON” state) when the fluorescent intensity is higher than that threshold or as coming from a “dark state” (an “OFF” state) when the fluorescent intensity is below the specified threshold[19]. The “blinking” is attributed to an Auger process.[20,21,22]

A striking property of the fluorescence intermittency is that in the studies of many different kinds of semiconductor QDs[23,24,25], the distribution of the probability for different time periods of the light (or dark) states has the form of power law. The power is the slope of $\log\left(-dP(t)/dt\right)$ versus $\log(t)$, where P(t) is the survival probability. The power is typically about -3/2 for both light and dark state distribution over some decades of time (as much as 5 decades for the dark state)[17,26], but truncated by an exponential tail in the case of the light state distribution[17]. This high similarity across materials indicates that there should be a universal explanation accountable for the observations[26].

Although the suppression of “blinking”, or even non-blinking QDs[27], has been achieved via different techniques[28-29], understanding the physics behind the Auger process is an interesting topic, especially the type of Auger process that is responsible for the well-known intermittent fluorescence behavior of these quantum dots. This process is an Auger process[20, 30] in which, as one example, the interaction two excited electrons provides a nonradiative alternative to fluorescence, for example by causing an electron-hole recombination while the other electron is excited to a high-energy state in order to satisfy energy conservation (an Auger process). Such a quantum dot is then dark rather than bright (fluorescent). The focus of the present dissertation is on the dependence of these Auger processes on the size of the quantum dot. A previous existing calculation of this dependence for CdSe QDs is by Vaxenburg *et al.*[31]. It employs a non-atomistic effective mass method, while in the present dissertation an atomistic method, tight-binding (TB) method, is employed. Comparison is made both with these results and with the experiments[32,33] and with the results for other semiconductor QD materials, as described in Table 1.1.

Role of the Auger Process in Fluorescence Intermittency

Although there is still some debate on the detailed steps of how the fluorescence intermittency (blinking) occurs within semiconductor QDs[34,21], it is widely believed that the non-radiative Auger process plays an important role in the conversion of light to dark states and vice versa.[30] In this process an electron-hole exciton interacts with a third particle, such as an electron (negative trion) or a hole (positive trion), or another exciton (biexciton). In the first two cases the QD has been charged by losing an electron or hole[18, 20] to a surface state[34,21] or to the surroundings[20, 35]. The Auger process is governed by the Coulombic interaction[36] between the various excited electrons and has a matrix element of the type

$$M_{Auger}=\int\int \psi_1^*(\boldsymbol{r}_1)\psi_2^*(\boldsymbol{r}_2)\frac{1}{\epsilon|\boldsymbol{r}_1-\boldsymbol{r}_2|}\psi'_1(\boldsymbol{r}_1)\psi'_2(\boldsymbol{r}_2)\,d\boldsymbol{r}_1 d\boldsymbol{r}_2 \quad , \tag{1}$$

where the Ψs represent the initial states of electron (or hole) while Ψ's represent the final states after the interaction and ε is the dielectric constant. Compared with the bulk semiconductor, the rate of Auger process is enhanced in QDs because the confined volume increases the overlap between the quasi-particles and hence increases the magnitude of the matrix element, M_{Auger}, in Eq. (1). This volume-related effect, called "quantum confinement"[2], is significantly enhanced when the size of a QD is smaller than the Bohr radius of an exciton in the semiconductor.

Efros and Rosen[20] pointed out that if an electron or hole has been ejected or trapped by an excitation of the QD, the next excitation by the light would produce a total of three particles (electrons and holes). In that case, instead of fluorescing the excited state of the QD can decay by a rapid (radiationless) Auger process and so QD is then "dark" when the decay rate is faster than the fluorescence rate, for example, when the three quasi-particles are two electrons in the CB and one hole in the VB, and an electron and the hole can recombine and hence not fluoresce, while the third particle, an electron, is excited to a high energy state in the CB, in order that energy conservation is obeyed, and even in some cases to a high enough energy state that it is ejected from the QD ("ionization").

One form of the Auger processes that was proposed by Frantsuzov and Marcus[30, 37] was the formation of a negative trion to account for the transition from a light state to a dark state. Using CdSe as an example, when an electron in the conduction band (CB) is generated by photoexcitation in a QD, there is a chance that the electron from an unpassivated Se^{2-} atom (at the surface of the QD) will fill the hole left in the valence band (VB) by the photoexcitation, so forming a trapped hole (Se^{-}) at the surface, while a CB electron in the state near the edge of the CB (the $1S_e$ state) is excited resonantly to the $1P_e$ state, approximately 0.3 eV[37-38] above the $1S_e$ state, and then relax to $1S_e$ state to complete this "trapping" process. The electron-electron interaction occurs via Coulombic interaction. The excited electron will relax to the $1S_e$ state to complete the dark cycle.

The light state can be restored by an Auger-based "detrapping" process, in which an electron of a subsequent photo-excitation that produces another exciton that recombines with the hole trapped in the Se^-, and the third particle (an electron) in the CB is then excited to a higher CB state by accepting the recombination energy. It then relaxes to the $1S_e$ state.[30] There are other possible mechanisms to account for the restoration process[34, 39], and further experimental verification might be needed, but these other processes will not be commented on in this dissertation since the restoration is not the main focus of the thesis.

Role that the Auger Process Plays in the Exponential Tail

The most significant difference between the power law of the light states and the dark states is that while both have a slope of -3/2 (approximate), the dark state having it over a wide time range of the off-times, the -3/2 slope of the linear regime for the on-time distribution truncated by an exponential tail, and the time for the onset of the tail is shorter at higher excitation intensities and at higher temperatures[17-19, 40]. In Tang and Marcus' diffusion-controlled electron transfer (DCET) model[41-42], both the on and the off transition were of the resonant type. The -3/2 slope for both the "on-time" and "off-time" distributions was successfully reproduced, as well as an exponential tail for the light state, but the tail did not have the above asymmetry for the light and dark states. Kuno *et al.*[24, 43] also provided another explanation to the log-log slope over several decades of time. Their model was capable of generating the constant slopes over several decades of time for both a light and a dark state[43], but the setting of the model didn't satisfy all the experimental constraints[26], and the absolute values of the slope lacked the comparability to the slopes in the experiments[43].

A subsequent study by Zhu and Marcus[44] remedied this situation by modifying the DCET model[41-42]. Experimentally it was demonstrated by Peterson and Nesbitt[45] that the onset of the exponential tail increases with the square of the incident light intensity, so suggesting a role for biexciton as the source of the exponential tail, a dark state being formed by the interaction of two excitons. In the reaction-diffusion differential equation formalism of Zhu and Marcus for light state distribution when a biexciton is formed (higher light intensity), one electron in the CB now acquires by an Auger process such a high energy (one band gap above the CB edge), that it may be ejected from the QD via a Fermi Golden Rule process instead of being involved in a resonant process, thus giving rise to an additional channel that leads to an exponential decay. In the dark state, the probability of forming a biexciton is small because the fast Auger-based recombination in the dark state keeps the biexciton concentration to a minimum, and so no exponential tail occurs in the dark state. Zhu and Marcus' conclusions are: (1) for dark states, the recombination of an electron-hole pair via a biexciton still keeps the system in the dark state, so the change on the exitons doesn't have a significant effect on the system, and (2) for light states, high incident light intensity leads to a high concentration of biexcitons that produces by an Auger process a highly excited electron from the core of the QD via a Fermi Golden Rule process and so leads to the exponential tail for the light state, instead of the usual resonant transition to form a dark state to a light state.

To summarize this discussion, Auger processes play an important role in the switching of the QD between light and dark states and in explaining why the light state has an exponential tail to the linear log-log time-distribution plots while a dark state does not.

Size-dependence of the Auger process in Semiconductor QDs

Since Auger processes play an important role in semiconductor QDs, and have high correlation with the size-dependent volume confinement, understanding the size-dependence of Auger process is of particular interest. Recently there have been measurements of size-dependence of the lifetime of an Auger process for CdSe[32], ZnO[46], and CdS[47] QDs. For QDs with a radius of 1 nm to 5 nm, the log-log plot of the size dependence of these measured Auger lifetimes has shown a linear dependence with a slope ranging from 2 to 4.3 for negative trions and from 2.5 to 3.1 for biexcitons. A summary is given in Table 1.1.

Part Theoretical Studies of the Auger Process in semiconductor QDs

Besides the DCET model and other dynamic models[34,48] that account for the fluorescent intermittency, theoretical studies of QDs that implement electronic structure calculations have attracted more attention since the 1980s. The calculation methods include the wave-like approach, such as the effective-mass approximation (EMA)[38-49], and atomistic approaches, such as the TB method[50,51,52], the pseudopotential method[53-54], and density functional theory (DFT)[55].

These theoretical studies have been made for QDs of different elements, including Si[56,57], CdSe[38, 58], CdS[51, 59], ZnS[51], PbSe[60], and many composites[58]. In this dissertation, the TB method is chosen among the theoretical methods above as a tool to calculate the electronic structure of semiconductor QDs. The details of the method are discussed in Chapter 2. There is existing literature on TB calculations on QDs of various chemical elements, and the QD radius in those studies ranges from 1 nm up to 4 nm. The calculations in the literature have shown that the TB method is capable of yielding various theoretical studies, including (1) the optical properties of QDs, e.g. band gap[51-52, 61] and absorption spectrum[62,63], (2) the electronic properties, e.g. density of state (DOS) and molecular orbitals (MOs) of QDs[64,65], and (3) the size dependence of the rate constants of Auger process, such as those involving a negative trion[57, 66] or a positive trion[57, 66].

The results from these theoretical studies have shown that with proper modification of the details of those computational methods previously used for either bulk semiconductors or molecules, they can be used to probe the mechanism of the Auger process in semiconductor QDs.

Reference

1. Hill, N. A.; Whaley, K. B., A theoretical study of the influence of the surface on the electronic structure of CdSe nanoclusters. *J Chem Phys* **1994,** *100* (4), 2831-2837.
2. Alivisatos, A. P., Semiconductor Clusters, Nanocrystals, and Quantum Dots. *Science* **1996,** *271* (5251), 933-937.
3. Reiss, P.; Protière, M.; Li, L., Core/Shell Semiconductor Nanocrystals. *Small* **2009,** *5* (2), 154-168.
4. Liljeroth, P.; Jdira, L.; Overgaag, K.; Grandidier, B.; Speller, S.; Vanmaekelbergh, D., Can scanning tunnelling spectroscopy measure the density of states of semiconductor quantum dots? *Phys Chem Chem Phys* **2006,** *8* (33), 3845-3850.
5. Ladizhansky, V.; Hodes, G.; Vega, S., Surface Properties of Precipitated CdS Nanoparticles Studied by NMR. *J. Phys. Chem. B* **1998,** *102* (43), 8505-8509.
6. Zhao, J.; Bardecker, J. A.; Munro, A. M.; Liu, M. S.; Niu, Y.; Ding, I. K.; Luo, J.; Chen, B.; Jen, A. K. Y.; Ginger, D. S., Efficient CdSe/CdS Quantum Dot Light-Emitting Diodes Using a Thermally Polymerized Hole Transport Layer. *Nano Lett* **2006,** *6* (3), 463-467.
7. Anikeeva, P. O.; Halpert, J. E.; Bawendi, M. G.; Bulović, V., Quantum Dot Light-Emitting Devices with Electroluminescence Tunable over the Entire Visible Spectrum. *Nano Lett* **2009,** *9* (7), 2532-2536.
8. Caruge, J. M.; Halpert, J. E.; Wood, V.; Bulovic, V.; Bawendi, M. G., Colloidal quantum-dot light-emitting diodes with metal-oxide charge transport layers. *Nat Photon* **2008,** *2* (4), 247-250.
9. Nozik, A. J., Quantum dot solar cells. *Phys. E: Low-dimensional Systems and Nanostructures* **2002,** *14* (1–2), 115-120.
10. Semonin, O. E.; Luther, J. M.; Choi, S.; Chen, H.-Y.; Gao, J.; Nozik, A. J.; Beard, M. C., Peak External Photocurrent Quantum Efficiency Exceeding 100% via MEG in a Quantum Dot Solar Cell. *Science* **2011,** *334* (6062), 1530-1533.
11. Grätzel, M., Dye-sensitized solar cells. *Journal of Photochemistry and Photobiology C: Photochemistry Reviews* **2003,** *4* (2), 145-153.
12. Mattoussi, H.; Mauro, J. M.; Goldman, E. R.; Anderson, G. P.; Sundar, V. C.; Mikulec, F. V.; Bawendi, M. G., Self-Assembly of CdSe−ZnS Quantum Dot Bioconjugates Using an Engineered Recombinant Protein. *J Am Chem Soc* **2000,** *122* (49), 12142-12150.
13. Medintz, I. L.; Uyeda, H. T.; Goldman, E. R.; Mattoussi, H., Quantum dot bioconjugates for imaging, labelling and sensing. *Nat Mater* **2005,** *4* (6), 435-446.
14. Mattoussi, H.; Palui, G.; Na, H. B., Luminescent quantum dots as platforms for probing in vitro and in vivo biological processes. *Adv Drug Deliver Rev* **2012,** *64* (2), 138-166.
15. Jin, W. J.; Costa-Fernández, J. M.; Pereiro, R.; Sanz-Medel, A., Surface-modified CdSe quantum dots as luminescent probes for cyanide determination. *Anal Chim Acta* **2004,** *522* (1), 1-8.
16. Senevirathna, M. K. I.; Pitigala, P. K. D. D. P.; Tennakone, K., Water photoreduction with Cu2O quantum dots on TiO2 nano-particles. *Journal of Photochemistry and Photobiology A: Chemistry* **2005,** *171* (3), 257-259.
17. Shimizu, K. T.; Neuhauser, R. G.; Leatherdale, C. A.; Empedocles, S. A.; Woo, W.

K.; Bawendi, M. G., Blinking statistics in single semiconductor nanocrystal quantum dots. *Phys Rev B* **2001,** *63* (20).

18. Nirmal, M.; Dabbousi, B. O.; Bawendi, M. G.; Macklin, J. J.; Trautman, J. K.; Harris, T. D.; Brus, L. E., Fluorescence intermittency in single cadmium selenide nanocrystals. *Nature* **1996,** *383* (6603), 802-804.
19. Kuno, M.; Fromm, D. P.; Hamann, H. F.; Gallagher, A.; Nesbitt, D. J., Nonexponential "blinking" kinetics of single CdSe quantum dots: A universal power law behavior. *J Chem Phys* **2000,** *112* (7), 3117-3120.
20. Efros, A. L.; Rosen, M., Random telegraph signal in the photoluminescence intensity of a single quantum dot. *Phys Rev Lett* **1997,** *78* (6), 1110-1113.
21. Galland, C.; Ghosh, Y.; Steinbruck, A.; Sykora, M.; Hollingsworth, J. A.; Klimov, V. I.; Htoon, H., Two types of luminescence blinking revealed by spectroelectrochemistry of single quantum dots. *Nature* **2011,** *479* (7372), 203-207.
22. Park, Y.-S.; Bae, W. K.; Pietryga, J. M.; Klimov, V. I., Auger Recombination of Biexcitons and Negative and Positive Trions in Individual Quantum Dots. *Acs Nano* **2014,** *8* (7), 7288-7296.
23. Cui, S.-C.; Tachikawa, T.; Fujitsuka, M.; Majima, T., Interfacial Electron Transfer Dynamics in a Single CdTe Quantum Dot-Pyromellitimide Conjugate. *J Phys Chem C* **2008,** *112* (49), 19625-19634.
24. Kuno, M.; Fromm, D. P.; Hamann, H. F.; Gallagher, A.; Nesbitt, D. J., "On"/"off" fluorescence intermittency of single semiconductor quantum dots. *J Chem Phys* **2001,** *115* (2), 1028-1040.
25. Kuno, M.; Fromm, D. P.; Gallagher, A.; Nesbitt, D. J.; Micic, O. I.; Nozik, A. J., Fluorescence Intermittency in Single InP Quantum Dots. *Nano Lett* **2001,** *1* (10), 557-564.
26. Frantsuzov, P.; Kuno, M.; Jankó, B.; Marcus, R. A., Universal emission intermittency in quantum dots, nanorods and nanowires. *Nat Phys* **2008,** *4* (7), 519-522.
27. Wang, X.; Ren, X.; Kahen, K.; Hahn, M. A.; Rajeswaran, M.; Maccagnano-Zacher, S.; Silcox, J.; Cragg, G. E.; Efros, A. L.; Krauss, T. D., Non-blinking semiconductor nanocrystals. *Nature* **2009,** *459* (7247), 686-689.
28. Yuan, C. T.; Yu, P.; Tang, J., Blinking suppression of colloidal CdSe/ZnS quantum dots by coupling to silver nanoprisms. *Appl Phys Lett* **2009,** *94* (24), 243108.
29. Mahler, B.; Spinicelli, P.; Buil, S.; Quelin, X.; Hermier, J.-P.; Dubertret, B., Towards non-blinking colloidal quantum dots. *Nat Mater* **2008,** *7* (8), 659-664.
30. Marcus, R. A., Interaction of theory and experiment: examples from single molecule studies of nanoparticles. *Philos T R Soc A* **2010,** *368* (1914), 1109-1124.
31. Vaxenburg, R.; Rodina, A.; Shabaev, A.; Lifshitz, E.; Efros, A. L., Nonradiative Auger Recombination in Semiconductor Nanocrystals. *Nano Lett* **2015,** *15* (3), 2092-2098.
32. Cohn, A. W.; Rinehart, J. D.; Schimpf, A. M.; Weaver, A. L.; Gamelin, D. R., Size Dependence of Negative Trion Auger Recombination in Photodoped CdSe Nanocrystals. *Nano Lett* **2014,** *14* (1), 353-358.
33. Robel, I.; Gresback, R.; Kortshagen, U.; Schaller, R. D.; Klimov, V. I., Universal Size-Dependent Trend in Auger Recombination in Direct-Gap and Indirect-Gap Semiconductor Nanocrystals. *Phys Rev Lett* **2009,** *102* (17), 177404.
34. Qin, W.; Guyot-Sionnest, P., Evidence for the Role of Holes in Blinking: Negative and Oxidized CdSe/CdS Dots. *Acs Nano* **2012,** *6* (10), 9125-9132.

35. Chepic, D. I.; Efros, A. L.; Ekimov, A. I.; Vanov, M. G.; Kharchenko, V. A.; Kudriavtsev, I. A.; Yazeva, T. V., Auger Ionization of Semiconductor Quantum Drops in a Glass Matrix. *J Lumin* **1990,** *47* (3), 113-127.
36. Landau, L. D.; Lifshits, E. M., *Quantum mechanics: non-relativistic theory.* 2d ed.; Pergamon Press; sole distributors in the U.S.A., Addison-Wesley Pub. Co., Reading, Mass.: Oxford, New York,, 1965; p xiii, 616 p.
37. Frantsuzov, P. A.; Marcus, R. A., Explanation of quantum dot blinking without the long-lived trap hypothesis. *Phys Rev B* **2005,** *72* (15).
38. Efros, A. L.; Rosen, M., The electronic structure of semiconductor nanocrystals. *Annu Rev Mater Sci* **2000,** *30*, 475-521.
39. Zhao, J.; Nair, G.; Fisher, B. R.; Bawendi, M. G., Challenge to the Charging Model of Semiconductor-Nanocrystal Fluorescence Intermittency from Off-State Quantum Yields and Multiexciton Blinking. *Phys Rev Lett* **2010,** *104* (15).
40. Nirmal, M.; Brus, L., Luminescence Photophysics in Semiconductor Nanocrystals. *Accounts Chem Res* **1998,** *32* (5), 407-414.
41. Tang, J.; Marcus, R. A., Diffusion-controlled electron transfer processes and power-law statistics of fluorescence intermittency of nanoparticles. *Phys Rev Lett* **2005,** *95* (10).
42. Tang, J.; Marcus, R. A., Mechanisms of fluorescence blinking in semiconductor nanocrystal quantum dots. *J Chem Phys* **2005,** *123* (5).
43. Kuno, M.; Fromm, D. P.; Johnson, S. T.; Gallagher, A.; Nesbitt, D. J., Modeling distributed kinetics in isolated semiconductor quantum dots. *Phys Rev B* **2003,** *67* (12).
44. Zhu, Z.; Marcus, R. A., Extension of the diffusion controlled electron transfer theory for intermittent fluorescence of quantum dots: inclusion of biexcitons and the difference of "on" and "off" time distributions. *Phys Chem Chem Phys* **2014,** *16* (47), 25694-25700.
45. Peterson, J. J.; Nesbitt, D. J., Modified Power Law Behavior in Quantum Dot Blinking: A Novel Role for Biexcitons and Auger Ionization. *Nano Lett* **2009,** *9* (1), 338-345.
46. Cohn, A. W.; Schimpf, A. M.; Gunthardt, C. E.; Gamelin, D. R., Size-Dependent Trap-Assisted Auger Recombination in Semiconductor Nanocrystals. *Nano Lett* **2013,** *13* (4), 1810-1815.
47. Kobayashi, Y.; Nishimura, T.; Yamaguchi, H.; Tamai, N., Effect of Surface Defects on Auger Recombination in Colloidal CdS Quantum Dots. *The Journal of Physical Chemistry Letters* **2011,** *2* (9), 1051-1055.
48. Frantsuzov, P. A.; Volkán-Kacsó, S.; Jankó, B., Universality of the Fluorescence Intermittency in Nanoscale Systems: Experiment and Theory. *Nano Lett* **2012,** *13* (2), 402-408.
49. Muto, T., Effective mass approximation in the band theory. *Proceedings of the Institute of Natural Sciences, Nihon University* **1968,** (4), 1-46.
50. Vogl, P.; Hjalmarson, H. P.; Dow, J. D., A Semi-Empirical Tight-Binding Theory of the Electronic-Structure of Semiconductors. *J Phys Chem Solids* **1983,** *44* (5), 365-378.
51. Lippens, P. E.; Lannoo, M., Calculation of the band gap for small CdS and ZnS crystallites. *Phys Rev B* **1989,** *39* (15), 10935.
52. Lippens, P. E.; Lannoo, M., Comparison between Calculated and Experimental Values of the Lowest Excited Electronic State of Small Cdse Crystallites. *Phys Rev B*

1990, *41* (9), 6079-6081.
53. Califano, M.; Franceschetti, A.; Zunger, A., Lifetime and polarization of the radiative decay of excitons, biexcitons, and trions in CdSe nanocrystal quantum dots. *Phys Rev B* **2007,** *75* (11).
54. Wang, L.-W.; Califano, M.; Zunger, A.; Franceschetti, A., Pseudopotential Theory of Auger Processes in CdSe Quantum Dots. *Phys Rev Lett* **2003,** *91* (5).
55. Voznyy, O.; Sargent, E. H., Atomistic Model of Fluorescence Intermittency of Colloidal Quantum Dots. *Physical Review Letters* **2014,** *112* (15), 157401.
56. Martin, E.; Delerue, C.; Allan, G.; Lannoo, M., Theory of excitonic exchange splitting and optical Stokes shift in silicon nanocrystallites: Application to porous silicon. *Phys Rev B* **1994,** *50* (24), 18258-18267.
57. Delerue, C.; Lannoo, M.; Allan, G.; Martin, E.; Mihalcescu, I.; Vial, J. C.; Romestain, R.; Muller, F.; Bsiesy, A., Auger and Coulomb Charging Effects in Semiconductor Nanocrystallites. *Phys Rev Lett* **1995,** *75* (11), 2228-2231.
58. Kobayashi, A.; Sankey, O. F.; Volz, S. M.; Dow, J. D., Semiempirical Tight-Binding Band Structures of Wurtzite Semiconductors - AlN, CdS, CdSe, ZnS, and ZnO. *Phys Rev B* **1983,** *28* (2), 935-945.
59. Efros, A., Auger Processes in Nanosize Semiconductor Crystals. *arXiv preprint cond-mat/0204437* **2002**.
60. Allan, G.; Delerue, C., Confinement effects in PbSe quantum wells and nanocrystals. *Phys Rev B* **2004,** *70* (24), 245321.
61. Albe, V.; Jouanin, C.; Bertho, D., Confinement and shape effects on the optical spectra of small CdSe nanocrystals. *Phys Rev B* **1998,** *58* (8), 4713-4720.
62. Pokrant, S.; Whaley, K., Tight-binding studies of surface effects on electronic structure of CdSe nanocrystals: the role of organic ligands, surface reconstruction, and inorganic capping shells. *Eur Phys J D -Atomic, Molecular, Optical and Plasma Physics* **1999,** *6* (2), 255-267.
63. Ramaniah, L. M.; Nair, S. V., Optical absorption in semiconductor quantum dots: A tight-binding approach. *Phys Rev B* **1993,** *47* (12), 7132.
64. Schulz, S.; Czycholl, G., Tight-binding model for semiconductor nanostructures. *Phys Rev B* **2005,** *72* (16).
65. Baer, N.; Schulz, S.; Schumacher, S.; Gartner, P.; Czycholl, G.; Jahnke, F., Optical properties of self-organized wurtzite InN⁄GaN quantum dots: A combined atomistic tight-binding and full configuration interaction calculation. *Appl Phys Lett* **2005,** *87* (23), 231114.
66. Lannoo, M.; Delerue, C.; Allan, G., Theory of radiative and nonradiative transitions for semiconductor nanocrystals. *J Lumin* **1996,** *70* (1–6), 170-184.
67. Jha, P. P.; Guyot-Sionnest, P., Trion Decay in Colloidal Quantum Dots. *Acs Nano* **2009,** *3* (4), 1011-1015.
68. Achermann, M.; Hollingsworth, J. A.; Klimov, V. I., Multiexcitons confined within a subexcitonic volume: Spectroscopic and dynamical signatures of neutral and charged biexcitons in ultrasmall semiconductor nanocrystals. *Phys Rev B* **2003,** *68* (24), 245302.
69. Qin, W.; Liu, H.; Guyot-Sionnest, P., Small Bright Charged Colloidal Quantum Dots. *Acs Nano* **2014,** *8* (1), 283-291.
70. Fisher, B.; Caruge, J.-M.; Chan, Y.-T.; Halpert, J.; Bawendi, M. G., Multiexciton fluorescence from semiconductor nanocrystals. *Chem Phys* **2005,** *318* (1–2), 71-81.

Table 1.1 Summary of the Existing Literature of Experiments on the Log-Log Slope of Auger Lifetimes in QDs

	Semiconductor	Slope of Auger Lifetime	$R_{core}/R_{core+shell}$	Reference
Negative Trion	CdSe/ZnS	4.3 (colloidal)	Not given	Cohn *et al.*[32]
	ZnO	2 (colloidal)	Not given	Cohn *et al.*[46]
	CdSe/CdS	2.6 (colloidal)	0.74 ~ 0.88	Jha & Guyot-Sionnest[67]
Positve Trion	CdSe/ZnS	2.5 (projected)	Not given	Cohn *et al.*[32]
Biexciton	CdSe/CdS	~2.5 (colloidal)	0.74 ~ 0.88	Jha & Guyot-Sionnest[67]
	CdSe	3.1 (colloidal)	0.36 ~ 0.45	Achermann *et al.*[68]
	CdSe/ZnS	3 (colloidal)	Not given	Cohn *et al.*[32]
	CdTe/CdSe	2.5	Not given	Qin *et al.*[69]
	CdSe	3 (colloidal)	Not given	Fisher *et al.*[70]

1. The Auger lifetimes listed above contain different charge states: negative trion, positive trion and biexciton.
2. The slope for the positive trion in the table is projected by using the equation, $1/\tau_A^{XX} = 2/\tau_A^{T^+} + 2/\tau_A^{T^-}$ [54, 67], where XX denotes a biexciton, T^+ denotes a positive trion, and T^- denotes a negative trion.

Chapter 2

Tight-Binding Method for Quantum Dots

Background

As mentioned in the previous chapter, a particularly useful property of semiconductor quantum dots (QDs) is the versatility of their optical properties due to the flexibility in their size, shape and attached organic ligands. The size scale of QDs is usually around a few nanometers, and so is in between that of bulk semiconductor and molecules. It is intuitive therefore to adopt either bulk-based methods or molecule-based methods to study QDs theoretically.

Plane-wave-like methods, such as the effective-mass approximation (EMA)[1] whose wave functions are described by modified plane waves[2], have their own limitation in applications to QDs. For example, for an Auger process involving trapping or detrapping[3] mentioned in the introduction in Chapter 1, a plane-wave-based description may not be the best choice because a localized atomic description for the wave function is required. As mentioned in Chapter 1, the studies using atomistic-based methods have shown the capability of the these theoretical methods. We have chosen to use the atomistic-based tight-binding (TB) method for the calculations.

An advantage of TB method is that the two-electron integrals between electrons on each atomic site are integrated implicitly by entering into simple parameters between neighbors (namely the V's in Table 2.1). Therefore, the Hamiltonian of a QD using the

TB method contains the energy of each atomic orbital (AO), i.e. the E's in Table 2.1, and the interaction between AOs, i.e. the V's, which costs low computational demand but still provides a useful description of the energy diagram[4,5], as in the TB results of the electronic band diagrams in bulk semiconductor[6]. The atomic wave functions for further applications are the eigenstates obtained by directly diagonalizing the Hamiltonian[7].

This chapter will describe how we implement the existing TB method with various modifications to meet our specific needs for treating the Auger process.

Method of Constructing the Quantum Dots

CdSe QDs have two different major crystal structures: Wurtzite (WZ) and zincblende (ZB). Experimental measurement show that CdSe QDs have a large permanent dipole moment[8], confirming that the structure of a CdSe QD is WZ. Even though it has been reported that CdSe QDs with ZB structure can be fabricated with new synthetic methods[9], in this dissertation, WZ is selected as the geometry appropriate for the usual experiments on QDs. For practical use in experiments, inorganic passivation layers of another semiconductor, such as ZnS[10,11,12] or CdS[13], are typically added outside of the bare core QD to eliminate potential surface traps[12] and to confine the excited excitons. QDs with this kind of structure are referred to as core/shell QDs.

There are four atoms, two anions and two cations, in a unit cell of the WZ structure, and their basis vectors are $(0,0,0)$, $(a/\sqrt{3},0,c/2)$, $(a/\sqrt{3},0,c/8)$, and $(0,0,5c/8)$, respectively, where *a* and *c* are the lattice constants.[4] The QDs for the calculation in this dissertation were constructed with alternative layers of cations and anions with an Se as the central atom at the origin. Starting from the central atom, all four cation atoms connecting to it in the next layer was built along the following four basis vectors iteratively, $(a/2,-\sqrt{3}a/6,-c/8)$, $(-a/2,-\sqrt{3}a/6,-c/8)$, $(0,\sqrt{3}a/3,-c/8)$, and $(0,0,3c/8)$, until the desired size was achieved, where a = 4.2999 Å and c = 7.0109 Å for CdSe. Since the major shape of the QDs observed in experiments is ellipsoidal[14], after the above construction, a smaller ellipsoidal QD with the desired aspect ratio and size was cut out from the WZ atom collective. To conserve the charge neutrality in each QD, both locally and globally, the center of the ellipsoid was chosen at the middle of an anion's and a cation's positions, and the total number of anion atoms added to the ellipsoidal QD is equal to the number of anion atoms in both core and shell layers, respectively, in a way that preserves the stoichiometry.

Typically, the semiconductor in the shell layers has different lattice constants (*a* & *c*) from the core semiconductor. To simplify the problem and to focus on the physical property of interest, the geometry (WZ) and the lattice constants for the shell material were assumed the same as those of core semiconductors. That is, the lattice mismatch was also neglected in the core/shell QDs.

Symmetry-adapted Linear Combination of Atomic Wave Functions

Once the spatial positions of each atom in the core/shell QD were determined, the atomic orbitals (AOs) on each atom form the basis set of the wave functions of the whole QD. The WZ structure belongs to the C_{3V} symmetry group w.r.t the c-axis in its crystal structure. The molecular orbitals (MOs) of a QD can be expressed in terms of the combination of the irreducible representations in the group. By using the concept of symmetry-adapted linear combination (SALC) of atomic wave functions, as discussed, for example, by Cotton[15], those irreducible MOs can be constructed from a complete set of AOs with the *complete projection operators* as defined in Cotton's book[15],

$$\hat{P}^{j}_{s't'}=\frac{l_j}{h}\sum_{R}[\Gamma(R)^{j}_{s't'}]^{*}\hat{\boldsymbol{R}} \quad , \tag{1}$$

where l_j is dimension of the j-th irreducible representation, h is the order of the group, $\hat{\boldsymbol{R}}$ is any given operator in the group, and $\Gamma(R)^{j}_{s't'}$ is the matrix element at the s'-th row and t'-th column of the operator **R**.[15] The definition in Eq. (1) can be further simplified using incomplete projection operators, in which $\Gamma(R)^{j}_{s't'}$ is replaced by the character of the operators, $\chi(R)^{j}$. That is,[15]

$$\hat{P}^{j}=\frac{l_j}{h}\sum_{R}\chi(R)^{j}\hat{\boldsymbol{R}} \quad . \tag{2}$$

For the sp^3s^* TB method, the complete set of AOs was formed by the valence s, p and s^* orbitals on cations and anions. By employing the SALC, only 1/6 (namely the fan-shape region between two red solid lines, σ_v and $\sigma_{v''}$, in Fig. 2.1) of the atoms (or AOs) in a QDs are needed, as shown in Fig. 2.1, where the σ_v, $\sigma_{v'}$ and $\sigma_{v''}$ are the reflective planes, and the angle between any of the two planes is 120º. The AOs within the fan-shaped area are used to form the irreducible representation of MOs, which were used to construct the TB Hamiltonian. The atoms in the 1/6 QD were divided into four categories: the symmetry axis, the σ_v plane, the $\sigma_{v'}$ plane, and the fan-shaped region between but not including σ_v and $\sigma_{v'}$. Applying the incomplete projection operators for each irreducible representation to every AO ϕ_i ,

$$\hat{p}^j \phi_i = \frac{l_j}{6} \left(\chi(E)^j \hat{E} + \sum_{k=1,2} \chi(C_3^k)^j \hat{C}_3^k + \sum_{n=1}^{3} \chi(\sigma_{v^n})^j \hat{\sigma}_{v^n} \right) \phi_i \quad . \tag{3}$$

A set of irreducible MOs can be obtained as the basis set for the TB Hamiltonian. The Hamiltonian matrix of the interactions between those MOs can form three block-diagonal matrices because of the orthogonality between different symmetries. The smaller dimension of those block-diagonal matrices reduced the computational loading and time for solving the full TB matrix when doing the matrix diagonalization. The diagonalization of the Hamiltonian matrices through this dissertation were calculated by the software library LAPACK (Linear Algebra Package)[16].

For QDs with C_{3V} symmetry, every eigenstate generated from the Hamiltonian can be categorized by its irreducible representation (A_1, A_2, or E). The categorization helped the identification of the states near the band edge, which are discussed in later chapters.

Parameters for Calculation

The TB parameters used in this dissertation are a set of quantities that include the energy of each AOs on the cation and anion (diagonal terms) and the interactions between each AO (off-diagonal terms). A model with a physically reasonable set of these parameters for the semiconductors, as Vogl *et al.* suggested in their study[5], should have the following properties: (1) the nature of the sp^3 bonding for the elements in those semiconductors is preserved, (2) the choices of the AO energy of the elements should preserve their original relative chemical trend, the properties of the compounds, and the theories of semiconductor with defects, (3) the value of off-diagonal terms scales inversely with the square of the distance between two adjacent atoms,[17,18,19] and (4) a minimum number of parameters, among which only those of the nearest neighbors are considered, should be required to reproduce the band structure, including the valence band states and the edge of the conduction band, of the semiconductor.

Vogl *et al.*[5] introduced an excited *s*-like orbital, *s**, on each atom to the traditional sp^3-basis model. This newly-introduced parameter of excited state better reproduced the band gap of semiconductors with an indirect band gap, such as silicon, by pushing the CB states below it lower in energy and providing a better description of the edge of CB[5]. The high similarity between the calculated band diagram using TB parameters and the band diagram using pseudopotential calculation has shown the validity of the NN description.[5] In Vogl *et al.*'s work[5], a few direct band gap semiconductors, such as GaAs and InAs, were also studied in additional to the indirect band gap semiconductors, and the calculated band diagrams for those direct band gap semiconductor have reasonable agreement with the results obtained using the pseudopotential method. Therefore, the sp^3s^* method is a reliable TB method for both direct and indirect band gap semiconductors, and it was later applied to other direct band gap semiconductors that are popular in the fabrication of QDs, such as CdSe[20,21] and ZnS[7].

There are 13 independent matrix elements in this sp^3s^* method, including 6 diagonal terms, such as the orbital energy of *s*, *p* and s^*, as shown in Table 2.1, and 7 off-diagonal terms, such as the combination of the interaction between the three AOs on adjacent atoms, as shown in Table 2.1.[5] The The diagonal terms were determined by

Hartree-Fock calculations (*s* and *p*) or from spectroscopic data (s^*), while the off-diagonal terms were obtained from the significant band points from the valence band (VB) and CB in the reciprocal space.[3]

Unlike bulk semiconductors, QDs studied in this dissertation preserve partial periodic potential only until the surface is reached, so the Hamiltonian for a single unit cell provided by Vogl *et al.*[5] is not suitable for QDs. For all the atoms in QDs, the knowledge of both the relative position of every atom and its neighbors are necessary to build up a TB Hamiltonian because the connection between any two atoms determines the position of off-diagonal terms in the Hamiltonian. Moreover, the parameters mentioned in the previous paragraph are required, while ¼ of the listed values of *V*'s in Table 2.1 were used for the off-diagonal terms of the atomic interactions because the original values are four times of the atomic interaction.[5]

As can be seen from the phase vectors (g(**k**)) in Vogl *et al.*'s work[5], the orientation of interaction between AOs was defined along the bonds in a zinc blende (ZB) unit cell, and the signs of the parameters therefore determined the orientation of the three *p* orbitals. However, for the Wurtrzite (WZ) structure, it is more symmetrical to define the p_z orbital along the *c*-axis in the WZ unit cell. It generates a set of Euler angles between the two definitions, this definition and the one used by Vogl *et al.*, of the Cartesian coordinates. Throughout this dissertation, the *p* orbitals used, $\{p_i^{WZ}, i=x,y,z\}$, are defined as

$$\begin{pmatrix} p_x^{WZ} \\ p_y^{WZ} \\ p_z^{WZ} \end{pmatrix} = \begin{pmatrix} \frac{-1}{\sqrt{2}} & \frac{1}{\sqrt{2}} & 0 \\ \frac{-1}{\sqrt{6}} & \frac{-1}{\sqrt{6}} & \frac{2}{\sqrt{6}} \\ \frac{1}{\sqrt{3}} & \frac{1}{\sqrt{3}} & \frac{1}{\sqrt{3}} \end{pmatrix} \begin{pmatrix} p_x \\ p_y \\ p_z \end{pmatrix} , \tag{4}$$

where $\{p_i, i=x, y, z\}$ represent the *p* orbitals defined by Vogl *et al.*. Following the definition in Eq. (4), all the off-diagonal terms of interaction between AOs on adjacent atoms need to be re-calculated from those used by Vogl *et al.*. Unlike the original set of matrix[5], the orientations of the bonds on the four atoms in a WZ unit cell are distinct (as provided in Fig. 2.3), and because of the choice of central atom (namely an Se) in this thesis, as mentioned above, Se atoms belong to either orientation 1 or 4 (Fig. 2.3) while Cd atoms belong to either orientation 2 or 3. The corresponding off-diagonal matrices for each orientation can be found from Tables 2.2 to 2.4.

For the convenience for applying the SALC method to the calculation in this dissertation, the Cartesian coordinates in different regions of the QD (Fig. 2.2) are defined accordingly. The only pre-determined Cartesian coordinates are for (1) the atoms in Area I, (2) the atom on the rotational smmetry axis (i.e. the center of the QD), (3) the atoms on the σ_v between Areas I and II, and (4) the atoms on the $\sigma_{v''}$ between Areas I and VI, and their respective coordinates are shown in Fig. 2.2. The off-diagonal matrix in cases (1), (2), and (3) are defined in Table 2.2 while the off-diagonal matrix between the AOs in the fourth case and the AOs in case (1) are defined in Table 2.3. For the coordinates in the rest area, they were determined by applying the symmetry operator to the two pre-determined coordinates. Therefore, for example, the orientation of the *p* orbitals of the atoms on $\sigma_{v'}$ (between Areas IV and V) are obtained by applying the C_3^1 operator on the coordinate on σ_v (between Areas I and II). Therefore, another set of the off-diagonal matrix is needed to describe the interaction of the AOs for the example above, as shown in Table 2.4.

Even though the matrices in Tables 2.2 to 2.4 were originally fitted from semiconductors with a ZB crystal structure, it can be found in the literature[22] that those parameters for ZB were used for the calculations of WZ QDs because the local environment at each atom is approximately the same for both ZB and WZ, especially when only nearest-neighbors are taken into account. Moreover, a calculation[23] using TB method on CdSe QDs has concluded that for the various sizes of QDs they considered, there is no significant difference in the energy levels regardless of whether their crystal structure is WZ or ZB. Therefore, I believed that it would be a reasonable approximation to apply the parameters for ZB to WZ.

Generating Surface States

A source of surface states in semiconductor QDs is the dangling bonds on anions in the surface of the core, especially when those anions are not properly passivated by organic ligands or by layers of another semiconductor shells. QDs with core/shell structure have been introduced to reduce the strains, and so reduced a source of surface state. The core/shell QDs have attracted most of attention and have been widely studied. For them, traps due to the lattice mismatch occur at the core/shell interface.

Since a purpose of this dissertation is to obtain an understanding of the various electronic dynamics within QDs that lead to the Auger process, the balance between an accurate treatment of the experimental setting and computational feasibility played a role in choosing a computational procedure. To reproduce traps due to the lattice mismatch, no cation in the shell was removed and the geometry of the shell also remained unaffected. Instead, a single (or multiple) anion(s) at the core/shell interface was selected, and the atomic interactions with its NNs (cations in the shell) were set equal to zero to create a “dangling-like” atom. Moreover, its on-site TB parameters (namely the *E*'s in Table 2.1) were adjusted to generate surface states that were isolated from the band of bulk states.[24] The atomic TB parameters of the five *s*, *p* and *s** orbitals on the picked anion were all adjusted to generate five new bases that preserved the hybridization of sp^3 orbitals. The values of parameters in the adjustment needed to be such that the energy difference of the trap and the VB edge was equal to the energy difference between the $1S_e$ state and $1P_e$ state in the conduction band, thus satisfying a requirement that there has to be an energy resonance for the Auger transition to occur[25], and keeping consistent with experimental results of Guyot-Sionnest and co-workers[26,27] on this Auger based resonance charge transfer.

The result in Chapter 4 doesn't use the technique here to generate surface states, but it can be applied in future work when studying the Auger process involving a trapping process.

Removal of the band gap states

In principle, there may be dangling bonds at the surface of QDs. During the process of the fabrication of QDs, the process is used in solutions containing the necessary organometallic precursors[10, 28], for example, dimethylcadmium ($CdMe_2$), trioctylphosphine selenide ((TOP)Se), and in a solvent, trioctylphosphine oxide (TOPO). The surface of the colloidal QDs fabricated by this process is capped by the TOPO in the solution even though the surface cannot be fully passivated by it, especially for large QDs[29]. In theoretical calculations, the unsaturated dangling bonds at a surface are usually undesired, in part because the energetic position of the dangling surface states (within the band gap) makes it difficult to identify the edge of VB.

Accordingly it was decided to remove the dangling surface states in the theoretical calculations. To do so, a layer of atoms, used to mimic the effect of organic ligands, like TOPO, was added onto the outermost surface of QDs. In this dissertation, instead of the commonly-used hydrogen[21] or oxygen[30], a layer of artificial atoms, whose TB parameters (as shown in Table 2.1) are defined by the author, is used to facilitate the calculation and analysis. The advantage of using self-defined artificial atoms is that one can easily obtain a complete set of interactions between the artificial atoms and the anion/cation in the QD, preventing from suffering of lacking parameters in the literature. The off-diagonal terms (namely the V's) in Table 2.1 have been optimized by scanning around their respective neighboring values to ensure that the band gap states are removed. The value of V_{ss}, V_{sapc} and V_{pasc} for the artificial atoms (AA or AC) in Table 2.1 are size-dependent: the larger the size of QD, the smaller those values.

Using the SALC method, however, adds a subtlety to the full passivation of QDs:

for the artificial atoms on the $\sigma_{v''}$ plane in Fig. 1, which have two nearest neighbors on either side of the $\sigma_{v''}$ in a complete QD, it needs to be ensured that the AOs on the artificial atom can generate bases with all kinds of symmetry (namely A_1, A_2, or E). In the dissertation, for all the artificial atoms, five AOs (namely *s*, *p*, and *s**) are included on the artificial atoms on the $\sigma_{v''}$.

Robustness Test of the SALC Method

The SALC methodology mentioned in the previous section reduces the computational effort and time as well. To test the robustness of the method and the accuracy of the results generated by the author's code and compiled programs, the comparison between the calculated results using the Hamiltonian of SALC method and using the Hamiltonian of a control group, including the eigenvalues (E) and eigenfunctions, is required. The control group is for a complete QD whose geometry is identical to that of the reconstruction of a 1/6 QD and is obtained from the latter using the symmetry operators in the C_{3V} group. The same set of TB parameters is applied to the control group. The diagonal terms in the Hamiltonian of the control group are the site energy of each atom and off-diagonal terms. They are non-zero only between an atom and its nearest-neighbors. The diagonalization of the Hamiltonian generated the eigenvalues and eigenstates for comparison of the complete QD and the calculation based on 1/6 segment of the QD, using symmetry argument in the latter case to construct the entire QD.

Instead of comparing all of the states of the complete QD method obtained from a

1/6 portion of it, the neighboring states in the following three categories were chosen for comparison: (1) the states at the CB edge and VB edge, (2) the states in the CB whose energies are about one-band-gap above the CB edge, and (3) the states in VB whose energy are one-band-gap below the VB edge, as shown in Table 2.5. The comparison is shown in Table 2.5: the relative deviation of eigenvalues, ΔE/E, of the chosen states between the two methods is around the order of ±0.01 % or even less, which is negligible. Moreover, when one compares the coefficients of each AO for states of interest, the relative deviation, ΔC/C, of coefficients C (for $|C|\geq 0.01$) for those states is no larger than 1.82%. Accordingly, the program and the calculated eigenstates and eigenvalues used through the thesis, based on using 1/6 of the QD plus symmetry, are regarded as reliable.

Summary

The integration of SALC method and TB method has shown reliability and accuracy for the computational purpose of obtaining eigenvalues and eigenvectors of semiconductor QDs. The eigenvectors are used further in the following chapters for the calculations, such as those for band gap, absorption spectrum, and the matrix elements of Auger processes.

Reference

1. Efros, A. L.; Rosen, M., The electronic structure of semiconductor nanocrystals. *Annu Rev Mater Sci* **2000,** *30*, 475-521.

2. Muto, T., Effective mass approximation in the band theory. *Proceedings of the Institute of Natural Sciences, Nihon University* **1968,** (4), 1-46.

3. Marcus, R. A., Interaction of theory and experiment: examples from single molecule studies of nanoparticles. *Philos T R Soc A* **2010,** *368* (1914), 1109-1124.

4. Kobayashi, A.; Sankey, O. F.; Volz, S. M.; Dow, J. D., Semiempirical Tight-Binding Band Structures of Wurtzite Semiconductors - AlN, CdS, CdSe, ZnS, and ZnO. *Phys Rev B* **1983,** *28* (2), 935-945.

5. Vogl, P.; Hjalmarson, H. P.; Dow, J. D., A Semi-Empirical Tight-Binding Theory of the Electronic-Structure of Semiconductors. *J Phys Chem Solids* **1983,** *44* (5), 365-378.

6. Ashcroft, N. W.; Mermin, N. D., Solid state phys. *Saunders, Philadelphia* **1976,** *293*.

7. Lippens, P. E.; Lannoo, M., Calculation of the band gap for small CdS and ZnS crystallites. *Phys Rev B* **1989,** *39* (15), 10935.

8. Shim, M.; Guyot-Sionnest, P., Permanent dipole moment and charges in colloidal semiconductor quantum dots. *J Chem Phys* **1999,** *111* (15), 6955-6964.

9. Mohamed, M. B.; Tonti, D.; Al-Salman, A.; Chemseddine, A.; Chergui, M., Synthesis of High Quality Zinc Blende CdSe Nanocrystals. *J Phys Chem B* **2005,** *109* (21), 10533-10537.

10. Dabbousi, B. O.; Rodriguez-Viejo, J.; Mikulec, F. V.; Heine, J. R.; Mattoussi, H.; Ober, R.; Jensen, K. F.; Bawendi, M. G., (CdSe)ZnS Core−Shell Quantum Dots: Synthesis and Characterization of a Size Series of Highly Luminescent Nanocrystallites. *J Phys Chem B* **1997,** *101* (46), 9463-9475.

11. Qin, W.; Shah, R. A.; Guyot-Sionnest, P., CdSeS/ZnS Alloyed Nanocrystal Lifetime and Blinking Studies under Electrochemical Control. *Acs Nano* **2011,** *6* (1), 912-918.

12. Hines, M. A.; Guyot-Sionnest, P., Synthesis and Characterization of Strongly Luminescing ZnS-Capped CdSe Nanocrystals. *J Phys Chem* **1996,** *100* (2), 468-471.

13. Qin, W.; Guyot-Sionnest, P., Evidence for the Role of Holes in Blinking: Negative and Oxidized CdSe/CdS Dots. *Acs Nano* **2012,** *6* (10), 9125-9132.

14. Murray, C. B. Synthesis and characterization of II-IV quantum dots and their

assembly into 3D quantum dot superlattices. Massachusetts Institute of Technology, 1995.

15. Cotton, F. A., *Chemical applications of group theory.* 3rd ed.; Wiley: New York, 1990; p xiv, 461 p.

16. Anderson, E.; Bai, Z.; Bischof, C.; Blackford, S.; Demmel, J.; Dongarra, J.; Du Croz, J.; Greenbaum, A.; Hammarling, S.; McKenney, A., *LAPACK Users' Guide Third Edition. Society for Industrial and Applied Mathematics, 1999.* 1999; Vol. 41.

17. Harrison, W. A., Bond-orbital model and the properties of tetrahedrally coordinated solids. *Phys Rev B* **1973,** *8* (10), 4487.

18. Harrison, W. A.; Ciraci, S., Bond-orbital model. II. *Phys Rev B* **1974,** *10* (4), 1516.

19. Pantelides, S. T.; Harrison, W. A., Structure of the valence bands of zinc-blende-type semiconductors. *Phys Rev B* **1975,** *11* (8), 3006.

20. Lippens, P. E.; Lannoo, M., Comparison between Calculated and Experimental Values of the Lowest Excited Electronic State of Small Cdse Crystallites. *Phys Rev B* **1990,** *41* (9), 6079-6081.

21. Albe, V.; Jouanin, C.; Bertho, D., Confinement and shape effects on the optical spectra of small CdSe nanocrystals. *Phys Rev B* **1998,** *58* (8), 4713-4720.

22. Pokrant, S.; Whaley, K., Tight-binding studies of surface effects on electronic structure of CdSe nanocrystals: the role of organic ligands, surface reconstruction, and inorganic capping shells. *Eur Phys J D -Atomic, Molecular, Optical and Plasma Physics* **1999,** *6* (2), 255-267.

23. von Grünberg, H. H., Energy levels of CdSe quantum dots: Wurtzite versus zinc-blende structure. *Phys Rev B* **1997,** *55* (4), 2293.

24. Davison, S. G.; Levine, J. D., Surface States. In *Solid State Physics*, Henry Ehrenreich, F. S.; David, T., Eds. Academic Press: 1970; Vol. Volume 25, pp 1-149.

25. Frantsuzov, P. A.; Marcus, R. A., Explanation of quantum dot blinking without the long-lived trap hypothesis. *Phys Rev B* **2005,** *72* (15).

26. Shim, M.; Guyot-Sionnest, P., n-type colloidal semiconductor nanocrystals. *Nature* **2000,** *407* (6807), 981.

27. Guyot-Sionnest, P.; Shim, M.; Matranga, C.; Hines, M., Intraband relaxation in CdSe quantum dots. *Phys Rev B* **1999,** *60* (4), R2181-R2184.

28. Murray, C. B.; Norris, D. J.; Bawendi, M. G., Synthesis and characterization of nearly monodisperse CdE (E = sulfur, selenium, tellurium) semiconductor nanocrystallites. *J Am Chem Soc* **1993,** *115* (19), 8706-8715.

29. Katari, J. E. B.; Colvin, V. L.; Alivisatos, A. P., X-ray Photoelectron Spectroscopy of CdSe Nanocrystals with Applications to Studies of the Nanocrystal Surface. *J Phys*

Chem **1994,** *98* (15), 4109-4117.

30. Hill, N. A.; Whaley, K. B., A theoretical study of the influence of the surface on the electronic structure of CdSe nanoclusters. *J Chem Phys* **1994,** *100* (4), 2831-2837.

31. Hanwell, M. D.; Curtis, D. E.; Lonie, D. C.; Vandermeersch, T.; Zurek, E.; Hutchison, G. R., Avogadro: An advanced semantic chemical editor, visualization, and analysis platform. *J. Cheminformatics* **2012,** *4* (1), 17.

32. Leung, K.; Pokrant, S.; Whaley, K. B., Exciton fine structure in CdSe nanoclusters. *Phys Rev B* **1998,** *57* (19), 12291.

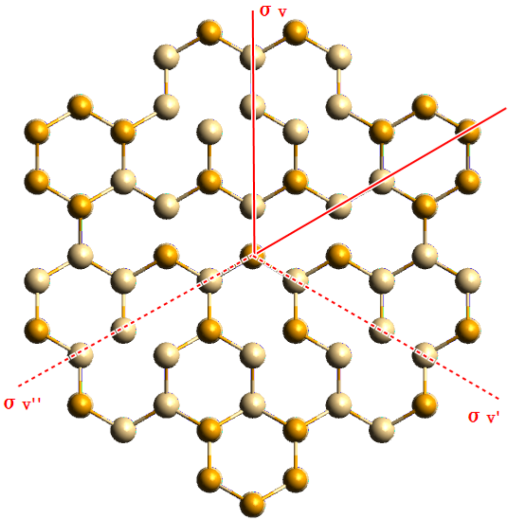

Fig. 2.1 The Top view (looking down from the symmetry axis, or *c* axis) of a CdSe QD with its radius about 1.17 nm (aspect ratio ~1.1). The geometry of the QD is plotted by the molecular visualization software Avogadro.[31] Some bonds in the firgure are absent in the figure because they are not recognized by the graphic software, but in reality, those bonds actually exist.

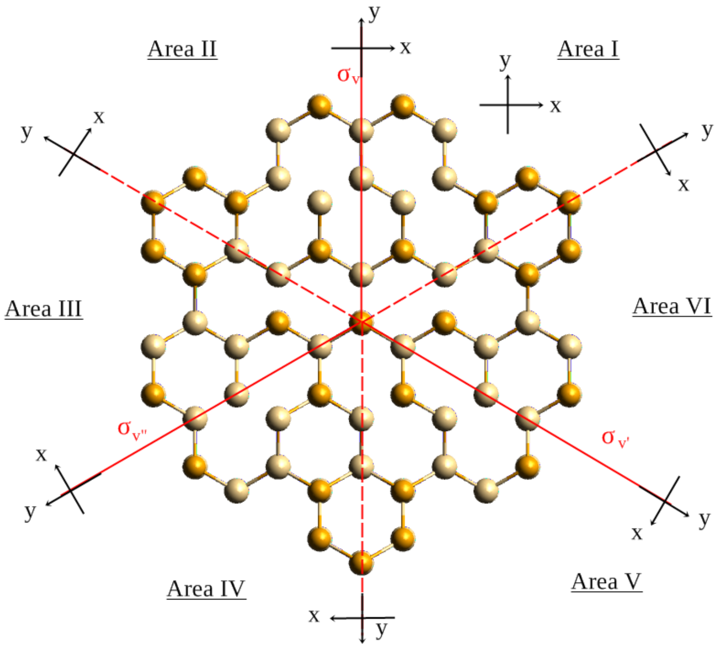

Fig. 2.2 The pre-defined Cartesian coordinates, which determined the sign of the *p* orbitals on each atom, on Areas I to VI and on the three reflective σ planes in the QD. These coordinates determine the sign and the value of the TB parameters between different region. The geometry of the QD is the same as the one in Fig. 2.1 and is plotted by the molecular visualization software Avogadro.[31] Some bonds in the firgure are absent in the figure because they are not recognized by the graphic software, but in reality, those bonds actually exist.

Table 2.1 The TB parameters for Cd, Se, and the artificial atoms

Diagonal Terms (eV)

Compound	E_s	E_p	E_{s*}
Cd	0.030	4.730[3]	5.720
Se	-9.630	1.326[3]	7.530
AA	-20.0	-40.0[3]	-40.0
AC	20.0	40.0[3]	40.0

Off-diagonal Terms (eV)

Compound	V_{ss}	V_{xx}	V_{xy}	V_{sapc}	V_{pasc}	V_{s*apc}	V_{pas*c}
CdSe	-1.160	0.660	1.340	1.143	-1.385	0.623	-0.763
Cd(AA)	-5.5 – -6.0	0.0	0.0	5.5 – 6.0	-5.5 – -6.0	0.0	0.0
(AC)Se	-5.5 – -6.0	0.0	0.0	5.5 – 6.0	-5.5 – -6.0	0.0	0.0

1. The unit of the values in this table is eV.
2. AA and AC are defined by the author. AA represents the artificial atom of anion, and AC represents the artificial atom of cation.
3. An additional -40 meV[32] were added the diagonal terms for P_z orbitals of all Cd, Se, AA, and AC atoms to reproduce the A-B splitting in a hexagonal lattice structure.

(a) Orientation 1 (b) Orientation 2

(c) Orientation 3 (d) Orientation 4

Fig. 2.3 The definition of the four orientations used in the thesis. The z axis of the defined coordinate system is pointing outward from the paper, and the x axis is pointing toward the top of the page.

Table 2.2 The matrix of off-diagonal coupling terms for the atoms in Area I, on σ_V and the rotational axis in Fig. 2.2

Orientation 1 (anion centered)

	s_c^{WZ}	$p_{x,c}^{WZ}$	$p_{y,c}^{WZ}$	$p_{z,c}^{WZ}$	s_c^{*WZ}
s_a^{WZ}	V_{ss}	$\sqrt{2}V_{s_a p_c}$	$\frac{-2}{\sqrt{6}}V_{s_a p_c}$	$\frac{-1}{\sqrt{3}}V_{s_a p_c}$	0.0
$p_{x,a}^{WZ}$	$\sqrt{2}V_{p_a s_c}$	$V_{xx}+V_{xy}$	$\frac{-4}{\sqrt{12}}V_{xy}$	$\frac{-2}{\sqrt{6}}V_{xy}$	$\sqrt{2}V_{s_c^* p_a}$
$p_{y,a}^{WZ}$	$\frac{-2}{\sqrt{6}}V_{p_a s_c}$	$\frac{-4}{\sqrt{12}}V_{xx}$	$V_{xx}-\frac{1}{3}V_{xy}$	$\frac{2}{\sqrt{18}}V_{xy}$	$\frac{-2}{\sqrt{6}}V_{s_c^* p_a}$
$p_{z,a}^{WZ}$	$\frac{-1}{\sqrt{3}}V_{p_a s_c}$	$\frac{-2}{\sqrt{6}}V_{xy}$	$\frac{2}{\sqrt{18}}V_{xy}$	$V_{xx}-\frac{2}{3}V_{xy}$	$\frac{-1}{\sqrt{3}}V_{s_c^* p_a}$
s_a^{*WZ}	0.0	$\sqrt{2}V_{s_a p_c}$	$\frac{-2}{\sqrt{6}}V_{s_a^* p_c}$	$\frac{-1}{\sqrt{3}}V_{s_a^* p_c}$	$V_{s^* s^*}$

Orientation 2 (cation centered)

	s_c^{WZ}	$p_{x,c}^{WZ}$	$p_{y,c}^{WZ}$	$p_{z,c}^{WZ}$	s_c^{*WZ}
s_a^{WZ}	V_{ss}	$-\sqrt{2}V_{s_a p_c}$	$\frac{-2}{\sqrt{6}}V_{s_a p_c}$	$\frac{-1}{\sqrt{3}}V_{s_a p_c}$	0.0
$p_{x,a}^{WZ}$	$-\sqrt{2}V_{p_a s_c}$	$V_{xx}+V_{xy}$	$\frac{4}{\sqrt{12}}V_{xy}$	$\frac{2}{\sqrt{6}}V_{xy}$	$-\sqrt{2}V_{s_c^* p_a}$
$p_{y,a}^{WZ}$	$\frac{-2}{\sqrt{6}}V_{p_a s_c}$	$\frac{4}{\sqrt{12}}V_{xx}$	$V_{xx}-\frac{1}{3}V_{xy}$	$\frac{2}{\sqrt{18}}V_{xy}$	$\frac{-2}{\sqrt{6}}V_{s_c^* p_a}$
$p_{z,a}^{WZ}$	$\frac{-1}{\sqrt{3}}V_{p_a s_c}$	$\frac{2}{\sqrt{6}}V_{xy}$	$\frac{2}{\sqrt{18}}V_{xy}$	$V_{xx}-\frac{2}{3}V_{xy}$	$\frac{-1}{\sqrt{3}}V_{s_c^* p_a}$
s_a^{*WZ}	0.0	$-\sqrt{2}V_{s_a p_c}$	$\frac{-2}{\sqrt{6}}V_{s_a^* p_c}$	$\frac{-1}{\sqrt{3}}V_{s_a^* p_c}$	$V_{s^* s^*}$

1. The definitions of the *V*'s are defined in Table 2.1
2. The definition of the orientation is described in Fig. 2.3. The *a* and *c* in the subscript represent anion and cation, respectively.

(*contd.*)

Table 2.2 (*contd.*)The matrix of off-diagonal coupling terms for the atoms in Area I, on σ_V and the rotational axis in Fig. 2.2

Orientation 3 (anion centered)					
	s_c^{WZ}	$p_{x,c}^{WZ}$	$p_{y,c}^{WZ}$	$p_{z,c}^{WZ}$	s_c^{*WZ}
s_a^{WZ}	V_{ss}	0.0	$\frac{4}{\sqrt{6}}V_{s_a p_c}$	$\frac{-1}{\sqrt{3}}V_{s_a p_c}$	0.0
$p_{x,a}^{WZ}$	0.0	$V_{xx}-V_{xy}$	0.0	0.0	0.0
$p_{y,a}^{WZ}$	$\frac{4}{\sqrt{6}}V_{p_a s_c}$	0.0	$V_{xx}+\frac{5}{3}V_{xy}$	$\frac{-4}{\sqrt{18}}V_{xy}$	$\frac{4}{\sqrt{6}}V_{s_c^* p_a}$
$p_{z,a}^{WZ}$	$\frac{-1}{\sqrt{3}}V_{p_a s_c}$	0.0	$\frac{-4}{\sqrt{18}}V_{xy}$	$V_{xx}-\frac{2}{3}V_{xy}$	$\frac{-1}{\sqrt{3}}V_{s_c^* p_a}$
s_a^{*WZ}	0.0	0.0	$\frac{4}{\sqrt{6}}V_{s_a^* p_c}$	$\frac{-1}{\sqrt{3}}V_{s_a^* p_c}$	$V_{s^* s^*}$
Orientation 4 (cation centered)					
	s_c^{WZ}	$p_{x,c}^{WZ}$	$p_{y,c}^{WZ}$	$p_{z,c}^{WZ}$	s_c^{*WZ}
s_a^{WZ}	V_{ss}	0.0	0.0	$\sqrt{3}V_{s_a p_c}$	0.0
$p_{x,a}^{WZ}$	0.0	$V_{xx}-V_{xy}$	0.0	0.0	0.0
$p_{y,a}^{WZ}$	0.0	0.0	$V_{xx}-V_{xy}$	0.0	0.0
$p_{z,a}^{WZ}$	$\sqrt{3}V_{p_a s_c}$	0.0	0.0	$V_{xx}+2V_{xy}$	$\sqrt{3}V_{s_c^* p_a}$
s_a^{*WZ}	0.0	0.0	0.0	$\sqrt{3}V_{s_a^* p_c}$	$V_{s^* s^*}$

1. The definitions of the *V*'s are defined in Table 2.1
2. The definition of the orientation is described in Fig. 2.3. The *a* and *c* in the subscript represent anion and cation, respectively.

Table 2.3 The matrix of off-diagonal coupling terms between the anions on $\sigma_{V''}$ and their neighbors in Area I in Fig. 2.2.

Orientation 1 (anion centered)					
	s_c^{WZ}	$p_{x,c}^{WZ}$	$p_{y,c}^{WZ}$	$p_{z,c}^{WZ}$	s_c^{*WZ}
s_a^{WZ}	V_{ss}	$\sqrt{2}V_{s_a p_c}$	$\frac{-2}{\sqrt{6}}V_{s_a p_c}$	$\frac{-1}{\sqrt{3}}V_{s_a p_c}$	0.0
$p_{x,a}^{WZ}$	$\sqrt{2}V_{p_a s_c}$	$\frac{1}{2}V_{xx}+\frac{3}{2}V_{xy}$	$\frac{-3}{\sqrt{12}}V_{xx}-\frac{1}{\sqrt{12}}V_{xy}$	$\frac{-2}{\sqrt{6}}V_{xy}$	$\sqrt{2}V_{s_c^* p_a}$
$p_{y,a}^{WZ}$	$\frac{2}{\sqrt{6}}V_{p_a s_c}$	$\frac{3}{\sqrt{12}}V_{xx}+\frac{1}{\sqrt{12}}V_{xy}$	$\frac{1}{2}V_{xx}-\frac{7}{6}V_{xy}$	$\frac{-2}{\sqrt{18}}V_{xy}$	$\frac{2}{\sqrt{6}}V_{s_c^* p_a}$
$p_{z,a}^{WZ}$	$\frac{-1}{\sqrt{3}}V_{p_a s_c}$	$\frac{-2}{\sqrt{6}}V_{xy}$	$\frac{2}{\sqrt{18}}V_{xy}$	$V_{xx}-\frac{2}{3}V_{xy}$	$\frac{-1}{\sqrt{3}}V_{s_c^* p_a}$
s_a^{*WZ}	0.0	$\sqrt{2}V_{s_a p_c}$	$\frac{-2}{\sqrt{6}}V_{s_a^* p_c}$	$\frac{-1}{\sqrt{3}}V_{s_a^* p_c}$	$V_{s^* s^*}$
Orientation 2 (anion centered)					
	s_c^{WZ}	$p_{x,c}^{WZ}$	$p_{y,c}^{WZ}$	$p_{z,c}^{WZ}$	s_c^{*WZ}
s_a^{WZ}	V_{ss}	$-\sqrt{2}V_{s_a p_c}$	$\frac{-2}{\sqrt{6}}V_{s_a p_c}$	$\frac{-1}{\sqrt{3}}V_{s_a p_c}$	0.0
$p_{x,a}^{WZ}$	0.0	$\frac{1}{2}V_{xx}-\frac{1}{2}V_{xy}$		0.0	0.0
$p_{y,a}^{WZ}$	$\frac{-4}{\sqrt{6}}V_{p_a s_c}$	$\frac{3}{\sqrt{12}}V_{xx}+\frac{5}{\sqrt{12}}V_{xy}$	$\frac{1}{2}V_{xx}+\frac{5}{6}V_{xy}$	$\frac{4}{\sqrt{18}}V_{xy}$	$\frac{-4}{\sqrt{6}}V_{s_c^* p_a}$
$p_{z,a}^{WZ}$	$\frac{-1}{\sqrt{3}}V_{p_a s_c}$	$\frac{2}{\sqrt{6}}V_{xy}$	$\frac{2}{\sqrt{18}}V_{xy}$	$V_{xx}-\frac{2}{3}V_{xy}$	$\frac{-1}{\sqrt{3}}V_{s_c^* p_a}$
s_a^{*WZ}	0.0	$-\sqrt{2}V_{s_a p_c}$	$\frac{-2}{\sqrt{6}}V_{s_a^* p_c}$	$\frac{-1}{\sqrt{3}}V_{s_a^* p_c}$	$V_{s^* s^*}$

1. The definitions of the *V*'s are defined in Table 2.1
2. The Cartesian coordinates are defined in Fig. 2.2
3. The definition of the orientation is described in Fig. 2.3. The *a* and *c* in the subscript represent anion and cation, respectively.

(*contd.*)

Table 2.3 (*contd.*)The matrix of off-diagonal coupling terms between the anions on $\sigma_{V''}$ and their neighbors in Area I in Fig. 2.2.

Orientation 3 (anion centered)					
	s_c^{WZ}	$p_{x,c}^{WZ}$	$p_{y,c}^{WZ}$	$p_{z,c}^{WZ}$	s_c^{*WZ}
s_a^{WZ}	V_{ss}	0.0	$\frac{4}{\sqrt{6}}V_{s_a p_c}$	$\frac{-1}{\sqrt{3}}V_{s_a p_c}$	0.0
$p_{x,a}^{WZ}$	$-\sqrt{2}V_{p_a s_c}$	$\frac{1}{2}V_{xx}-\frac{1}{2}V_{xy}$	$\frac{-3}{\sqrt{12}}V_{xx}-\frac{5}{\sqrt{12}}V_{xy}$	$\frac{2}{\sqrt{6}}V_{xy}$	$-\sqrt{2}V_{s_c^* p_a}$
$p_{y,a}^{WZ}$	$\frac{2}{\sqrt{6}}V_{p_a s_c}$	$\frac{3}{\sqrt{12}}V_{xx}-\frac{3}{\sqrt{12}}V_{xy}$	$\frac{1}{2}V_{xx}+\frac{5}{6}V_{xy}$	$\frac{-4}{\sqrt{18}}V_{xy}$	$\frac{2}{\sqrt{6}}V_{s_c^* p_a}$
$p_{z,a}^{WZ}$	$\frac{-1}{\sqrt{3}}V_{p_a s_c}$	0.0	$\frac{-4}{\sqrt{18}}V_{xy}$	$V_{xx}-\frac{2}{3}V_{xy}$	
s_a^{*WZ}	0.0	0.0	$\frac{4}{\sqrt{6}}V_{s_a^* p_c}$	$\frac{-1}{\sqrt{3}}V_{s_a^* p_c}$	$V_{s^* s^*}$
Orientation 4 (anion centered)					
	s_c^{WZ}	$p_{x,c}^{WZ}$	$p_{y,c}^{WZ}$	$p_{z,c}^{WZ}$	s_c^{*WZ}
s_a^{WZ}	V_{ss}	0.0	0.0	$\sqrt{3}V_{s_a p_c}$	0.0
$p_{x,a}^{WZ}$	0.0	$\frac{1}{2}V_{xx}-\frac{1}{2}V_{xy}$	$\frac{-3}{\sqrt{12}}V_{xx}+\frac{3}{\sqrt{12}}V_{xy}$	0.0	0.0
$p_{y,a}^{WZ}$	0.0		$\frac{1}{2}V_{xx}-\frac{1}{2}V_{xy}$	0.0	0.0
$p_{z,a}^{WZ}$	$\sqrt{3}V_{p_a s_c}$	0.0	0.0	$V_{xx}+2V_{xy}$	$\sqrt{3}V_{s_c^* p_a}$
s_a^{*WZ}	0.0	0.0	0.0	$\sqrt{3}V_{s_a^* p_c}$	$V_{s^* s^*}$

1. The definitions of the *V*'s are defined in Table 2.1
2. The Cartesian coordinates are defined in Fig. 2.2
3. The definition of the orientation is described in Fig. 2.3. The *a* and *c* in the subscript represent anion and cation, respectively.

(*contd.*)

Table 2.3 (*contd.*)The matrix of off-diagonal coupling terms between the anions on $\sigma_{V''}$ and their neighbors in Area I in Fig. 2.2.

<table>
<tr><td colspan="6">Orientation 1 (cation centered)</td></tr>
<tr><td></td><td>s_c^{WZ}</td><td>$p_{x,c}^{WZ}$</td><td>$p_{y,c}^{WZ}$</td><td>$p_{z,c}^{WZ}$</td><td>s_c^{*WZ}</td></tr>
<tr><td>s_a^{WZ}</td><td>V_{ss}</td><td>$\sqrt{2}V_{s_a p_c}$</td><td>$\frac{2}{\sqrt{6}}V_{s_a p_c}$</td><td>$\frac{-1}{\sqrt{3}}V_{s_a p_c}$</td><td>0.0</td></tr>
<tr><td>$p_{x,a}^{WZ}$</td><td>$\sqrt{2}V_{p_a s_c}$</td><td>$\frac{1}{2}V_{xx}+\frac{3}{2}V_{xy}$</td><td>$\frac{3}{\sqrt{12}}V_{xx}+\frac{1}{\sqrt{12}}V_{xy}$</td><td>$\frac{-2}{\sqrt{6}}V_{xy}$</td><td>$\sqrt{2}V_{s_c^* p_a}$</td></tr>
<tr><td>$p_{y,a}^{WZ}$</td><td>$\frac{-2}{\sqrt{6}}V_{p_a s_c}$</td><td>$\frac{-3}{\sqrt{12}}V_{xx}-\frac{1}{\sqrt{12}}V_{xy}$</td><td>$\frac{1}{2}V_{xx}-\frac{7}{6}V_{xy}$</td><td>$\frac{2}{\sqrt{18}}V_{xy}$</td><td>$\frac{-2}{\sqrt{6}}V_{s_c^* p_a}$</td></tr>
<tr><td>$p_{z,a}^{WZ}$</td><td>$\frac{-1}{\sqrt{3}}V_{p_a s_c}$</td><td>$\frac{-2}{\sqrt{6}}V_{xy}$</td><td>$\frac{-2}{\sqrt{18}}V_{xy}$</td><td>$V_{xx}-\frac{2}{3}V_{xy}$</td><td>$\frac{-1}{\sqrt{3}}V_{s_c^* p_a}$</td></tr>
<tr><td>s_a^{*WZ}</td><td>0.0</td><td>$\sqrt{2}V_{s_a p_c}$</td><td>$\frac{2}{\sqrt{6}}V_{s_a^* p_c}$</td><td>$\frac{-1}{\sqrt{3}}V_{s_a^* p_c}$</td><td>$V_{s^* s^*}$</td></tr>
<tr><td colspan="6">Orientation 2 (cation centered)</td></tr>
<tr><td></td><td>s_c^{WZ}</td><td>$p_{x,c}^{WZ}$</td><td>$p_{y,c}^{WZ}$</td><td>$p_{z,c}^{WZ}$</td><td>s_c^{*WZ}</td></tr>
<tr><td>s_a^{WZ}</td><td>V_{ss}</td><td>0.0</td><td>$\frac{-4}{\sqrt{6}}V_{s_a p_c}$</td><td>$\frac{-1}{\sqrt{3}}V_{s_a p_c}$</td><td>0.0</td></tr>
<tr><td>$p_{x,a}^{WZ}$</td><td>$-\sqrt{2}V_{p_a s_c}$</td><td>$\frac{1}{2}V_{xx}-\frac{1}{2}V_{xy}$</td><td>$\frac{3}{\sqrt{12}}V_{xx}+\frac{5}{\sqrt{12}}V_{xy}$</td><td>$\frac{2}{\sqrt{6}}V_{xy}$</td><td>$-\sqrt{2}V_{s_c^* p_a}$</td></tr>
<tr><td>$p_{y,a}^{WZ}$</td><td>$\frac{-2}{\sqrt{6}}V_{p_a s_c}$</td><td>$\frac{-3}{\sqrt{12}}V_{xx}+\frac{3}{\sqrt{12}}V_{xy}$</td><td>$\frac{1}{2}V_{xx}+\frac{5}{6}V_{xy}$</td><td>$\frac{2}{\sqrt{18}}V_{xy}$</td><td>$\frac{-2}{\sqrt{6}}V_{s_c^* p_a}$</td></tr>
<tr><td>$p_{z,a}^{WZ}$</td><td>$\frac{-1}{\sqrt{3}}V_{p_a s_c}$</td><td>0.0</td><td>$\frac{4}{\sqrt{18}}V_{xy}$</td><td>$V_{xx}-\frac{2}{3}V_{xy}$</td><td>$\frac{-1}{\sqrt{3}}V_{s_c^* p_a}$</td></tr>
<tr><td>s_a^{*WZ}</td><td>0.0</td><td>0.0</td><td>$\frac{-4}{\sqrt{6}}V_{s_a^* p_c}$</td><td>$\frac{-1}{\sqrt{3}}V_{s_a^* p_c}$</td><td>$V_{s^* s^*}$</td></tr>
</table>

1. The definitions of the *V*'s are defined in Table 2.1
2. The Cartesian coordinates are defined in Fig. 2.2
3. The definition of the orientation is described in Fig. 2.3. The *a* and *c* in the subscript represent anion and cation, respectively.

(contd.)

Table 2.3 (*contd.*)The matrix of off-diagonal coupling terms between the anions on $\sigma_{V''}$ and their neighbors in Area I in Fig. 2.2.

Orientation 3 (cation centered)

	s_c^{WZ}	$p_{x,c}^{WZ}$	$p_{y,c}^{WZ}$	$p_{z,c}^{WZ}$	s_c^{*WZ}
s_a^{WZ}	V_{ss}	$-\sqrt{2}V_{s_a p_c}$	$\frac{2}{\sqrt{6}}V_{s_a p_c}$	$\frac{-1}{\sqrt{3}}V_{s_a p_c}$	0.0
$p_{x,a}^{WZ}$	0.0	$\frac{1}{2}V_{xx}-\frac{1}{2}V_{xy}$	$\frac{3}{\sqrt{12}}V_{xx}-\frac{3}{\sqrt{12}}V_{xy}$	0.0	0.0
$p_{y,a}^{WZ}$	$\frac{4}{\sqrt{6}}V_{p_a s_c}$	$\frac{-3}{\sqrt{12}}V_{xx}-\frac{5}{\sqrt{12}}V_{xy}$	$\frac{1}{2}V_{xx}+\frac{5}{6}V_{xy}$	$\frac{-4}{\sqrt{18}}V_{xy}$	$\frac{4}{\sqrt{6}}V_{s_c^* p_a}$
$p_{z,a}^{WZ}$	$\frac{-1}{\sqrt{3}}V_{p_a s_c}$	$\frac{2}{\sqrt{6}}V_{xy}$	$\frac{-2}{\sqrt{18}}V_{xy}$	$V_{xx}-\frac{2}{3}V_{xy}$	$\frac{-1}{\sqrt{3}}V_{s_c^* p_a}$
s_a^{*WZ}	0.0	$-\sqrt{2}V_{s_a^* p_c}$	$\frac{2}{\sqrt{6}}V_{s_a^* p_c}$	$\frac{-1}{\sqrt{3}}V_{s_a^* p_c}$	$V_{s^* s^*}$

Orientation 4 (cation centered)

	s_c^{WZ}	$p_{x,c}^{WZ}$	$p_{y,c}^{WZ}$	$p_{z,c}^{WZ}$	s_c^{*WZ}
s_a^{WZ}	V_{ss}	0.0	0.0	$\sqrt{3}V_{s_a p_c}$	0.0
$p_{x,a}^{WZ}$	0.0	$\frac{1}{2}V_{xx}-\frac{1}{2}V_{xy}$	$\frac{3}{\sqrt{12}}V_{xx}-\frac{3}{\sqrt{12}}V_{xy}$	0.0	0.0
$p_{y,a}^{WZ}$	0.0	$\frac{-3}{\sqrt{12}}V_{xx}+\frac{3}{\sqrt{12}}V_{xy}$	$\frac{1}{2}V_{xx}-\frac{1}{2}V_{xy}$	0.0	0.0
$p_{z,a}^{WZ}$	$\sqrt{3}V_{p_a s_c}$	0.0	0.0	$V_{xx}+2V_{xy}$	$\sqrt{3}V_{s_c^* p_a}$
s_a^{*WZ}	0.0	0.0	0.0	$\sqrt{3}V_{s_a^* p_c}$	$V_{s^* s^*}$

1. The definitions of the *V*'s are defined in Table 2.1
2. The Cartesian coordinates are defined in Fig. 2.2
3. The definition of the orientation is described in Fig. 2.3. The *a* and *c* in the subscript represent anion and cation, respectively.

Table 2.4 The matrix of off-diagonal coupling terms between the anions on the rotation axis and their neighbors, the atoms on $\sigma_{V''}$ and on $\sigma_{V'}$, in Fig. 2.2

Orientation 1 (anion centered)					
	s_c^{WZ}	$p_{x,c}^{WZ}$	$p_{y,c}^{WZ}$	$p_{z,c}^{WZ}$	s_c^{*WZ}
s_a^{WZ}	V_{ss}	0.0	$\frac{4}{\sqrt{6}}V_{s_a p_c}$	$\frac{-1}{\sqrt{3}}V_{s_a p_c}$	0.0
$p_{x,a}^{WZ}$	$\sqrt{2}V_{p_a s_c}$	$\frac{-1}{2}V_{xx}+\frac{1}{2}V_{xy}$	$\frac{3}{\sqrt{12}}V_{xx}+\frac{5}{\sqrt{12}}V_{xy}$	$\frac{-2}{\sqrt{6}}V_{xy}$	$\sqrt{2}V_{s_c^* p_a}$
$p_{y,a}^{WZ}$	$\frac{-2}{\sqrt{6}}V_{p_a s_c}$	$\frac{-3}{\sqrt{12}}V_{xx}+\frac{3}{\sqrt{12}}V_{xy}$	$\frac{-1}{2}V_{xx}-\frac{5}{6}V_{xy}$	$\frac{2}{\sqrt{18}}V_{xy}$	$\frac{-2}{\sqrt{6}}V_{s_c^* p_a}$
$p_{z,a}^{WZ}$	$\frac{-1}{\sqrt{3}}V_{p_a s_c}$	0.0	$\frac{-4}{\sqrt{18}}V_{xy}$	$V_{xx}-\frac{2}{3}V_{xy}$	$\frac{-1}{\sqrt{3}}V_{s_c^* p_a}$
s_a^{*WZ}	0.0	0.0	$\frac{4}{\sqrt{6}}V_{s_a^* p_c}$	$\frac{-1}{\sqrt{3}}V_{s_a^* p_c}$	$V_{s^* s^*}$
Orientation 2 (anion centered)					
	s_c^{WZ}	$p_{x,c}^{WZ}$	$p_{y,c}^{WZ}$	$p_{z,c}^{WZ}$	s_c^{*WZ}
s_a^{WZ}	V_{ss}	0.0	$\frac{4}{\sqrt{6}}V_{s_a p_c}$	$\frac{-1}{\sqrt{3}}V_{s_a p_c}$	0.0
$p_{x,a}^{WZ}$	$-\sqrt{2}V_{p_a s_c}$	$\frac{-1}{2}V_{xx}+\frac{1}{2}V_{xy}$	$\frac{-3}{\sqrt{12}}V_{xx}-\frac{5}{\sqrt{12}}V_{xy}$	$\frac{2}{\sqrt{6}}V_{xy}$	$-\sqrt{2}V_{s_c^* p_a}$
$p_{y,a}^{WZ}$	$\frac{-2}{\sqrt{6}}V_{p_a s_c}$	$\frac{3}{\sqrt{12}}V_{xx}-\frac{3}{\sqrt{12}}V_{xy}$	$\frac{-1}{2}V_{xx}-\frac{5}{6}V_{xy}$	$\frac{2}{\sqrt{18}}V_{xy}$	$\frac{-2}{\sqrt{6}}V_{s_c^* p_a}$
$p_{z,a}^{WZ}$	$\frac{-1}{\sqrt{3}}V_{p_a s_c}$	0.0	$\frac{-4}{\sqrt{18}}V_{xy}$	$V_{xx}-\frac{2}{3}V_{xy}$	$\frac{-1}{\sqrt{3}}V_{s_c^* p_a}$
s_a^{*WZ}	0.0	0.0	$\frac{4}{\sqrt{6}}V_{s_a^* p_c}$	$\frac{-1}{\sqrt{3}}V_{s_a^* p_c}$	$V_{s^* s^*}$

1. The definitions of the *V*'s are defined in Table 2.1
2. The Cartesian coordinates are defined in Fig. 2.2
3. The definition of the orientation is described in Fig. 2.3. The *a* and *c* in the subscript represent anion and cation, respectively.

(*contd.*)

Table 2.4 (*contd.*)The matrix of off-diagonal coupling terms between the anions on the rotation axis and their neighbors, the atoms on $\sigma_{V''}$ and on $\sigma_{V'}$, in Fig. 2.2

Orientation 3 (cation centered)					
	s_c^{WZ}	$p_{x,c}^{WZ}$	$p_{y,c}^{WZ}$	$p_{z,c}^{WZ}$	s_c^{*WZ}
s_a^{WZ}	V_{ss}	$\sqrt{2}V_{s_a p_c}$	$\frac{-2}{\sqrt{6}}V_{s_a p_c}$	$\frac{-1}{\sqrt{3}}V_{s_a p_c}$	0.0
$p_{x,a}^{WZ}$	0.0	$\frac{-1}{2}V_{xx}+\frac{1}{2}V_{xy}$	$\frac{-3}{\sqrt{12}}V_{xx}+\frac{3}{\sqrt{12}}V_{xy}$	0.0	0.0
$p_{y,a}^{WZ}$	$\frac{4}{\sqrt{6}}V_{p_a s_c}$	$\frac{3}{\sqrt{12}}V_{xx}+\frac{5}{\sqrt{12}}V_{xy}$	$\frac{-1}{2}V_{xx}-\frac{5}{6}V_{xy}$	$\frac{-4}{\sqrt{18}}V_{xy}$	$\frac{4}{\sqrt{6}}V_{s_c^* p_a}$
$p_{z,a}^{WZ}$	$\frac{-1}{\sqrt{3}}V_{p_a s_c}$	$\frac{-2}{\sqrt{6}}V_{xy}$	$\frac{2}{\sqrt{18}}V_{xy}$	$V_{xx}-\frac{2}{3}V_{xy}$	$\frac{-1}{\sqrt{3}}V_{s_c^* p_a}$
s_a^{*WZ}	0.0	$\sqrt{2}V_{s_a^* p_c}$	$\frac{-2}{\sqrt{6}}V_{s_a^* p_c}$	$\frac{-1}{\sqrt{3}}V_{s_a^* p_c}$	$V_{s^* s^*}$
Orientation 4 (cation centered)					
	s_c^{WZ}	$p_{x,c}^{WZ}$	$p_{y,c}^{WZ}$	$p_{z,c}^{WZ}$	s_c^{*WZ}
s_a^{WZ}	V_{ss}	$-\sqrt{2}V_{s_a p_c}$	$\frac{-2}{\sqrt{6}}V_{s_a p_c}$	$\frac{-1}{\sqrt{3}}V_{s_a p_c}$	0.0
$p_{x,a}^{WZ}$	0.0	$\frac{-1}{2}V_{xx}+\frac{1}{2}V_{xy}$	$\frac{3}{\sqrt{12}}V_{xx}-\frac{3}{\sqrt{12}}V_{xy}$	0.0	0.0
$p_{y,a}^{WZ}$	$\frac{4}{\sqrt{6}}V_{p_a s_c}$	$\frac{-3}{\sqrt{12}}V_{xx}-\frac{5}{\sqrt{12}}V_{xy}$	$\frac{-1}{2}V_{xx}-\frac{5}{6}V_{xy}$	$\frac{-4}{\sqrt{18}}V_{xy}$	$\frac{4}{\sqrt{6}}V_{s_c^* p_a}$
$p_{z,a}^{WZ}$	$\frac{-1}{\sqrt{3}}V_{p_a s_c}$	$\frac{2}{\sqrt{6}}V_{xy}$	$\frac{2}{\sqrt{18}}V_{xy}$	$V_{xx}-\frac{2}{3}V_{xy}$	$\frac{-1}{\sqrt{3}}V_{s_c^* p_a}$
s_a^{*WZ}	0.0	$-\sqrt{2}V_{s_a^* p_c}$	$\frac{-2}{\sqrt{6}}V_{s_a^* p_c}$	$\frac{-1}{\sqrt{3}}V_{s_a^* p_c}$	$V_{s^* s^*}$

1. The definitions of the *V*'s are defined in Table 2.1
2. The Cartesian coordinates are defined in Fig. 2.2
3. The definition of the orientation is described in Fig. 2.3. The *a* and *c* in the subscript represent anion and cation, respectively.

Table 2.5 The comparison between the calculated result between the SALC method and the direct diagonalization of a complete QD.

	State # in mixture of symmetries	State # in symmetry group	Symmetry group	|ΔE/E| (in %) between two methods	Relative coefficient diff. between (ΔC/C, in %) for |coefficient| ≥ 0.01	
States in the band edge	1216	234	A1	2.7×10^{-3}	≤0.1/≤0.1	
	1215	805	E	3.9×10^{-3}	≤1/≤1	
	1214	806	E	3.9×10^{-3}	≤1/≤1	
	1213	233	A1	0	≤1/≤1	
	1212	176	A2	1.8×10^{-3}	≤1/≤1	
States in VB	866	571	E	0	≤1/≤1	
	867	572	E	5.5×10^{-4}	≤1.48/≤1.52	
	865	122	A2	8.2×10^{-4}	≤1.15/≤1.38	
	864	173	A1	8.2×10^{-4}	≤1.25/≤1.34	
States in CB	1550	311	A1	5.2×10^{-4}	≤1/≤1	
	1551	1025	E	5.2×10^{-4}	≤1/≤1	
	1552	1026	E	8.6×10^{-4}	≤1.55/≤1.82	
	1547	215	A2	3.5×10^{-4}	≤1/≤1	

The radius of the CdSe QD in this table is around 1.3 nm. The degenerate pair of E states of one method needs to rotate *w.r.t.* the rotation axis to compare with another method.

Chapter 3

The Calculated Properties of Semiconductor Quantum Dots

Background

The physical properties of QDs of different sizes using SALC method mentioned in Chapter 2 can be further compared with various calculated results in the literature. It has been reported that the aspect ratio of WZ CdSe QDs is between 1.1 to 1.3, depending on the size[1,2,3], and there are also certain significant facets[2] on the surface of the QDs. Therefore, to have a solid basis for the comparison that involves electron dynamics to compare with experimental measurements, the geometry of QDs should be as similar to the realistic QDs generally used in experiments. To meet the needs mentioned above, several calculated results, such as the structure of QDs used in this dissertation, band gap, density of states (DOS), and absorption spectrum, are discussed in this chapter and compared with experimental results.

Structure of Semiconductor Quantum Dots

The foundation of all the further calculations in this thesis is the structure of a WZ QD, in particular the connections between atoms and the facets of the crystal. Wide-angle X-ray scattering (WAXS) is a common X-ray diffraction (XRD) technique used to determine the crystal structure. The measured WAXS result of WZ CdSe QDs in C.B.

Murray's dissertation[1] has shown several significant features of having different facets, such as (100), (200), (110) (or $(11\bar{2}0)$), (103), (002) and (101) surface, and the relative intensities in the dissertation for those peaks are shown in Table 3.1. A curve of WAXS to an ellipsoidal geometry has shown in the same dissertation a better result than to a spherical geometry.[1] It would be challenging to programmatically generate a WZ QD fitting all the facets mentioned above because there would be many parameters for controlling the shape of a QD. Therefore, the aspect ratio ($\mu = 1.1 – 1.3$) and one of the significant facets observed in the WXAS, (002), were chosen as the criteria for building up the structure of a WZ QD. Among the significant peaks observed in the WXAS pattern[1,2, 4], the (002) plane is easier to characterize in the program. An example of the outcome of the author's program, a CdSe QD shown in Fig. 3.1 whose radius is around 3.73 nm and aspect ratio is around 1.3. In each figure in Fig. 3.1, the significant planes are labeled with colored solid lines, and their respective numbers in the whole QD are noted in the bottom right corner.

To examine if the structure is close to the experimental findings, the structure factor (F) is used as a measure to the WAXS data, since the diffracted amplitude is the proportional to $|F|^2$, which is the sum of all diffractions from each atom in the crystal. F is defined as[5],

$$F^{\text{crystal}}(\boldsymbol{Q}) = \sum_{j=1}^{N} f_j(\boldsymbol{Q}) e^{-2\pi i(\boldsymbol{Q}\cdot\boldsymbol{r}_j)} \sum_{n} e^{-2\pi i \boldsymbol{Q}\cdot\boldsymbol{R}_n} \quad , \tag{1}$$

where N denotes the number of atoms in a unit cell, $\mathbf{Q}$ is a scattering vector (the vector difference between the incident and diffracted rays[6]), $\boldsymbol{R}_n$ is a lattice vector in a crystal, $\boldsymbol{r}_j$ is the local position vector of an atom j in each unit cell, and f_j is the scattering factor[6] of the reflection from an atom *j*. As can be seen in Eq. (1), the structure factor is the product of two sums, the sum over the unit cell structure factor and the lattice sum[4]. One can achieve a non-zero $F^{crystal}$ if and only if the condition **Q** = **G** is fulfilled, where G is a lattice vector in the reciprocal lattice.[5] If **G** = **Q**, the product of $\boldsymbol{R}_n$ and **Q** in the lattice sum in Eq. (1) is an integer, and Eq. (1) becomes

$$F^{\text{crystal}}(\boldsymbol{G}) = M \sum_{j=1}^{N} f_j(\boldsymbol{G}) e^{-2\pi i(\boldsymbol{G}\cdot\boldsymbol{r}_j)} \quad , \tag{2}$$

where *M* is the multiplicity of the number of unit cells in the crystal. For the convenience of comparing the estimated x-ray diffraction intensity using Eq. (2) with experimental data, the M is approximately replaced by the number of atoms on a plane of Miller index ***G*** in the crystal, which is proportional to the number of unit cells. To determine the number, the following assumptions were also made: (1) the structure of the QD is a perfect sphere with radius, *r*, and (2) the density of atom, D_A, within the volume of the QD is homogeneous. By using the assumptions, the total number of atoms on the surfaces with the same Miller index can be determined. For the case of (002) surfaces, the total number of atoms, $N_{(002)}$, is expressed as the sum of number of atoms on a set of parallel circles, which belong to the group of (002) surfaces,

$$\begin{aligned}
N_{(002)} &\sim 2\times\{D_A\times[(r\cos\theta_1)^2+(r\cos\theta_2)^2+\cdots+(r\cos\theta_n)^2]\} \\
&= 2D_A r^2 \sum_{m=1}^{n} \left(1-\frac{d_m^2}{r^2}\right) \\
&= 2D_A r^2 \sum_{m=1}^{n} \left[1-\frac{1}{r^2}\left((m-1)\frac{c}{2}+\frac{5}{16}c\right)^2\right] \qquad , \\
&= 2D_A r^2\left[n-\frac{c^2}{4r^2}\left(\frac{n(n+1)(2n+1)}{6}-\frac{3}{4}\frac{n(n+1)}{2}+\sum_{m=1}^{n}\frac{9}{64}\right)\right] \\
&\propto n-\frac{c^2}{4r^2}\left[\frac{n(n+1)(2n+1)}{6}-\frac{3}{4}\frac{n(n+1)}{2}+\frac{9}{64}n\right]
\end{aligned} \tag{3}$$

where d_m is the perpendicular distance between the *m*-th circle and the circle passing through the center of the sphere, *n* is the total number of circles. Similarly, if the expression of d_m for the (*hkl*) plane is known, the $N_{(hkl)}$ can be calculated using Eq. (3). The results of a few planes are shown in Table 3.1, and compared with the measured result in the literature[1].

The Table 3.1 shows the calculated results, which are needed for the comparison with the WAXS data deduced from Murray's thesis[1], of the CdSe QD shown in Fig. 3.1. The table contains (1) the number (in the unit of $N_{(hkl)}/D_A r^2$) of each significant plane mentioned earlier, (2) the calculated unit cell structure factor, (3) the calculated intensity of x-ray diffraction using Eq. (2), and (4) the experimental data of Muray's[1], where the QD contained about 10000 atoms, and its aspect ratio was 1.3. The diffraction intensities of each facet in (3) and (4) are normalized w.r.t. the intensity of the (110) plane. The ratio of f_{Se}/f_{Cd} for the unit cell structure factor in Table 3.1 is approximately selected as the ratio of their atomic number[7], namely Z_{se}/Z_{cd}, which is the value of atomic scattering factor at zero scattering angle. It can be seen in Table 3.1 that although the ratio of the calculated intensities for each peak is different from that of the measured intensities, the ratio between (100) and (200) is similar to that in experiments. Among the measured values[1], (103) has a comparable intensity with (101), while in the calculated values (103) is twice larger than (101). This unexpected phenomenon can be caused by the stacking fault[6] in (103) in CdSe QDs[2], which makes the measured (103) peak broaden in diffraction angles and lower in intensity[6], while the calculated structure in Fig 3.1 is a perfect Wurtzite.

In summary, ellipsoidal CdSe QDs can be generated by using the author's program, and their shape are created partially based on some of the experimental findings. Moreover, an approximate method is used to determine the facets in a calculated QD structure. Although the experimental results are not completely reproduced, further modification to the approximation made in this section, such as the ratio of atomic scattering factors, could help identify the structure of QDs.

Permanent Dipole Moment in Semiconductor Quantum Dots

Since the structure of generated QDs is approximately a prolate ellipsoid, as shown in Fig. 3.1, there should be a permanent dipole moment along the *c* axis of the QDs, as suggested in the literature[8,9]. The calculation of the dipole moment $\boldsymbol{P}$ is approximated by the formula:

$$\boldsymbol{P}=\sum_i q_{cation}\boldsymbol{r}_i+\sum_j q_{anion}\boldsymbol{r}_j \quad , \tag{5}$$

where $\boldsymbol{r}$ are the position vectors, $\{x, y, z\}$, of each atom, q is the formal charge of the atom. As an approximation, the q_{cation} is assumed to be +2 while the q_{anion} is assumed to be -2. The calculated result of $\boldsymbol{P}$ of a WZ unit cell, which includes two anions and two cations, a QD with the structure in Fig. 3.1, and the structure composed of the complete unit cells within the structure in Fig. 3.1.

Even though there is no measured dipole moment reported in the literature of the size of QD shown in Table 2, the absolute value of calculated value of P_z in the second column is slightly larger than that in the third column, which suggests that P_z in the second column should be a correct estimate since the atoms in the incomplete unit cells

(2636 atoms in total) should add more contribution to the P_z.

The dipole moment of QD in Fig. 3.1 can also be estimated by extrapolating the volume dependence, $\mu(V) \approx 17.14\, V^{0.3756}$ (fitted by the author), in the literature[8]. Using the equation above, the upper limit of the dipole moment of 156.9 Debye was obtained, which is about 32.09% of the value in the estimated value of 489 Debye. The volume used to calculate the upper limit was using the *c* axis of the QD in Fig 3.1 as the radius. The discrepancy between the two dipole moments could come from (1) that there are organic ligands, TOPO, capping the surface of the QDs, which could compensate the extra charge, (2) the structure relaxation was not taken into account for the QDs in Fig. 3.1, and (3) the formal charges (±2) used earlier to estimate the dipole moment too large for the actual situation.

Therefore, to better estimate the dipole moment of a QD, the author plan to look into the charge distribution of a QD, such as the Mulliken charge distribution[10]. For the Mulliken charge distribution, in the current TB scheme, for a given atom in a QD, one could sum (1) the coefficient square of all the AOs on that atom (the “net atomic population”[10]) and (2) the overlap integral of the AOs between that atom and its adjacent atoms (the “overlap population”[10]), and deduct the sum of (1) and (2) from the nuclei charge of that atom to obtain the charge distribution on each atom.

Band Gap of Semiconductor Quantum Dots

Another important property of the QDs used in this dissertation is the band gap, which decreases as the size of a QD increases due to the decrease of the quantum confinement until some limiting value is reached for the bulk crystal. The band gap can be used to estimate the first peak of the absorption spectrum.

The values of TB parameters given in the previous chapter are the same as Albe *et al.*'s work[11], so their calculated band gaps provide a good benchmark to compare with. The values of the band gap of QDs in Fig. 3.2 are obtained by calculating the energy difference between the first CB state above the band gap and the first VB state below the band gap. It can be seen in Fig. 3.2 that the calculated values (filled magenta circles) of band gap in this dissertation show a similar trend as that of Albe *et al.*'s work[11] (dashed black line) within the range of interest even though the geometry of the QD in Albe *et al.*'s paper is ZB instead of WZ. However, it can be seen that the energy difference between the two curves is not negligible, and the deviation ranges between around 0.48 to 0.58 eV. There is another calculated curve of CdSe QDs done by Lippens and Lannoo[12] (filled green triangles) shown in Fig. 3.2 for comparison, and it has a difference from experimental values, caused by lacking of spin-orbit coupling[11].

One of the sources of the difference between the author's value and Albe *et al.*'s work[11] could be that to better compare with the experimental value, the Coulomb interaction within exicton was taken into consideration as a perturbation in their work[13], and the size-dependent interaction was modeled by $E'_g(d) = E_g(d) - (3.572\, e^2/\epsilon\, d)$ [11, 13], where E_g is the unperturbed band gap, d is the diameter of the QD, and ε is the dielectric constant of the material. If the equation above is applied to our calculated values and the dielectric constant of bulk CdSe ($\varepsilon = 6.25$)[14] is used, the adjusted curve (filled wine diamonds) is obtained. The deviation between the olive line and the black line in Fig. 3.2

then reduces to 0.33 eV. This difference is further reduced by introducing another source of the difference, the spin-orbit coupling, which is not included in our calculation. According to Albe *et al.*'s calculation[11], for a 2-nm-diameter CdSe QD, its band gap is reduced by an amount of 0.28 eV when considering the spin-orbit coupling. A much better agreement with Albe *et al.*'s work is obtained if the same spin-orbit coupling is applied to all sizes of the QD, as shown in Fig. 2 (filled red down triangles).

One notices in Fig. 3.2 that the measured bang gap by Katari *et al.*[15] approaches a constant value around 2 eV, but still 0.2 eV higher than the bulk value. The small energy difference indicates that for CdSe QDs with a diameter larger than the exciton Bohr radius (5.4 nm for CdSe)[16], the quantum confinement still has an intermediate effect.

To summarize the above discussion, the size dependence of the band gap in our calculated result has a qualitative agreement with other calculated results. Although there is a deviation on numerical values, the difference could be adjusted by including the more special effects, which are not expected to be important to the present focus, the calculation of the Auger lifetimes.

Molecular Orbitals of Semiconductor Quantum Dots

A widely-used model to describe the electronic structure of QDs is the particle-a-sphere model, and it has been providing a simple but good qualitative description, such as the discrete electronic states and the effect of quantum confinement.[17,18,19] In this description, the wave functions are expressed in terms of the product of the spherical Bessel function (radial part) and the spherical harmonics (angular part)[17, 20], i.e.

$\psi_{n,l,m}(r)=j_l(k_{n,l}r)Y_l^m(\theta,\phi)$, which is usually referred to as "envelope functions".[18,21] It would then be expected that the frontier states can be characterized by the combinations of quantum numbers, i.e. *n*, *l*, and *m*, in those functions.[17] For spherical Bessel functions, each *n* permits many choices of *l*, so unlike hydrogen atom, the labeling of molecular orbitals (MOs) could have more varieties, such as 1S, 1P, 1D, 2S. This terminology is now accepted as the common language to refer electronic states in QDs.[22] When atomic orbitals (AOs) of atoms are introduced into theoretical models, like effective-mass-approximation (EMA) method, as Bloch functions[20, 22], the electronic wave functions are expressed as the product of the envelope function and the Bloch functions[20,22]. However, for the TB method, the one used in this dissertation, the description of the envelope function is not explicitly used: the wave functions are instead described only by the linear combination of AOs (LCAO), and the coefficient in each atomic basis is the approximate value of the envelope function by each AO at that atom.

An example of the frontier MOs of a CdSe QD (radius ~1.75 nm) is shown in Fig. 3.3: the first five states above the edge of CB (C_1 to C_5, C_1 has the lowest energy) and the first five states below the edge of VB (V_1 to V_5, V_1 has the highest energy) are calculated by the basis set STO-3G[23], and the parameters of the Gaussian functions for the calculation are shown in Table 3.4. The MO of the CB states (from lower energy to higher) starts with an *s* orbital, followed by a p_z orbital, then a p_x orbitals (the degenerate p_y is not shown), a d_{z^2} , and one of the four other *d* orbitals (the other three degenerate *d* orbitals are not shown). This result is consistent with the theoretical prediction of envelope functions in the particle-a-sphere model.

As for VB states, it is seen in Fig. 3.3 that the valence states are highly oscillating with many nodal planes, while the conduction states are not. The reason behind the oscillation of the envelope function is because the highest state filled with electrons should have the most number of nodal planes among valence eigenstates, for example, if one considers a one-dimensional case of linear combination of atomic orbitals, where the state with the highest energy should be the one with all possible nodes. The envelope function of V_1 (A_2 symmetry) can hardly be categorized into any orbital symmetry, while V_2 and V_3 are likely categorized into *S*-like state, V_4 is *P*-like, and V_5 is *D*-like. This result is not similar to the spatial distribution of the five lowest hole states for a spherical CdSe QD in Schulz and Czycholl's study[24] (Fig. 8 in their work), where the first four hole states cannot be classified into any S-like or *P*-like state, while the fifth state is *P*-like. Schulz and Czycholl suggested that the intermixing between states in the VB makes it difficult to identify the state symmetry.

Analyzing the composition of AOs in these MOs, one would find that for the states near the edge of the CB, the primary contribution is from the *s* orbital on Cd's, ranging from 54.8% to 68.2%, while for the VB states, the primary contribution is from the *p* orbitals on Se's, ranging from 69.6% to 72.4%, and partially from Cd's *s* and *p* orbitals, which is consistent with the conclusion from other calculated results[25].

Density of States of Semiconductor Quantum Dots

It has been noted that the electronic states of semiconductor QDs are discrete due to the quantum-size effect.[26] The large spacing between states increases the significance of phonons in the electronic dynamics. Therefore, understanding the distribution of the electronic states in CB and VB would benefit the treatment of the detailed dynamics, especially when the Auger process we are interested in this dissertation involves states deep in the CB/VB.[27,28,29]

The calculated result of the density of states (DOS) of a CdSe QD of radius ~1.17 nm is shown in Fig. 3.4(a), (b) and (c). Each bar in Fig. 3.4(a) and (b) represents the number of states within a 50 meV energy window. It can be seen in Fig. 3.4(b) that adding an artificial layer removes the band gap states in Fig. 3,4(a). The fitting curve (red solid line in Fig. 3.4(c)) is obtained by convoluting a Gaussian function (FWHM =50 meV) with each bar in Fig. 3.4(b) and by adjusting the height of the peak around 2.2 eV to the peak of Pokrant and Whaley around 2.5 eV. This fitting curve is compared with two other calculated results in Fig 3.4(c), one using TB[30] (the black dashed line) and the other using density functional theory (DFT)[31] (the blue dot line). The FWHM of the Gaussian function is selected by estimating the FWHM of the peak near 2.5 eV in Pokrant and Whaley's work[30] because that peak should represent the single $1S_e$ state. The calculated result in Fig. 3.4 contains 350 atoms, including Cd's and Se's, while the QD in the TB result by Pokrant and Whaley has 384 atoms.

The similarity between the two TB results in Fig. 3.4(c) suggests that the calculated eigenstates and eigenvalues in this thesis can be regarded as reliable. One item to notice is that although the QD in the DFT result only contains 66 atoms, there is still a significant discrepancy between the two TB results in Fig. 3.4(c) and the DFT result: (1) the relative amplitude of CB to that of VB has a different trend and (2) there is no obvious energy gap in the deep band in the DFT result. Considering that the FWHMs of the first peak in the DOS in the three calculated results are similar, the possible explanation is that there are only valence orbitals considered in the TB method while there are more electronic states considered in DFT method and the repulsion between states makes the gaps not obvious.

Absorption Spectrum of Semiconductor Quantum Dots

One essential parameter to obtain a calculated absorption spectrum is the dimensionless quantity, the oscillator strength f_{ab}, between the initial state *a* and the final state *b*, and it is expressed as,

$$f_{ab}=\frac{2}{3}\frac{m_e}{\hbar^2}(E_a-E_b)\sum_{k=x,y,z}\left|\langle\psi_a|\hat{\boldsymbol{r}}_k|\psi_b\rangle\right|^2 \quad , \tag{6}$$

where m_e is the electron mass, *e* is the electron charge, E_a and E_b are the energy of state ψ_a and ψ_b, respectively, $\hat{\boldsymbol{r}}_k$ is the position operator in *x*, *y*, or *z* direction, and $\langle\psi_a|\hat{\boldsymbol{r}}_k|\psi_b\rangle$ is the transition dipole moment, which can be expressed as the sum of atomic transition dipole moments,

$$\langle\psi_a|\hat{\boldsymbol{r}}_k|\psi_b\rangle=\sum_{m,m'}\sum_{i,j}c_{m,i}^{a*}c_{m',j}^{b}\left\langle\phi_{m,i}^{a*}\middle|\hat{\boldsymbol{r}}_k\middle|\phi_{m',j}^{b}\right\rangle \tag{7}$$

when ψ_a and ψ_b are expressed in term of LCAO fashion, where $c_{m,i}^{a}$ and $c_{m',j}^{b}$ are the coefficients of the atomic orbital $\phi_{m,i}^{a}$ and $\phi_{m',j}^{b}$, respectively (*m* denotes the *m*-th atom). In this dissertation, the transition dipole moment is calculated using Eq. (3) in Pokrant and Whaley's work, and using the x component of Eq. (7) as an example,[30]

$$
\begin{aligned}
\langle\psi_a|\hat{\boldsymbol{r}}_x|\psi_b\rangle=&\sum_m\sum_{i,j}c^{a*}_{m,i}c^{b}_{m,j}\left\langle\phi^{a*}_{m,i}\middle|\hat{\boldsymbol{r}}_x\middle|\phi^{b}_{m,j}\right\rangle \\
&+\sum_m\sum_{\Delta n}\sum_{i,j}c^{a*}_{m,i}c^{b}_{\Delta n,j}\left\langle\phi^{a*}_{m,i}\middle|\hat{\boldsymbol{r}}_x\middle|\phi^{b}_{\Delta n,j}\right\rangle\quad, \\
&+\sum_m r_{x,m}\sum_j c^{a*}_{m,j}c^{b}_{m,j}
\end{aligned}
\qquad (8)
$$

where Δn is the nearest neighbor of atom m, $r_{x,m}$ is the x component of the coordinates of atom m, and the rest of the notation has been defined in Eq. (7). An approximation[30] is made for an atomic transition dipole moment between two different sites that this kind of dipole moment can be interpreted as the sum of the local matrix element for each atom (namely the second term in Eq. (8)) because the off-site atomic transition dipole moments have translational invariant, and the selection of Δn is further limited to nearest neighbors. Pokrant and Whaley's work[30] suggested that the first term in Eq. (8) can be neglected because for a given excitation of electron (e.g. VB state $a \rightarrow$ CB state b), the primary wave function of the state a is on Se's, while that of the state b is on Cd's, so the transition dipole moment on the same atom should be small. In this dissertation, the author chose to keep all of terms in Eq. (8) to see if the inclusion of the first term still provides a reliable absorption spectrum.

The local atomic transition dipole moments, such as $\left\langle\phi^{a*}_{m,i}\middle|\hat{\boldsymbol{r}}_k\middle|\phi^{b}_{m,j}\right\rangle$ in Eq. (8), in the three Cartesian coordinates were calculated separately using the adaptive Simpson method, where $\phi^{a}_{m,i}$ and $\phi^{b}_{m',j}$ used 4 sp^3 lobes and 1 s^* orbital as the bases. The calculated values of $\left\langle\phi^{a*}_{m,i}\middle|\hat{\boldsymbol{r}}_k\middle|\phi^{b}_{m,j}\right\rangle$ and $\left\langle\phi^{a*}_{m,i}\middle|\hat{\boldsymbol{r}}_k\middle|\phi^{b}_{\Delta n,j}\right\rangle$ (k= x, y, or z) are shown in Tables 3.5 and 3.6. The on-site atomic transition dipole moments in Tables 3.5 and 3.6 are for Se atoms of orientation 1 and Cd atoms of orientation 2 (the orientations are defined in Fig. 2.3 in Chap 2), so for Se atoms of orientation 4 or Cd atoms of orientation

3, the on-site values need to be multiplied by -1. To use the pre-calculated values in Tables 3.5 and 3.6, for both ψ_a and ψ_b, the 5 AOs on each atom and their respective coefficients were transformed into 4 sp^3 lobes and an s^* orbital..

By using the values in Table 3.5, Table 3.6, and Eq. (8), the transition dipole moments for the selected pairs of ψ_a and ψ_b for a CdSe QD (radius ~ 1.17 nm) were calculated. In the theoretical scheme of EMA for a spherical QD[22], an intraband transition is allowed only when the envelope functions of the initial and the final states have the same quantum number *L*, e.g., an S hole state in the VB to an S electron state in the CB. In a prolate QD with the C_{3v} symmetry in this thesis, an analogy is made that only a transition, which involves two states belonging to the same irreducible representation, is allowed, i.e. A_1 to A_1, A_2 to A_2 or E to E. The calculated absorption spectrum is plotted in Fig. 3.5 and is compared with that of an experimental measurement by Katari *et al.*[15]. Each allowed transition is convoluted with a Gaussian function (FWHM = 0.15 eV), whose FWHM is chosen to fit the first peak of the measured spectrum of CdSe QDs (radius = 1.14 nm)[15]. There is a displacement of 0.84 eV between the first peaks of the calculated and measured results, and taking the interaction between electron-hole pair and the spin-orbit coupling into account, as discussed earlier in the band gap section, reduces the difference to 0.30 eV, which is more consistent with the result shown in Fig. 3.2. Further, if the amplitude of the calculated spectrum was modulated by a constant of 1/6, the intensity of the first peak of the calculated spectrum is able to match the scaled optical intensity of the first peak of the measured spectrum in Katari *et al.*'s study[15]. It can be seen in Fig. 3.5 that the major peaks of the measured spectrum (solid red line) are qualitatively reproduced by the calculated one (solid black line), except that the relative energy difference between the first peak and the rest peaks in the calculated result is larger than that in the Katari *et al.*'s result[15]. A possible reason is because the interaction between electron and hole in the exciton is omitted in the current model.

In principle, applying a selection rule to the pair of the states in a transition dipole moment has generated a reasonable absorption spectrum to compare with experimental measurement. The similarity between the two spectra indicates that the calculated eigenstates using the TB method mentioned in Chapter 2, not limited to band edge states, have qualitative consistency with the states in real QDs.

Summary

The results and their comparison with the results in respective literature suggests that the QDs generated by the author's program could provide a reliable basis for other theoretical calculations, such as the rate constants of the Auger processes in the next chapter.

Reference

1. Murray, C. B. Synthesis and characterization of II-IV quantum dots and their assembly into 3D quantum dot superlattices. Massachusetts Institute of Technology, 1995.
2. Murray, C. B.; Norris, D. J.; Bawendi, M. G., Synthesis and characterization of nearly monodisperse CdE (E = sulfur, selenium, tellurium) semiconductor nanocrystallites. *J Am Chem Soc* **1993,** *115* (19), 8706-8715.
3. Rossetti, R.; Ellison, J. L.; Gibson, J. M.; Brus, L. E., Size effects in the excited electronic states of small colloidal CdS crystallites. *J Chem Phys* **1984,** *80* (9), 4464-4469.
4. Peng, X.; Manna, L.; Yang, W.; Wickham, J.; Scher, E.; Kadavanich, A.; Alivisatos, A. P., Shape control of CdSe nanocrystals. *Nature* **2000,** *404* (6773), 59-61.
5. Als-Nielsen, J.; McMorrow, D., *Elements of modern X-ray physics*. John Wiley & Sons: 2011.
6. Guinier, A., *X-ray diffraction in crystals, imperfect crystals, and amorphous bodies*. New York : Dover, 1994: 1994.
7. Hammond, C.; Hammond, C., *The basics of crystallography and diffraction*. Oxford University Press Oxford: 2009.
8. Shim, M.; Guyot-Sionnest, P., Permanent dipole moment and charges in colloidal semiconductor quantum dots. *J Chem Phys* **1999,** *111* (15), 6955-6964.
9. Li, L.-s.; Alivisatos, A. P., Origin and Scaling of the Permanent Dipole Moment in CdSe Nanorods. *Phys Rev Lett* **2003,** *90* (9), 097402.
10. Mulliken, R. S., Electronic Population Analysis on LCAO–MO Molecular Wave Functions. I. *J. Chem. Phys.* **1955,** *23* (10), 1833-1840.
11. Albe, V.; Jouanin, C.; Bertho, D., Confinement and shape effects on the optical spectra of small CdSe nanocrystals. *Phys Rev B* **1998,** *58* (8), 4713-4720.
12. Lippens, P. E.; Lannoo, M., Comparison between Calculated and Experimental Values of the Lowest Excited Electronic State of Small Cdse Crystallites. *Phys Rev B* **1990,** *41* (9), 6079-6081.
13. Kayanuma, Y., Quantum-size effects of interacting electrons and holes in semiconductor microcrystals with spherical shape. *Phys Rev B* **1988,** *38* (14), 9797-9805.
14. Vaxenburg, R.; Rodina, A.; Shabaev, A.; Lifshitz, E.; Efros, A. L., Nonradiative Auger Recombination in Semiconductor Nanocrystals. *Nano Lett* **2015,** *15* (3), 2092-2098.
15. Katari, J. E. B.; Colvin, V. L.; Alivisatos, A. P., X-ray Photoelectron Spectroscopy of CdSe Nanocrystals with Applications to Studies of the Nanocrystal Surface. *J Phys Chem* **1994,** *98* (15), 4109-4117.
16. Landolt-Bornstein, N., Semiconductors, vol. 17. Springer, Berlin: 1982.
17. Efros, A. L., Interband Absorption of Light in a Semiconductor Sphere. *Sov Phys Semicond* **1982,** *16* (7), 772-775.
18. Nirmal, M.; Murray, C.; Bawendi, M., Fluorescence-line narrowing in CdSe quantum dots: Surface localization of the photogenerated exciton. *Phys Rev B* **1994,** *50* (4), 2293-2300.
19. Nirmal, M.; Brus, L., Luminescence Photophysics in Semiconductor Nanocrystals.

Accounts Chem Res **1999,** *32* (5), 407-414.
20. Chepic, D. I.; Efros, A. L.; Ekimov, A. I.; Vanov, M. G.; Kharchenko, V. A.; Kudriavtsev, I. A.; Yazeva, T. V., Auger Ionization of Semiconductor Quantum Drops in a Glass Matrix. *J Lumin* **1990,** *47* (3), 113-127.
21. Norris, D.; Bawendi, M., Measurement and assignment of the size-dependent optical spectrum in CdSe quantum dots. *Phys Rev B* **1996,** *53* (24), 16338.
22. Efros, A. L.; Rosen, M., The electronic structure of semiconductor nanocrystals. *Annu Rev Mater Sci* **2000,** *30*, 475-521.
23. Hehre, W. J.; Stewart, R. F.; Pople, J. A., self-consistent molecular-orbital methods. i. use of gaussian expansions of Slater-type atomic orbitals. *J Chem Phys* **1969,** *51* (6), 2657-2664.
24. Schulz, S.; Czycholl, G., Tight-binding model for semiconductor nanostructures. *Phys Rev B* **2005,** *72* (16).
25. Kobayashi, A.; Sankey, O. F.; Volz, S. M.; Dow, J. D., Semiempirical Tight-Binding Band Structures of Wurtzite Semiconductors - AlN, CdS, CdSe, ZnS, and ZnO. *Phys Rev B* **1983,** *28* (2), 935-945.
26. Alivisatos, A. P., Semiconductor Clusters, Nanocrystals, and Quantum Dots. *Science* **1996,** *271* (5251), 933-937.
27. Cohn, A. W.; Rinehart, J. D.; Schimpf, A. M.; Weaver, A. L.; Gamelin, D. R., Size Dependence of Negative Trion Auger Recombination in Photodoped CdSe Nanocrystals. *Nano Lett* **2014,** *14* (1), 353-358.
28. Jha, P. P.; Guyot-Sionnest, P., Trion Decay in Colloidal Quantum Dots. *Acs Nano* **2009,** *3* (4), 1011-1015.
29. Cragg, G. E.; Efros, A. L., Suppression of Auger Processes in Confined Structures. *Nano Lett* **2010,** *10* (1), 313-317.
30. Pokrant, S.; Whaley, K., Tight-binding studies of surface effects on electronic structure of CdSe nanocrystals: the role of organic ligands, surface reconstruction, and inorganic capping shells. *Eur Phys J D -Atomic, Molecular, Optical and Plasma Physics* **1999,** *6* (2), 255-267.
31. Kilina, S. V.; Craig, C. F.; Kilin, D. S.; Prezhdo, O. V., Ab Initio Time-Domain Study of Phonon-Assisted Relaxation of Charge Carriers in a PbSe Quantum Dot. *J Phys Chem C* **2007,** *111* (12), 4871-4878.
32. Hanwell, M. D.; Curtis, D. E.; Lonie, D. C.; Vandermeersch, T.; Zurek, E.; Hutchison, G. R., Avogadro: An advanced semantic chemical editor, visualization, and analysis platform. *J. Cheminformatics* **2012,** *4* (1), 17.
33. Slater, J. C., Atomic shielding constants. *Phys Rev* **1930,** *36* (1), 0057-0064.
34. Feller, D., The role of databases in support of computational chemistry calculations. *J COMPUT CHEM* **1996,** *17* (13), 1571-1586.
35. Schuchardt, K. L.; Didier, B. T.; Elsethagen, T.; Sun, L.; Gurumoorthi, V.; Chase, J.; Li, J.; Windus, T. L., Basis set exchange: a community database for computational sciences. *J of Chem Inf Model* **2007,** *47* (3), 1045-1052.
36. Humphrey, W.; Dalke, A.; Schulten, K., *VMD: visual molecular dynamics*. 1996; Vol. 14, p 33-38.
37. Prezhdo, O. V.; Kilina, S. V.; Kilin, D. S., Breaking the Phonon Bottleneck in PbSe

and CdSe Quantum Dots: Time-Domain Density Functional Theory of Charge Carrier Relaxation. *Acs Nano* **2009,** *3* (1), 93-99.

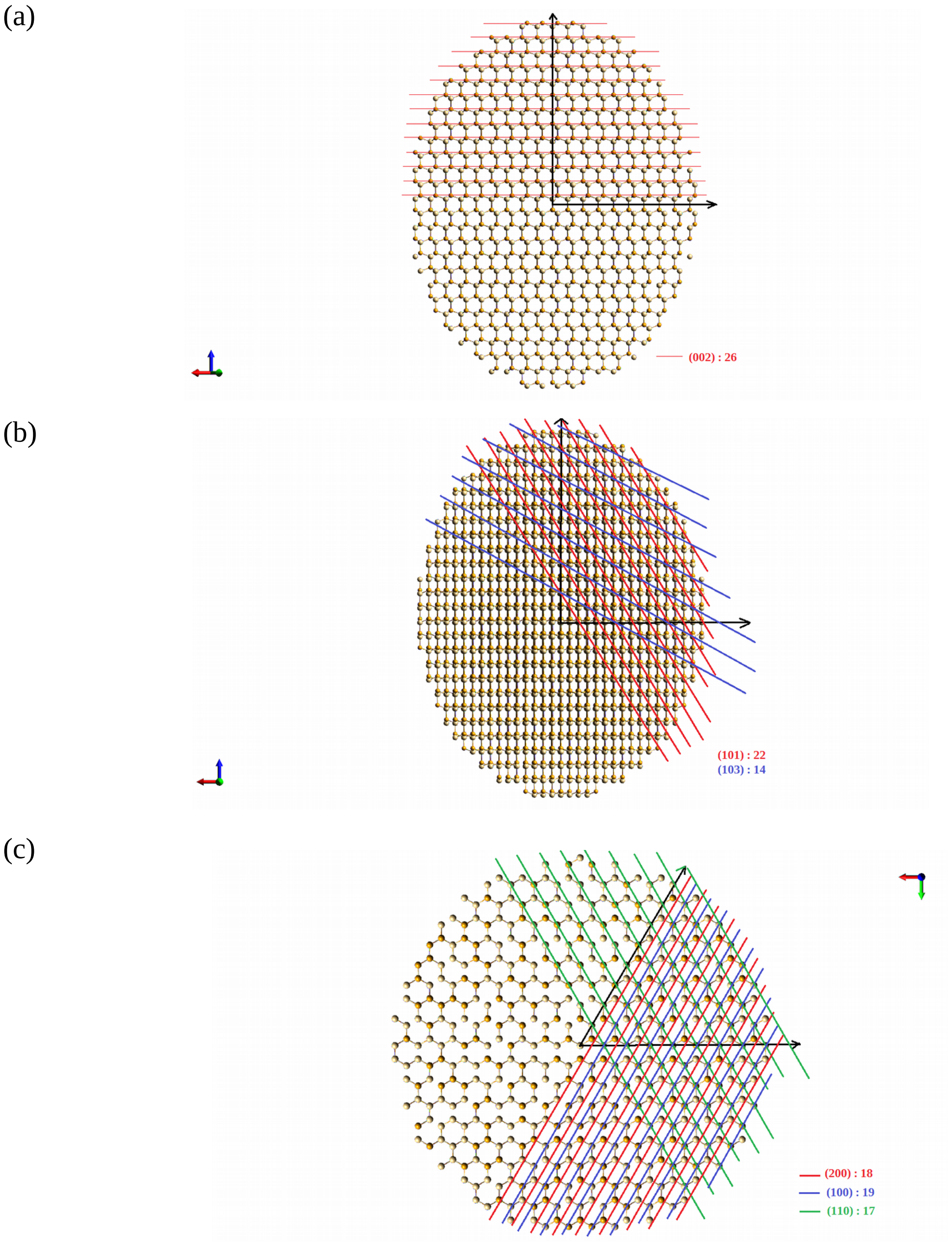

Fig. 3.1 The geometry of a CdSe QD with its radius ~ 3.73 nm (aspect ratio ~1.3). (a) & (b) side view (c) top view (looking down from *c* axis). The legend in each figure represent the Miller indexes for different surfaces, and the number represents total number of that surface. The structures of QD are plotted by the software Avogadro.[32]

Table 3.1 The comparison between the calculated and measured x-ray diffraction intensity

Miller Index of a surface	Average number of atoms ($N_{(hkl)}/D_A r^2$)	calculated unit cell structure factor by Eq. (2)	Prediction of the intensity	Relative intensity in the WAXS data[1]
(100)	13.90	$\lvert f_{Se}\rvert^2+\lvert f_{Cd}\rvert^2+2f_{Se}f_{Cd}$	0.27	0.67
(200)	13.32	$\lvert f_{Se}\rvert^2+\lvert f_{Cd}\rvert^2+2f_{Se}f_{Cd}$	0.26	0.60
(110)/ $(11\bar{2}0)$	12.93	$4\lvert f_{Se}\rvert^2+4\lvert f_{Cd}\rvert^2+8f_{Se}f_{Cd}$	1.0	1.0
(103)	6.364	$3\lvert f_{Se}\rvert^2+3\lvert f_{Cd}\rvert^2+4.24f_{Se}f_{Cd}$	0.32	0.40
(002)	12.71	$4\lvert f_{Se}\rvert^2+4\lvert f_{Cd}\rvert^2$	0.52	0.80
(101)	12.23	$3\lvert f_{Se}\rvert^2+3\lvert f_{Cd}\rvert^2-4.24f_{Se}f_{Cd}$	0.14	0.47

The comparison between the calculated x-ray diffraction intensity and measured intensity of WXAS[1] for the significant facets in a CdSe QD. The values in the fourth and the fifth column were normalized w.r.t. their respective intensity of (110)

Table 3.2 Calculated dipole moment in the unit of Debye for different CdSe Crystals in each dimension

		A single unit cell of WZ structure	CdSe QD in Fig. 3.1[^]	Collection of complete unit cells in QD in Fig. 3.1[*]
Number of atoms in the crystal		4	8378	5724
Calculated Dipole Moment (Debye)	$\lvert\mathbf{P}_x\rvert$	0.00	$2.14\text{x}10^{-4}$	0.00
	$\lvert\mathbf{P}_y\rvert$	0.00	$7.11\text{x}10^{-4}$	0.00
	$\lvert\mathbf{P}_z\rvert$	0.274	489	391

[^]: P_x and P_y of the QD in Fig. 3.1 are almost zero while P_z is as the same order as that in the third column, which is the expected result.

[*]:The collection of complete unit cells in the QD in Fig. 3.1 (the fourth column) has 5724/4 = 1431 complete unit cells, and its dipole moment is 1431 times that of a single unit cell.

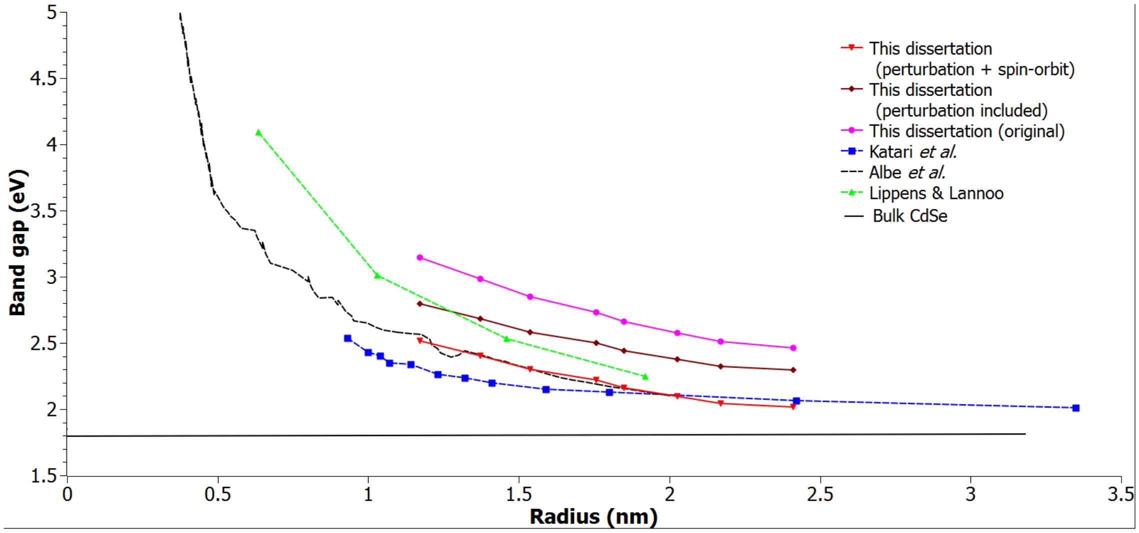

Fig. 3.2 The results of the band gap vs. radius of CdSe QDs of this dissertation: (1) the energy difference between the edge of CB and VB (filled circle and solid magenta line), (2) applying the perturbation introduced by Albe *et al.*[11] to the values in (1)(filled diamond and solid wine line), and (3) the values in (1) modified by the perturbation and the spin-orbit coupling[11] (down triangles and solid red line). The calculation of Albe *et al.*[11] (dash black line), the calculation of Lippens and Lannoo[12] (filled triangles and dash green line), and the measured absorption spectrum of Katari *et al.*[15] (dash blue line) are shown as the comparison. The band gap of CdSe bulk (1.8 eV) is shown as the solid black line.

Table 3.3 Parameters used for Slater-type orbitals (STO) used in this dissertation.

Cd				Se			
orbital	A*	n	Z	orbital	A*	n	Z
5s	0.0463662	4.0	4.35	4s	0.685560	3.7	6.95
5p	0.112687	4.0	4.00	4p	2.43025	3.7	6.95
6s	9.72143×10^{-8}	4.2	0.29988	5s	3.86448×10^{-5}	4.0	0.900

The definition of *n* and *Z* can be found in Slater's study[33].

*: *A* is the normalization constant.

Table 3.4 The exponents and the contraction coefficients of the STO-3G basis for Cd and Se

Atom	Valence Orbital	Exponent	Contraction Coefficient
Cd	5s	0.5949150981	-0.3842642607
		0.3203250000	-0.1972567438
		0.1414931855	1.3754955120
	5p	0.5949150981	-0.3481691526
		0.3203250000	0.6290323690
		0.1414931855	0.6662832743
Se	4s	1.2146442970	-0.3088441215
		0.4482801363	0.0196064117
		0.1979652346	1.1310344420
	4p	1.2146442970	-0.1215468600
		0.4482801363	0.5715227604
		0.1979652346	0.5498949471

The values are from EMSL Basis set exchange (https://bse.pnl.gov/bse/portal)[34,35].

Conduction Band			Valence Band		
	Top view (*c* axis)	Side view		Top view (*c* axis)	Side view
C$_5$	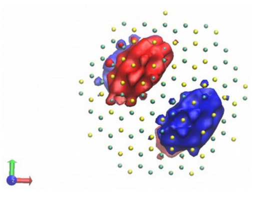	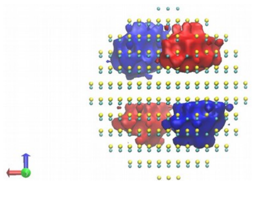	V$_1$	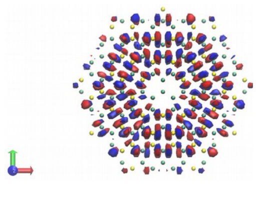	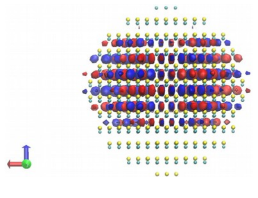
C$_4$	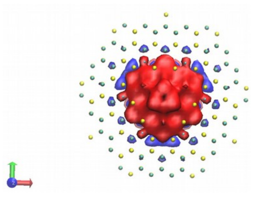	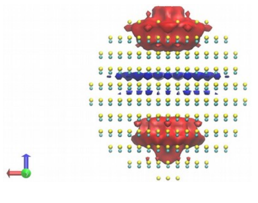	V$_2$	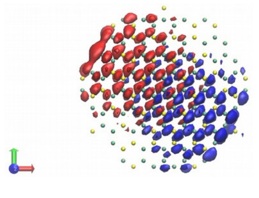	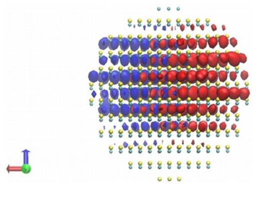
C$_3$	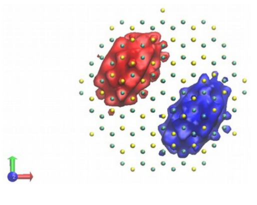	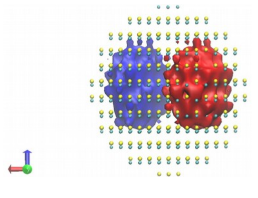	V$_3$	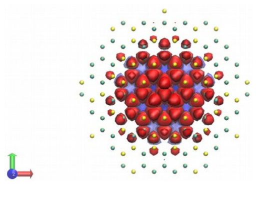	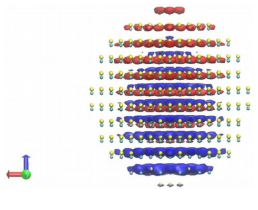
C$_2$	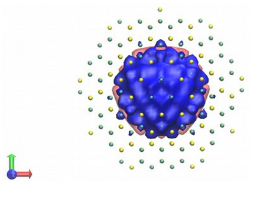	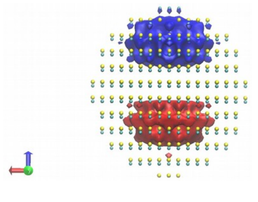	V$_4$	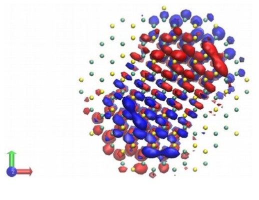	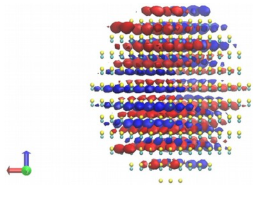
C$_1$	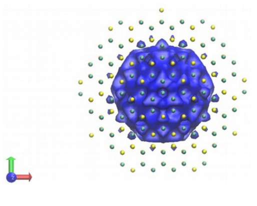	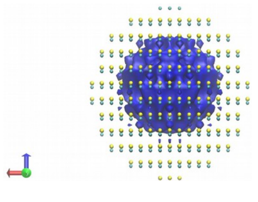	V$_5$	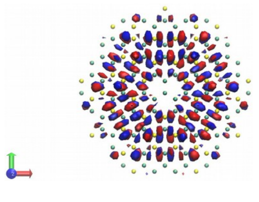	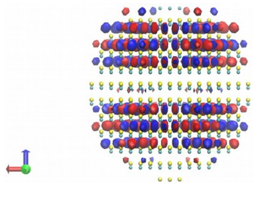

Fig. 3.3 The molecular orbitals of the first five states in the conduction band above the edge of CB and the first five states in the valence band below the edge of VB, respectively. The isoValue for the CB states is 0.015 $\mathring{A}^{-3}$ while that for the VB states is 0.005 $\mathring{A}^{-3}$. The molecular orbitals are generated by the software Visual Molecular Dynamics (VMD).[36]

Table 3.5 The matrix of atomic transition dipole moments of Se

An Se atom as the center atom (x component)						
		Lobe 1	Lobe 2	Lobe 3	Lobe 4	s*
The two atomic orbitals on the same atom (on-site)	Lobe 1	0.913	0.000	0.456	0.456	0.0186
	Lobe 2	0.000	-0.913	-0.456	-0.456	-0.0186
	Lobe 3	0.456	-0.456	0.000	0.000	0.000
	Lobe 4	0.456	-0.456	0.000	0.000	0.000
	s*	0.0186	-0.0186	0.000	0.000	-0.00043
The Nearest neighbor (Cd) in Vector 1	Lobe 1	0.537	0.568	0.132	0.133	0.00016
	Lobe 2	-0.877	-0.0750	-0.0830	-0.0833	-0.00031
	Lobe 3	0.0201	0.293	-0.143	0.0709	-0.00009
	Lobe 4	0.0200	0.293	0.0708	-0.143	-0.00009
	s*	-0.236	0.473	0.149	0.149	-0.155
The Nearest neighbor (Cd) in Vector 2	Lobe 1	0.0750	0.877	0.0830	0.0833	0.00031
	Lobe 2	-0.568	-0.537	-0.132	-0.133	-0.00016
	Lobe 3	-0.293	-0.0201	0.143	-0.0709	0.00009
	Lobe 4	-0.293	-0.0200	-0.0708	0.143	0.00009
	s*	-0.473	0.236	-0.149	-0.149	0.150
The Nearest neighbor (Cd) in Vector 3	Lobe 1	-0.0682	0.376	0.897	0.154	0.00022
	Lobe 2	-0.376	0.0682	-0.897	-0.154	0.00022
	Lobe 3	-0.436	0.436	0.000	0.000	0.000
	Lobe 4	-0.222	0.222	0.000	0.000	0.000
	s*	-0.324	0.324	0.000	0.000	0.00264
The Nearest neighbor (Cd) in Vector 4	Lobe 1	0.376	-0.0681	0.154	0.897	0.00022
	Lobe 2	0.0681	-0.376	-0.154	-0.897	-0.00022
	Lobe 3	0.222	-0.222	0.000	0.000	0.000
	Lobe 4	0.436	-0.436	0.000	0.000	0.000
	s*	0.324	-0.324	0.000	0.000	-0.00264

The values (in atomic unit) in the table are for various combinations of sp^3 lobes/s* orbital of a Se atom and the matrices of the Se and its neighbor Cd's in the three Cartesian coordinates.

(contd.)

Table 3.5 *(contd.)* The matrix of atomic transition dipole moments of Se

An Se atom as the center atom (y component)						
		Lobe 1	Lobe 2	Lobe 3	Lobe 4	s*
The two atomic orbitals on the same atom (on-site)	Lobe 1	-0.527	-0.527	0.264	-0.264	-0.0107
	Lobe 2	-0.527	-0.527	0.264	-0.264	-0.0107
	Lobe 3	0.264	0.264	1.05	0.527	0.0215
	Lobe 4	-0.264	-0.264	0.527	0.000	0.000
	s*	-0.0107	-0.0107	0.0215	0.000	-0.00043
The Nearest neighbor (Cd) in Vector 1	Lobe 1	-0.310	0.175	-0.580	-0.0765	-0.00009
	Lobe 2	-0.530	0.122	-0.386	-0.130	-0.00008
	Lobe 3	1.02	0.265	0.00395	0.137	0.00031
	Lobe 4	-0.0115	0.0874	-0.297	0.0827	0.00005
	s*	0.136	0.101	-0.459	0.0858	0.0856
The Nearest neighbor (Cd) in Vector 2	Lobe 1	0.122	-0.530	-0.386	-0.130	-0.00008
	Lobe 2	0.175	-0.310	-0.580	-0.0765	-0.00009
	Lobe 3	0.265	1.02	0.00395	0.137	0.00031
	Lobe 4	0.0874	-0.0115	-0.297	0.0827	0.00005
	s*	0.101	0.136	-0.460	-0.0858	0.0856
The Nearest neighbor (Cd) in Vector 3	Lobe 1	-0.126	0.121	-0.495	-0.00714	-0.00023
	Lobe 2	0.121	-0.126	-0.495	-0.00714	-0.00023
	Lobe 3	0.404	0.404	0.621	0.153	0.00018
	Lobe 4	0.210	0.210	0.0231	-0.165	-0.00010
	s*	0.359	0.359	-0.272	0.172	-0.179
The Nearest neighbor (Cd) in Vector 4	Lobe 1	-0.217	-0.217	0.168	-0.518	-0.00013
	Lobe 2	-0.217	-0.217	0.168	-0.518	-0.00013
	Lobe 3	0.0497	0.0497	0.435	1.04	0.00026
	Lobe 4	-0.252	-0.252	0504	0.000	0.000
	s*	-0.187	-0.187	0.374	0.000	-0.00264

(contd.) The values (in atomic unit) in the table are for various combinations of sp^3 lobes/s* orbital of a Se atom and the matrices of the Se and its neighbor Cd's in the three Cartesian coordinates.

(contd.)

Table 3.5 *(contd.)* The matrix of atomic transition dipole moments of Se

An Se atom as the center atom (z component)						
		Lobe 1	Lobe 2	Lobe 3	Lobe 4	s*
The two atomic orbitals on the same atom (on-site)	Lobe 1	-0.373	-0.373	-0.373	-0.373	-0.00759
	Lobe 2	-0.373	-0.373	-0.373	-0.373	-0.00759
	Lobe 3	-0.373	-0.373	-0.373	-0.373	-0.00759
	Lobe 4	0.373	0.373	0.373	1.12	0.0228
	s*	-0.00759	-0.00759	-0.00759	0.0228	-0.00043
The Nearest neighbor (Cd) in Vector 1	Lobe 1	-0.219	0.124	0.124	-0.588	-0.00006
	Lobe 2	-0.374	0.0862	-0.00102	-0.364	-0.00005
	Lobe 3	-0.374	-0.00102	0.0862	-0.364	-0.00005
	Lobe 4	1.09	0.250	0.250	-0.0248	0.00031
	s*	0.0964	0.0718	0.0718	-0.458	0.0597
The Nearest neighbor (Cd) in Vector 2	Lobe 1	0.0862	-0.374	-0.00102	-0.364	-0.00005
	Lobe 2	0.124	-0.220	0.124	-0.588	-0.00006
	Lobe 3	-0.00102	-0.374	0.0862	-0.364	-0.00005
	Lobe 4	0.250	1.09	0.250	-0.0248	0.00031
	s*	0.0718	0.0962	0.0718	-0.458	0.0597
The Nearest neighbor (Cd) in Vector 3	Lobe 1	0.0862	-0.00102	-0.374	-0.364	-0.00005
	Lobe 2	-0.00102	0.0862	-0.374	-0.364	-0.00005
	Lobe 3	0.124	0.124	-0.219	-0.588	-0.00006
	Lobe 4	0.250	0.250	1.09	-0.0248	0.00031
	s*	0.0718	0.0718	0.0964	-0.458	0.0597
The Nearest neighbor (Cd) in Vector 4	Lobe 1	0.202	-0.0602	-0.0602	-0.342	-0.00020
	Lobe 2	-0.0602	0.202	-0.0602	-0.342	-0.00020
	Lobe 3	-0.0602	-0.0602	0.202	-0.342	-0.00020
	Lobe 4	0.340	0.340	0.340	0.657	0.00019
	s*	0.314	0.314	0.314	-0.289	-0.189

(contd.) The values (in atomic unit) in the table are for various combinations of sp^3 lobes/s* orbital of a Se atom and the matrices of the Se and its neighbor Cd's in the three Cartesian coordinates.

Table 3.6 The matrix of atomic transition dipole moments of Cd

A Cd atom as the center atom (x component)						
		Lobe 1	Lobe 2	Lobe 3	Lobe 4	s*
The two atomic orbitals on the same atom (on-site)	Lobe 1	-1.75	0.000	-0.873	-0.873	-0.00447
	Lobe 2	0.000	1.75	0.873	0.873	0.00447
	Lobe 3	-0.873	0.873	0.000	0.000	0.000
	Lobe 4	-0.873	0.873	0.000	0.000	0.000
	s*	-0.00447	0.00447	0.000	0.000	-0.0231
The Nearest neighbor (Se) in Vector 1	Lobe 1	-0.105	-1.79	-0.893	-0.893	-0.271
	Lobe 2	0.250	0.493	-0.0967	-0.0966	0.357
	Lobe 3	-0.186	0.472	0.425	-0.319	0.0323
	Lobe 4	-0.186	0.472	-0.319	0.425	0.0323
	s*	0.00018	-0.00052	-0.00030	-0.00030	-0.603
The Nearest neighbor (Se) in Vector 2	Lobe 1	-0.493	-0.250	0.0967	0.0966	-0.357
	Lobe 2	1.79	0.105	0.893	0.893	0.271
	Lobe 3	0.472	0.186	-0.425	0.319	-0.0323
	Lobe 4	0.473	0.186	0.319	-0.425	-0.0323
	s*	0.00052	-0.00018	0.00030	0.00030	0.603
The Nearest neighbor (Se) in Vector 3	Lobe 1	-0.0682	-0.376	-0.436	-0.222	-0.323
	Lobe 2	0.376	0.0682	0.436	0.222	0.324
	Lobe 3	0.897	-0.897	0.000	0.000	0.000
	Lobe 4	0.154	-0.154	0.000	0.000	0.000
	s*	0.00022	-0.00022	0.000	0.000	-0.00001
The Nearest neighbor (Se) in Vector 4	Lobe 1	-0.376	-0.0681	-0.222	-0.436	-0.324
	Lobe 2	0.0681	0.376	0.222	0.436	0.324
	Lobe 3	-0.154	0.154	0.000	0.000	0.000
	Lobe 4	-0.897	0.897	0.000	0.000	0.000
	s*	-0.00022	0.00022	0.000	0.000	-0.00001

The values (in atomic unit) in the table are for various combinations of sp^3 lobes/s* orbital of a Cd atom and the matrices of the Cd and its neighbor Se's in the three Cartesian coordinates.

(contd.)

Table 3.6 *(contd.)* The matrix of atomic transition dipole moments of Cd

A Cd atom as the center atom (y component)						
		Lobe 1	Lobe 2	Lobe 3	Lobe 4	s*
The two atomic orbitals on the same atom (on-site)	Lobe 1	1.01	1.01	-0.504	0.504	0.00258
	Lobe 2	1.01	1.01	-0.504	0.504	0.00258
	Lobe 3	-0.504	-0.504	-2.02	-1.01	-0.00516
	Lobe 4	0.504	0.504	-1.01	0.000	0.000
	s*	0.00258	0.00258	-0.00516	0.000	-0.0231
The Nearest neighbor (Se) in Vector 1	Lobe 1	0.0605	-0.00252	1.55	0.516	0.157
	Lobe 2	0.359	-0.206	0.490	0.312	0.169
	Lobe 3	-0.396	-0.161	-0.324	-0.0724	-0.393
	Lobe 4	0.107	0.0951	0.362	-0.245	-0.0187
	s*	-0.00010	0.00004	0.00043	0.00017	0.348
The Nearest neighbor (Se) in Vector 2	Lobe 1	-0.206	0.359	0.490	0.312	0.169
	Lobe 2	-0.00252	0.0605	1.55	0.516	0.157
	Lobe 3	-0.161	-0.396	-0.324	-0.0724	-0.393
	Lobe 4	0.0951	0.107	0.362	-0.245	-0.0187
	s*	0.00004	-0.00010	0.00043	0.00017	0.348
The Nearest neighbor (Se) in Vector 3	Lobe 1	0.530	-0.329	0.0370	-0.240	0.225
	Lobe 2	-0.329	0.530	0.0370	-0.240	0.225
	Lobe 3	-1.55	-1.55	-0.121	-1.03	-0.313
	Lobe 4	-0.457	-0.457	-0.215	0.490	0.0373
	s*	-0.00048	-0.00048	0.00021	-0.00035	-0.696
The Nearest neighbor (Se) in Vector 4	Lobe 1	0.217	0.217	-0.0497	0.252	0.187
	Lobe 2	0.217	0.217	-0.0497	0.252	0.187
	Lobe 3	-0.168	-0.168	-0.435	-0.504	-0.374
	Lobe 4	0.518	0.518	-1.04	0.000	0.000
	s*	0.00013	0.00013	-0.00026	0.000	-0.00001

The values (in atomic unit) in the table are for various combinations of sp^3 lobes/s* orbital of a Cd atom and the matrices of the Cd and its neighbor Se's in the three Cartesian coordinates.

(contd.)

Table 3.6 *(contd.)* The matrix of atomic transition dipole moments of Cd

A Cd atom as the center atom (z component)						
		Lobe 1	Lobe 2	Lobe 3	Lobe 4	s*
The two atomic orbitals on the same atom (on-site)	Lobe 1	0.713	0.713	0.713	-0.713	0.00182
	Lobe 2	0.713	0.713	0.713	-0.713	0.00182
	Lobe 3	0.713	0.713	0.713	-0.713	0.00182
	Lobe 4	-0.713	-0.713	-0.713	-2.14	-0.00547
	s*	0.00182	0.00182	0.00182	-0.00547	-0.0231
The Nearest neighbor (Se) in Vector 1	Lobe 1	0.0424	-0.00220	-0.00220	1.46	0.111
	Lobe 2	0.254	-0.145	0.158	0.409	0.119
	Lobe 3	0.254	0.158	-0.145	0.409	0.119
	Lobe 4	-0.458	-0.205	-0.205	-0.256	-0.410
	s*	-0.00007	0.00003	0.00003	0.00040	0.246
The Nearest neighbor (Se) in Vector 2	Lobe 1	-0.145	0.254	0.158	0.409	0.119
	Lobe 2	-0.00220	0.0424	-0.00220	1.46	0.111
	Lobe 3	0.158	0.254	-0.145	0.409	0.119
	Lobe 4	-0.205	-0.458	-0.205	-0.256	-0.410
	s*	0.00003	-0.00007	0.00003	0.00040	0.246
The Nearest neighbor (Se) in Vector 3	Lobe 1	-0.145	0.158	0.254	0.409	0.119
	Lobe 2	0.158	-0.145	0.254	0.409	0.119
	Lobe 3	-0.00220	-0.00220	0.0424	1.46	0.111
	Lobe 4	-0.205	-0.205	-0.458	-0.256	-0.410
	s*	0.00003	0.00003	-0.00007	0.00040	0.246
The Nearest neighbor (Se) in Vector 4	Lobe 1	-0.666	0.244	0.244	-0.0493	0.172
	Lobe 2	0.244	-0.666	0.244	-0.0493	0.172
	Lobe 3	0.244	0.244	-0.666	-0.0493	0.172
	Lobe 4	-1.46	-1.46	-1.46	-0.126	-0.332
	s*	-0.00046	-0.00046	-0.00046	0.00022	-0.737

The values (in atomic unit) in the table are for various combinations of sp^3 lobes/s* orbital of a Cd atom and the matrices of the Cd and its neighbor Se's in the three Cartesian coordinates.

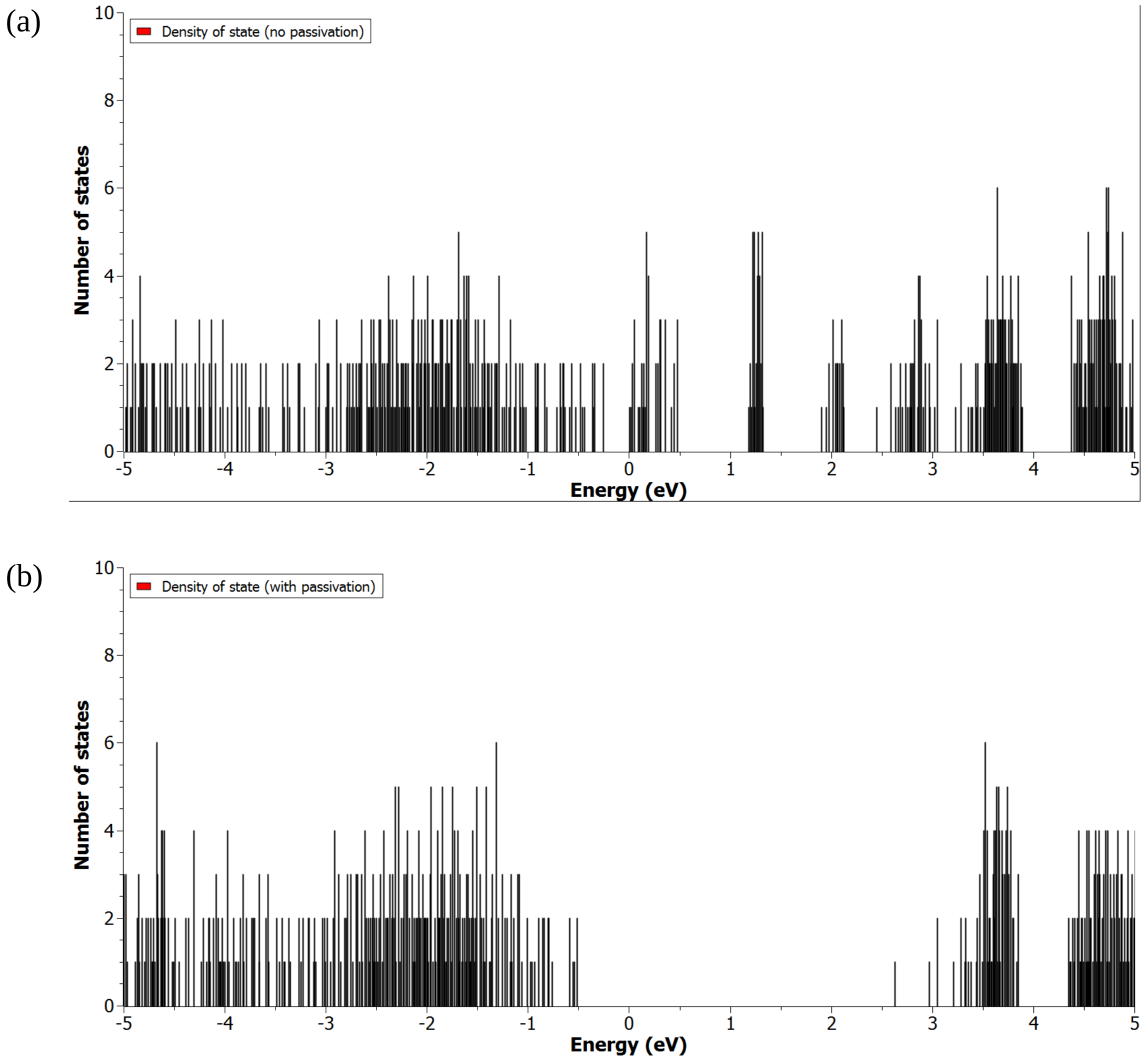

Fig. 3.4 Density of states (DOS) of a CdSe QD (radius ~ 1.17 nm) and the comparison with other calculated results.

(a) The original calculated DOS without a passivation layer of artificial atoms.

(b) The original calculated DOS with a passivation layer of artificial atoms. The height of each bar in the (a) and (b) represents the number of states within the energy window of 0.05 eV.

(*contd.*)

(c)

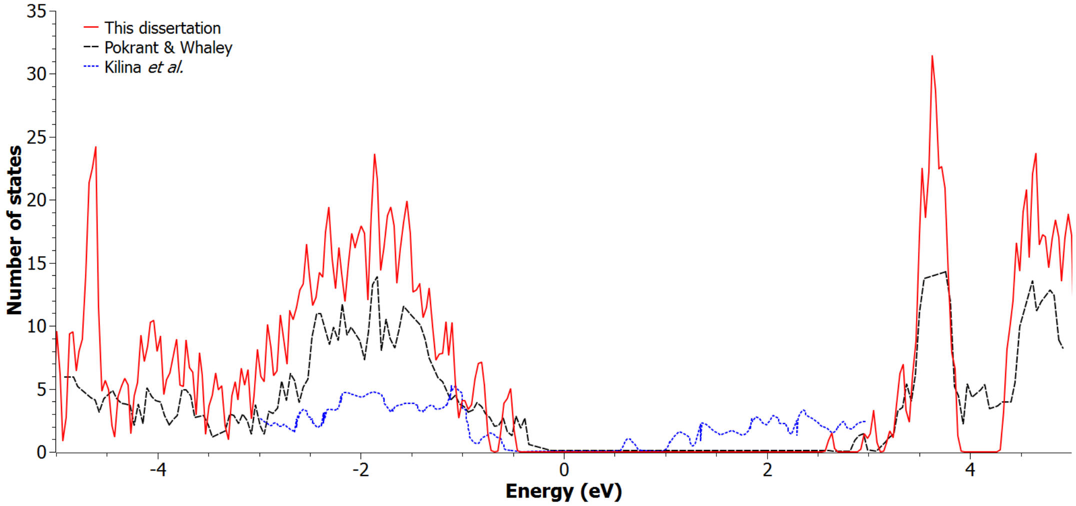

Fig. 3.4 (*contd.*) (c) the convolution of the bars in (b) with Gaussian functions (FWHM = 0.05 eV) and its comparison with Porkant and Whaley's result[30] and Kilina *et al.*'s result[37].

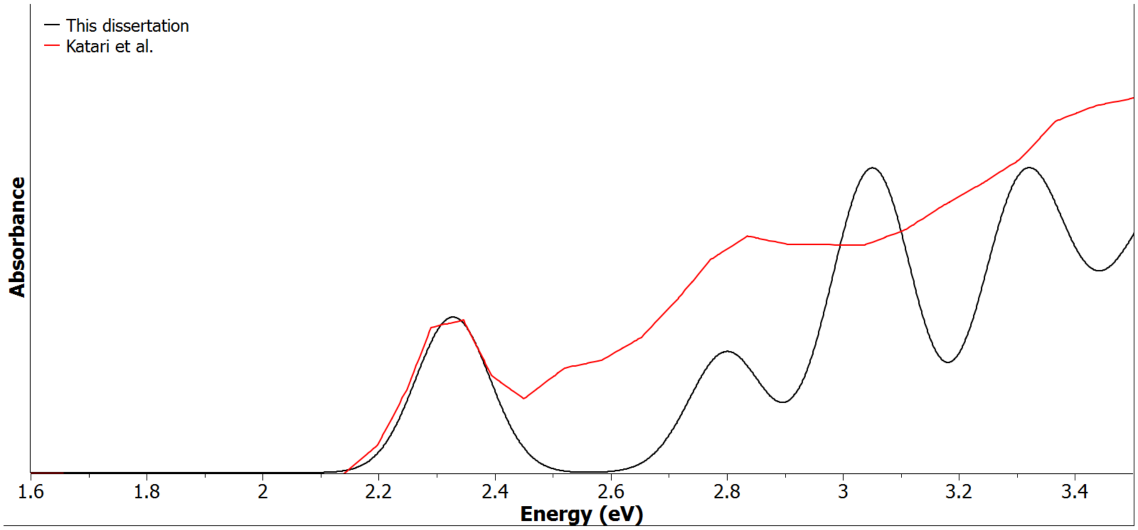

Fig. 3.5 The comparison between the calculated absorption spectrum of a CdSe QD and the measured spectrum by Katari *et al.*[15].

Chapter 4

Studies of the Size-dependent Auger Processes in Semiconductor Quantum Dots

Background

As discussed in Chapter 1, the Auger processes play various kind of roles in QDs, such as conversion of light to dark states and vice versa[1], or quenching the fluorescence of an exciton when the third quasi-particle is excited to high energy state to conserve the energy[1-2]. Recent experimental findings[2-3-4] discovered that the size-dependence of the Auger lifetime obeys a power law, namely $\tau_A \propto r^p$, of over a large radius span, from 1 nm to 5 nm, across semiconductors. The summary of experimental results on different kinds of charge states can be found in Table 1.1. The previous[5,6] and recent[7] theoretical works that have studied the size dependence of the Auger process inspired author's interest in studying the size-dependent trend using tight-binding (TB) method described in Chap 2. In this chapter, the calculation of the rate of a few kinds of the Auger process in various size of CdSe QDs were performed: (1) negative trion (two electrons and one hole), (2) positive trion (one electron and two holes), and (3) biexciton (two electrons and two holes). The author also compared these results with the existing literature, including both experimental[2,3] and theoretical[5, 7] studies, whose focus was on CdSe QDs.

Methodology for Calculations

I. Theoretical Expression of the Auger Processes for a Trion

As mentioned in Chapter 1, the source of the Auger process is governed by the Coulombic interaction[8]. Therefore, for the case of a negative trion (two electrons and one hole) in a quantum dot (QD), the wave functions of the initial and final states are expressed below[9]:

(1) the initial singlet state is

$$\Phi_i(r_1,r_2)=\frac{1}{\sqrt{2}}\Psi_{Se}(r_1)\Psi_{Se}(r_2)(\alpha(r_1)\beta(r_2)-\alpha(r_2)\beta(r_1)) \tag{1}$$

and (2) the final singlet state is

$$\Phi_f(\boldsymbol{r}_1,\boldsymbol{r}_2)=\frac{1}{2}(\Psi_{VB}(\boldsymbol{r}_1)\Psi_{e_f}(\boldsymbol{r}_2)+\Psi_{VB}(\boldsymbol{r}_2)\Psi_{e_f}(\boldsymbol{r}_1))(\alpha(\boldsymbol{r}_1)\beta(\boldsymbol{r}_2)-\alpha(\boldsymbol{r}_2)\beta(\boldsymbol{r}_1)) \quad , \tag{2}$$

where $\Psi_{Se}(\boldsymbol{r})=\sum_{\alpha} c_{\alpha}^{Se}\phi_{\alpha}^{Se}(\boldsymbol{r})$ is the electronic state at the conduction band (CB) edge,

$\Psi_{VB}(\boldsymbol{r})=\sum_{\gamma} c_{\gamma}^{VB}\phi_{\gamma}^{VB}(\boldsymbol{r})$ is the state in the valence band (VB), and

$\Psi_{e_f}(\boldsymbol{r})=\sum_{\delta} c_{\delta}^{e_f}\phi_{\delta}^{e_f}(\boldsymbol{r})$ is the final state in the CB to which the second electron is excited after the electron-hole recombination. The spin state of the two states in Eq. (1) and (2) are assumed to remain singlet. The matrix element of the Auger transition for a negative trion is therefore written as,

$$\begin{aligned} M_{if} &= \left\langle \Phi_i(\boldsymbol{r}_1,\boldsymbol{r}_2) \middle| \frac{1}{\epsilon|\boldsymbol{r}_{12}|} \middle| \Phi_f(\boldsymbol{r}_1,\boldsymbol{r}_2) \right\rangle \\ &= \frac{1}{\sqrt{2}}\left(\left\langle \Psi_{Se}(\boldsymbol{r}_1)\Psi_{Se}(\boldsymbol{r}_2) \middle| \frac{1}{\epsilon|\boldsymbol{r}_{12}|} \middle| \Psi_{VB}(\boldsymbol{r}_1)\Psi_{e_f}(\boldsymbol{r}_2) \right\rangle \right. \quad , \\ &\quad \left. + \left\langle \Psi_{Se}(\boldsymbol{r}_1)\Psi_{Se}(\boldsymbol{r}_2) \middle| \frac{1}{\epsilon|\boldsymbol{r}_{12}|} \middle| \Psi_{e_f}(\boldsymbol{r}_1)\Psi_{VB}(\boldsymbol{r}_2) \right\rangle \right) \end{aligned} \tag{3}$$

where ε is the dielectric constant. The Coulombic operator in Eq.(3) can be expressed in terms of the coordinates of the nuclei, **R**, and the local orbital coordinate, $\mathbf{r}_\alpha$, where α is the label of atomic orbital *s*, *p* and s^*. That is, for a pair of atom *A* and *B*,. Using multipole expansion for Cartesian coordinate on the operator, the leading term is

$$\frac{1}{|\boldsymbol{r}_{12}|} \approx \frac{1}{|\boldsymbol{R}_A(1)-\boldsymbol{R}_B(2)|} \quad , \tag{4}$$

where the assumption $|\boldsymbol{R}_A(1)-\boldsymbol{R}_B(2)| \gg |\boldsymbol{r}_{A\alpha}(1)-\boldsymbol{r}_{B\beta}(2)|$ is valid when one introduces Eq. (4) into Eq. (3) for the inter-atomic interactions. When the restriction of A < B restriction is applied to Eq.(4) to account for the indistinguishability of identical particles. Eq.(3) then becomes

$$\begin{aligned} M_{if} \approx \frac{1}{\sqrt{2}} \sum_{A=B} \{ & \\ & \sum_{\alpha,\beta,\gamma,\delta} c_\alpha^{Se} c_\beta^{Se} c_\gamma^{VB} c_\delta^{e_f} \left\langle \phi_A^{Se}(\boldsymbol{r}_\alpha(1))\,\phi_B^{Se}(\boldsymbol{r}_\beta(2)) \right| \frac{1}{\epsilon|\boldsymbol{r}(1)-\boldsymbol{r}(2)|} \left| \phi_{A'}^{VB}(\boldsymbol{r}_\gamma(1))\,\phi_{B'}^{e_f}(\boldsymbol{r}_\delta(2)) \right\rangle \\ & + \sum_{\alpha,\beta,\gamma,\delta} c_\alpha^{Se} c_\beta^{Se} c_\gamma^{VB} c_\delta^{e_f} \left\langle \phi_A^{Se}(\boldsymbol{r}_\alpha(2))\,\phi_B^{Se}(\boldsymbol{r}_\beta(1)) \right| \frac{1}{\epsilon|\boldsymbol{r}(1)-\boldsymbol{r}(2)|} \left| \phi_{A'}^{VB}(\boldsymbol{r}_\gamma(2))\,\phi_{B'}^{e_f}(\boldsymbol{r}_\delta(1)) \right\rangle \} \\ & + \frac{1}{\sqrt{2}} \sum_{A<B} \{ \sum_{\alpha,\beta,\gamma,\delta} c_\alpha^{Se} c_\beta^{Se} c_\gamma^{VB} c_\delta^{e_f} \frac{\left\langle \phi_A^{Se}(\boldsymbol{r}_\alpha(1)) \middle| \phi_{A'}^{VB}(\boldsymbol{r}_\gamma(1)) \right\rangle \left\langle \phi_B^{Se}(\boldsymbol{r}_\beta(2)) \middle| \phi_{B'}^{e_f}(\boldsymbol{r}_\delta(2)) \right\rangle}{\epsilon|\boldsymbol{R}_A(1)-\boldsymbol{R}_B(2)|} \\ & + \sum_{\alpha,\beta,\gamma,\delta} c_\alpha^{Se} c_\beta^{Se} c_\gamma^{VB} c_\delta^{e_f} \frac{\left\langle \phi_A^{Se}(\boldsymbol{r}_\alpha(2)) \middle| \phi_{A'}^{VB}(\boldsymbol{r}_\gamma(2)) \right\rangle \left\langle \phi_B^{Se}(\boldsymbol{r}_\beta(1)) \middle| \phi_{B'}^{e_f}(\boldsymbol{r}_\delta(1)) \right\rangle}{\epsilon|\boldsymbol{R}_A(1)-\boldsymbol{R}_B(2)|} \}. \end{aligned} \tag{5}$$

An expression of the Auger rate similar to the above equation is given in Schulz *et al.*'s study[10]. The first summation on the RHS of the approximate sign in Eq. (5) is the Coulombic interaction between atomic orbitals on the same atom (A = B), and the evaluation of the two-electron integrals uses the numerical values calculated by Lee *et al.*[11], where the two-electron integrals for the summation of A = B were unscreened, so ε was chosen as unity[12]. On the other hand, the overlap integrals between atomic orbital in the second summation in Eq. (5), i.e. the terms with the form $\left\langle \phi_A(\boldsymbol{r}_\alpha(1)) \middle| \phi_{A'}(\boldsymbol{r}_\gamma(1)) \right\rangle$ (or $\left\langle \phi_B(\boldsymbol{r}_\beta(1)) \middle| \phi_{B'}(\boldsymbol{r}_\delta(1)) \right\rangle$), have the following properties:

$$\left\langle \phi_A(\boldsymbol{r}_\alpha) \middle| \phi_{A'}(\boldsymbol{r}_\gamma) \right\rangle \left\langle \phi_B(\boldsymbol{r}_\beta) \middle| \phi_{B'}(\boldsymbol{r}_\delta) \right\rangle = \begin{cases} \delta_{\alpha,\gamma}\delta_{\beta,\delta} & \text{if A = A' and B = B'} \\ \delta_{\alpha,\gamma}\left\langle \phi_B(\boldsymbol{r}_\beta) \middle| \phi_{B'}(\boldsymbol{r}_\delta) \right\rangle & \text{if A = A' but B' is B's nearest neighbor} \\ \delta_{\beta,\delta}\left\langle \phi_A(\boldsymbol{r}_\alpha) \middle| \phi_{A'}(\boldsymbol{r}_\gamma) \right\rangle & \text{if B = B' but A' is A's nearest neighbor} \\ 0 & \text{Otherwise,} \end{cases} \tag{6}$$

where the values of the overlap integral can be found in Table 4.1, where $\phi_i(\boldsymbol{r})$ are represented in terms of *sp*^{3} lobes, composed of *s* and 3 *p* orbits, and *s**. The dielectric constant of bulk CdSe, 6.25[7], was chosen for ε in the summations of A < B in this dissertation as an approximation. The overlap integrals were calculated by the author using the composite Simpson's rule.

For the expression for the Auger process within a positive trion, one can simply replace the initial singlet states in Eq. (1) by[9]

$$\Phi_f(\boldsymbol{r}_1,\boldsymbol{r}_2)=\frac{1}{2}(\Psi_{S_e}(\boldsymbol{r}_1)\Psi_{h_i}(\boldsymbol{r}_2)+\Psi_{S_e}(\boldsymbol{r}_2)\Psi_{h_i}(\boldsymbol{r}_1))(\alpha(\boldsymbol{r}_1)\beta(\boldsymbol{r}_2)-\alpha(\boldsymbol{r}_2)\beta(\boldsymbol{r}_1)) \quad , \tag{7}$$

where $\Psi_{S_e}(\boldsymbol{r})$ is the electronic state at the CB edge, as defined in Eq. (1), and

$\Psi_{h_i}(\boldsymbol{r})=\sum_\gamma c_\gamma^{h_i}\phi_\gamma^{h_i}(\boldsymbol{r})$ is a state deep in the VB, while the final singlet state is replaced by

$$\Phi_i(\boldsymbol{r}_1,\boldsymbol{r}_2)=\frac{1}{2}(\Psi_{VB_1}(\boldsymbol{r}_1)\Psi_{VB_2}(\boldsymbol{r}_2)+\Psi_{VB_1}(\boldsymbol{r}_2)\Psi_{VB_2}(\boldsymbol{r}_1))(\alpha(\boldsymbol{r}_1)\beta(\boldsymbol{r}_2)-\alpha(\boldsymbol{r}_2)\beta(\boldsymbol{r}_1)) \quad , \tag{8}$$

where $\Psi_{VB_1}(\boldsymbol{r})$ and $\Psi_{VB_2}(\boldsymbol{r})$ are the two electronic states in the VB and they both have the form of $\Psi_{VB_i}(\boldsymbol{r})=\sum_\alpha c_\alpha^{VB_i}\phi_\alpha^{VB_i}(\boldsymbol{r})$, {*i* = 1 or 2}. The choices of VB$_1$ and VB$_2$ are determined by the Fermi-Dirac distribution mentioned in the section II.

Using the matrix element defined in Eq. (5), the Auger process of a pair of initial and final states, Φ_i and Φ_j , has the form of Fermi's Golden rule[6],

$$k_A = \frac{2\pi}{\hbar} |M_{if}|^2 \rho_f \quad , \tag{9}$$

where ρ_f is the density of states (DOS) for the final state. Due to the sparse and discrete nature of the state distribution in semiconductor QDs, as the examples shown in Fig. 4.1, the electronic transitions, such as the Auger transition of interest, need phonons to achieve an energetic resonance. Although the literature[13,14] has suggested that the more dense states near the edge of VB mitigates the phonon bottleneck, the treatment of phonon density is not included in this dissertation because the phonon contribution is a second-order contribution[7]. Instead, an approximation was made to account for the resonance issue: a fixed energetic window around resonant final state, ΔE_f, is chosen, and all the states within the window have equal contribution to the square of the matrix element of the Auger transition. As an approximation, ρ_f is defined as $1/|2\Delta E_f|$, which means including all of the states within $2\Delta E_f$. In this chapter, ΔE_f was chosen as ±kT.

II. Statistical Means for the Summation of Rates

For both negative and positive trion, there is at least one hole in the VB, and due to the more dense states around the edge of VB, the location of the hole(s) should follow a distribution in each case. For a negative trion, the Boltzmann distribution,

$p_h(E_{i,m}) = e^{-\beta E_{i,m}} / \sum_{i=1}^{N} \sum_{m=1}^{M} e^{-\beta E_{i,m}}$, is applied to calculate the probability of finding a hole at the state $VB_{i,m}$, where $E_{i,m}$ is the energy of the $VB_{i,m}$ state and M represents the number of degeneracy of $VB_{i,m}$, because there is only a single hole in VB. For the cases involving a positive trion, there are two holes in VB, so the Fermi-Dirac (F-D) distribution for a hole, $f_h(E_i)=1-f_e(E_i)=1/(1+e^{\beta(\mu_h-E_i)})$, is used to account for the average number of holes in state VB_i, where μ_h is the chemical potential for the two holes. The probability of finding the two holes in a given state(s) is defined as

$$p_h(E_{i,m},E_{j,n})=\frac{f_h(E_{i,m})f_h(E_{j,n})}{\sum_{i,j}^{L}\sum_{m,n}^{M,N}f_h(E_{i,m})f_h(E_{j,n})} \quad , \tag{10}$$

where $E_{i,m}$ ($E_{j,n}$) is the energy of the $VB_{i,m}$ ($VB_{j,n}$) state and M (N) represents the number of degeneracy of $VB_{i,m}$ ($VB_{j,n}$). In this dissertation, the states VB_1 to VB_L were all the states within an energy range of 5kT from the edge of VB, and value of 0.026 eV was used for 1/β (or kT).

For the electron(s), the probability to find the two electrons in a negative trion has the same form of Eq. (10), except f_h is replaced by the F-D distribution for electrons, $f_e(E_{i,,})=1/(1+e^{\beta(E_{i,m}-\mu_e)})$, where m represents the m-th degenerate state with the energy E_i, while for the electron in a positive trion, it is assumed to locate at the edge of CB. The probability of finding an electron at the CB edge is essentially unity because the energy difference between the two states with the lowest energy is large (about 300 meV)[15,16] compared with thermal energy.

The chemical potential of the two holes in a positive trion is calculated using the equation below:

$$2=\sum_{i,j}\sum_{m,n}^{M,N}(1-f_h(E_{i,m}))(1-f_h(E_{j,n}))-\sum_{(i=j)\vee(i<j)}\sum_{m,n}^{M,N}(1-f_h(E_{i,m}))(1-f_h(E_{j,m})) \quad , \tag{11}$$

where 2 on the LHS means that the summation of the RHS equals to two quasi-particles, and the subtraction of the second summation on the RHS eliminates double counting and accounts for the Pauli exclusion principle. Similarly, the chemical potential of the two electrons in a negative trion is calculated using the equation,

$$2=\sum_{i,j}\sum_{m,n}^{M,N} f_e(E_{i,m}) f_e(E_{j,n}) - \sum_{(i=j)\vee(i<j)}\sum_{m,n}^{M,N} f_e(E_{i,m}) f_e(E_{j,n}) \quad , \tag{12}$$

where $E_{i,m}$ ($E_{j,n}$) is the energy of the CB state $CB_{i,m}$ ($CB_{j,n}$) state and M (N) represents the number of degeneracy of $CB_{i,m}$ ($CB_{j,n}$). The calculated chemical potential of (1) electrons in a negative trion and (2) holes in a positive trion for various sizes of CdSe QD are provided in Table 4.2

Applying the statistics described in this section to Eq. (9) converts it to

$$k_A^{tot}=\sum_l k_{A,l}=\sum_l \left(\sum_f p_{h,l}\frac{2\pi}{\hbar}|M_{lf}|^2 (\Delta E_f)^{-1}\right) \quad , \tag{13}$$

where $p_{h,l}$ stands for either the $P_h(E_{l,m})$ or $P_h(E_{l,m}, E_{j,n})$ mentioned above.

III. Debye Shielding

When considering trions, there is always some shielding of the two of them by the third. For example, in the case of a negative trion, the hole shields the interaction of the two electrons. Shielding is often invoked in bulk semiconductor when the concentration of the charge carrier, often photo-induced, is high. (ref) One way to model the shielding is to introduce the Debye shielding,

$$\Phi(\boldsymbol{r})=\frac{e^2}{4\pi\epsilon\boldsymbol{r}}e^{-\boldsymbol{r}/\lambda_D} \quad , \tag{14}$$

where e is the electronic charge, ε is the dielectric constant, and the Debye length, λ_D, is defined as $\sqrt{\epsilon k_B T/\sum_i n_i e^2}$, where k_B is the Boltzmann constant, n_i is the concentration of charge. In this dissertation, the Coulombic operator in the Auger matrix element in Eq. (5) is replaced by Eq. (12). However, because of the small number of carriers and hence the length approximation of Eq. (14), the Debye length is not calculated using the definition above, but instead, a series of calculations of the Auger process is made with different values of λ_D are performed to study the effect of various on the rate.

IV. Expression of the Auger Rate for a Biexciton

The wave function of a biexciton in a QD with 2N electrons can be written in a Slater determinant[17],

$$\psi_{BX}(\boldsymbol{r}_1,\ldots,\boldsymbol{r}_{2N})=\left|\phi_1(\boldsymbol{r}_1)\bar{\phi}_1(\boldsymbol{r}_2)\cdots\phi_{VB-1}(\boldsymbol{r}_{2N-3})\bar{\phi}_{VB-1}(\boldsymbol{r}_{2N-2})\phi_{CB}(\boldsymbol{r}_{2N-1})\bar{\phi}_{CB}(\boldsymbol{r}_{2N})\right\rangle \quad (15)$$

where ϕ_1 is the eigenstate with the lowest energy among all electronic states, ϕ_{VB-1} is the second to the last VB state to the VB edge, ϕ_{CB} is the state at the CB edge, and the states with an overhead bar, e.g. $\bar{\phi}_1$, are the states of opposite spin to states without a bar. In Eq. (15), the state at the VB edge (ϕ_{VB} , not present in Eq. (15)) has no electron because they are excited to ϕ_{CB} . Similarly, a negative trion is

$$\psi_{T^-,1}(\boldsymbol{r}_1,\ldots,\boldsymbol{r}_{2N})=\left|\phi_1(\boldsymbol{r}_1)\bar{\phi}_1(\boldsymbol{r}_2)\cdots\phi_{VB-1}(\boldsymbol{r}_{2N-3})\bar{\phi}_{VB-1}(\boldsymbol{r}_{2N-2})\phi_{VB}(\boldsymbol{r}_{2N-1})\bar{\phi}_{f,T^-}(\boldsymbol{r}_{2N})\right\rangle \quad (16)$$

or

$$\psi_{T^-,2}(\boldsymbol{r}_1,\ldots,\boldsymbol{r}_{2N})=\left|\phi_1(\boldsymbol{r}_1)\bar{\phi}_1(\boldsymbol{r}_2)\cdots\phi_{VB-1}(\boldsymbol{r}_{2N-3})\bar{\phi}_{VB-1}(\boldsymbol{r}_{2N-2})\bar{\phi}_{VB}(\boldsymbol{r}_{2N-1})\phi_{f,T^-}(\boldsymbol{r}_{2N})\right\rangle. \quad (17)$$

And for the case of positive trion, the final state is

$$\psi_{T^+,1}(\boldsymbol{r}_1,\ldots,\boldsymbol{r}_{2N})=\left|\phi_1(\boldsymbol{r}_1)\bar{\phi}_1(\boldsymbol{r}_2)\cdots\phi_{f,T^+}(\boldsymbol{r}_k)\cdots\phi_{VB}(\boldsymbol{r}_{2N-2})\bar{\phi}_{VB}(\boldsymbol{r}_{2N-1})\bar{\phi}_{CB}(\boldsymbol{r}_{2N})\right\rangle \quad (18)$$

or

$$\psi_{T^+,2}(\boldsymbol{r}_1,\ldots,\boldsymbol{r}_{2N})=\left|\phi_1(\boldsymbol{r}_1)\bar{\phi}_1(\boldsymbol{r}_2)\cdots\bar{\phi}_{f,T^+}(\boldsymbol{r}_k)\cdots\phi_{VB}(\boldsymbol{r}_{2N-2})\bar{\phi}_{VB}(\boldsymbol{r}_{2N-1})\phi_{CB}(\boldsymbol{r}_{2N})\right\rangle. \quad (19)$$

Assuming the cases in Eq. (16) to (19) have equal probability, and the electrons and holes in the biexcton are uncorrelated, by introducing Eqs. (16) to (19) into Eqs. (3) and (9), the expression of the Auger rate of a biexciton, k_A^{BX} , is

$$\begin{aligned}
k_A^{BX} &= \frac{2\pi}{\hbar}\left|M_{if,A}^{BX}\right|^2 \rho_{f,BX} \\
&\sim \frac{2\pi}{\hbar}\Bigg(\left|\langle\psi_{BX}|\frac{1}{\boldsymbol{r}_{12}}|\psi_{T^-,1}\rangle\right|^2 \rho_{f,T^-} + \left|\langle\psi_{BX}|\frac{1}{\boldsymbol{r}_{12}}|\psi_{T^-,2}\rangle\right|^2 \rho_{f,T^-} \\
&\quad + \left|\langle\psi_{BX}|\frac{1}{\boldsymbol{r}_{12}}|\psi_{T^+,1}\rangle\right|^2 \rho_{f,T^+} + \left|\langle\psi_{BX}|\frac{1}{\boldsymbol{r}_{12}}|\psi_{T^+,2}\rangle\right|^2 \rho_{f,T^+}\Bigg) \\
&= \frac{2\pi}{\hbar}\left|\langle\phi_{CB}(\boldsymbol{r}_1)\bar{\phi}_{CB}(\boldsymbol{r}_2)|\frac{1}{\boldsymbol{r}_{12}}|\phi_{f,T^-}(\boldsymbol{r}_1)\bar{\phi}_{VB}(\boldsymbol{r}_2)\rangle\right|^2 \rho_{f,T^-} \\
&\quad + \frac{2\pi}{\hbar}\left|\langle\phi_{CB}(\boldsymbol{r}_1)\bar{\phi}_{CB}(\boldsymbol{r}_2)|\frac{1}{\boldsymbol{r}_{12}}|\bar{\phi}_{f,T^-}(\boldsymbol{r}_1)\phi_{VB}(\boldsymbol{r}_2)\rangle\right|^2 \rho_{f,T^-} \\
&\quad + \frac{2\pi}{\hbar}\left|\langle\phi_{CB}(\boldsymbol{r}_1)\bar{\phi}_{CB}(\boldsymbol{r}_2)|\frac{1}{\boldsymbol{r}_{12}}|\phi_{f,T^+}(\boldsymbol{r}_1)\bar{\phi}_{VB}(\boldsymbol{r}_2)\rangle\right|^2 \rho_{f,T^+} \\
&\quad + \frac{2\pi}{\hbar}\left|\langle\phi_{CB}(\boldsymbol{r}_1)\bar{\phi}_{CB}(\boldsymbol{r}_2)|\frac{1}{\boldsymbol{r}_{12}}|\bar{\phi}_{f,T^+}(\boldsymbol{r}_1)\phi_{VB}(\boldsymbol{r}_2)\rangle\right|^2 \rho_{f,T^+} \\
&= k_A^{T^-} + k_A^{T^-} + k_A^{T^+} + k_A^{T^+} = 2k_A^{T^-} + 2k_A^{T^+},
\end{aligned} \tag{20}$$

where $k_A^{T^+}$ / $k_A^{T^-}$ is the rate constant of the Auger process of positive/negative trion, respectively, ϕ_{f,T^+} , ϕ_{f,T^-} , ϕ_{CB} , and ϕ_{VB} are defined earlier, and $\rho_{f,BX}$ is the density of final states of biexciton, while ρ_{f,T^+} / ρ_{f,T^-} is the density of final states of the positive/negative trion, respectively. This relationship in Eq. (19) has been used in literature[18,19,20] as an approximate relationship between the Auger rate of a biexciton and those of negative and positive trions. Although the assumption of equal probability of the four channels is made in the relationship in Eq. (20), $k_A^{BX} \approx 2k_A^{T^+} + 2k_A^{T^-}$, it has been found in experiments[21] that even if the Auger rate of a positive trion is much faster (about 10 times)[21] than that of a negative trion, Eq. (20) still provides a reasonable estimate of the Auger lifetime of a biexiton.

Results and Discussion

The calculated results of the size dependence of the Auger lifetime of a negative trion and a positive trion are shown in Fig. 4.2. The comparison between the results of this thesis and the existing literature are provided in Table 4.3. The data points were calculated using Eq. (13) and the details discussed in the section on the theoretical expression for the Auger processes for a trion. It can be seen in the figure that the behavior between negative trions and positive trions is different, especially in the case of large Debye shielding length (λ_D), 100 times of lattice constant (i.e. 100*a* in the figure), or effectively no shielding between quasi-particles. For the negative trion, the size dependence of the Auger lifetime follows the trend of $\tau_A^{T^-} \propto r^p$, and the power p ranges from 7.21 to 8.48. This power is comparable to the power of the TB calculation (p = 8.25, deduced from the data reported by Delerue *et al.*[6]) of Delerue *et al.*[6] on the Auger process of a negative trion in Si nanocrystal. However, unlike the relatively constant slopes for the negative trions, for the positive trion, the slopes of the three cases of smaller λ_D is different from that of λ_D=100*a*: for the later one, a turning point of the slope shows at the radius of 2.03 nm. The turning point is caused by the treatment on the matrix element of the Auger process in Eq. (5), where each atomic matrix element is categorized into (1) the interaction on the same atom, and (2) the inter-atomic interactions. The number of terms in (1) is proportional to the volume (or (size of a QD)^3), while the number of terms in (2) is roughly proportional to the volume square (or (size of a QD)^6). Therefore, the terms in (1) have a more significant contribution to the lifetime in the region of smaller sizes of QD, while the terms in (2) is more important in the region of larger sizes. The slope of the linear fit in the log-log plot (namely, p in $\tau_A^{T^+} \propto r^p$) of

λ_D=100*a* (magenta triangles) in Fig.4.2(b) is 18.7, while the second part is 6.43, where the second slope is comparable to that in Delerue *et al.*'s work[6] on the Auger lifetime of positive trion (4.95, deduced from the values reported by Delerue *et al.*[6]). This comparability between the slopes in the larger sizes suggests that the shielding plays a minimal role in the Auger process of positive trion, while the case of strongest shielding (λ_D=0.5*a*) in a negative trion gives the closest slope (p = 7.21) to the experiment findings (p = 4.3)[2]. This observation is consistent with the well accepted idea that the wave functions of the holes are more localized than those of electrons, and applying shielding on positive trions restricts the Coulombic interaction between holes.

The comparison between the calculated values of negative and positive trions and the findings in Cohn *et al.*'s experimental work[2] and the single-molecule results in Vaxenburg *et al.*'s theoretical study[7] is provided in Fig. 4.3 and Fig. 4.4. In Fig. 4.3(a), it can be seen that the absolute values of the calculated Auger lifetime by the author is around one-order-of-magnitude larger than Cohn *et al.*'s values[2] (dashed blue line), or within this ratio when the Debye shielding length (λ_D) is chosen as 100*a* (olive diamonds), while the λ_D is made smaller, such as λ_D = 0.5*a* (red squares), the absolute values of the Auger lifetime become smaller also. Although the calculated values of the Auger rate (at λ_D = 100*a*) is comparable to the measured ones, the size dependence of the former one is much larger than the later, and even larger than the calculated slope of the single-molecule calculation in Vaxenburg *et al.*'s study[7] (namely, 6.5).

There should be a similarity in the results between the TB method and the effective-mass-approximation (EMA) method, but as shown in Fig. 4.3, the size dependence between the author's calculated results (red squares and olive diamonds) and the EMA result of the single-molecule calculation by Vaxenburg *et al.*[7] (black dashed line) are different. Although Vaxenburg and coworkers[7] also applied the multipole expansion on the Coulombic interaction, $1/|\mathbf{r}_{12}|$, they expanded the operator in spherical coordinates and up to 36 terms, while in this disseration only the leading term of the expansion in Cartesian coordinates was considered, so the number of terms of expansion could be one of the sources of the discrepancy in the slope and the absolute values of lifetime between the two theoretical results. There are two other distinct differences between the method used in this dissertation and Vaxenburg *et al.*'s work[7]: (1) the nature of the wave functions at the boundary/interface between the interior of a QD and the exterior environment and (2) the region of the occurrence of the Auger processes. Regards the first difference, Vaxenburg *et al.* applied various boundary conditions and parameters to allow the electron wave functions within the QD to extend across the boundary and to conserve the probability current density at the boundary[7]. However, for the eigenstates calculated by the present TB method, the wave functions terminate at the boundary/interface of a QD, and moreover, the exclusion of the contribution of the layer of the artificial atoms from the Auger matrix element further creates an abrupt disappearance of the wave function at the boundary. For the discrepancy (2), Vaxenburg *et al.* suggested that the Auger processes have a higher chance of occurring at the boundary of QDs[7], and Efros[22] also suggested that only the surface part of the core boundary of QD has significant contribution to the matrix element of an Auger ionization process. However, for the calculation of the Auger matrix elements in this dissertation, the full spatial distribution of the wave function was included, which could introduce some ineffective contribution to the matrix elements. To alleviate the two discrepancies, an *ad hoc* approach was applied to the calculated result: a set of effective radii of the QDs were obtained by reducing the actual radii by one monolayer in the log-log plot, so the wave functions within the QD would not terminate abruptly at the boundary. It can be seen in Fig. 4.3(b) that this change made the slopes of the TB results, both $\lambda_D = 0.5a$ and $\lambda_D = 100a$, is comparable to Vaxenburg *et al.*'s result[7].

The same change in radius was also applied to the Auger lifetime of positive trion, and the comparison between the new results and the projected result of Cohn *et al.*'s study[2] is shown in Fig. 4.4(b). Although it can be seen that the new calculated slope and the absolute values still deviate from the projected curve, similar to the case in Fig. 4.4(a), the slope on the larger-size side of $\lambda_D = 100a$ curve is more comparable to the size dependence of the positive trion Delerue *et al.*'s study[6] mentioned above, i.e. 4.95. The biexciton lifetimes of various sizes of CdSe QDs was also calculated using Eq. (20) and were shown in Fig. 4.5(a) and (b) for both cases of $\lambda_D = 0.5a$ and $\lambda_D = 100a$. The size dependence of the two cases was compared with Robel *et al.*'s experimental work[3] (the slope of the dashed blue lines in Fig. 4.5 was deduced from the data reported by Robel *et al.*). The size dependence of $\lambda_D = 100a$ is closer to the results in the experimental findings (the slope p ranging from 2.5 to 3.1)[2,19,23] than that of $\lambda_D = 0.5a$, but there is still a large discrepancy from the measured result due to the propagation from the size dependence of positive trion and of negative trion.

Even though the characteristics of the dynamics of positive trion have not been well understood[21], the ratios of the Auger lifetimes ($\lambda_D = 100a$) of a positive trion to that of a negative trion for different sizes of CdSe QDs are summarized in Table 4.4 for further discussion. Due to the different size dependence between positive trion and negative trion, the ratio is not a constant, and the ratio changes from less than unity to large than one. The Auger lifetime of positive trion is expected to be smaller than that of negative trion because the DOS of the hole is higher due to the heavier effective mass. However, as shown in Fig. 4.6, the DOS of around the final state of an Auger process of a positive trion is smaller than that of a negative trion in the size region of the data points in Table 4.4. Moreover, the Auger lifetime of a positive trion in other theoretical studies[6, 20] is not necessarily shorter than that of a negative trion. The information noted above indicates that further study is needed to better understand the dynamics of positive trion. Even with the puzzles, a simple comparison between the calculated ratio of the Auger lifetime of the positive trion to that of the negative trion is shown here: for the CdSe QD with the radius = 1.76 nm, the ratio of $\tau_A^{T^+}$ / $\tau_A^{T^-}$ is 0.68, which is larger than the measured ratio of CdSe/CdS QD (the core radius = 1.5 nm), 0.15, in Park *et al.*'s study[21]. Although the calculated ratio is larger, the calculated $\tau_A^{T^+}$ (68.5 ps vs. 1.5 ns) and $\tau_A^{T^-}$ (100 ps vs. 10 ns) are both shorter than the measured values, respectively.

Summary

The size dependence of the Auger lifetime of negative trions, positive trions, and biexcitons were studied using TB method in this chapter. Although the absolute values and the size dependence of these lifetimes didn't reproduce the experimental value, the modification of the radii of QDs pointed out a potential path to improve the calculation method, but a method that allows the wave functions to be finite outside the core, such as adding a layer of shell instead of terminating abruptly at the core boundary, would be the next step to explore.

Reference

1. Marcus, R. A., Interaction of theory and experiment: examples from single molecule studies of nanoparticles. *Philos T R Soc A* **2010,** *368* (1914), 1109-1124.

2. Cohn, A. W.; Rinehart, J. D.; Schimpf, A. M.; Weaver, A. L.; Gamelin, D. R., Size Dependence of Negative Trion Auger Recombination in Photodoped CdSe Nanocrystals. *Nano Lett* **2014,** *14* (1), 353-358.

3. Robel, I.; Gresback, R.; Kortshagen, U.; Schaller, R. D.; Klimov, V. I., Universal Size-Dependent Trend in Auger Recombination in Direct-Gap and Indirect-Gap Semiconductor Nanocrystals. *Phys Rev Lett* **2009,** *102* (17), 177404.

4. Qin, W.; Liu, H.; Guyot-Sionnest, P., Small Bright Charged Colloidal Quantum Dots. *Acs Nano* **2014,** *8* (1), 283-291.

5. Chepic, D. I.; Efros, A. L.; Ekimov, A. I.; Vanov, M. G.; Kharchenko, V. A.; Kudriavtsev, I. A.; Yazeva, T. V., Auger Ionization of Semiconductor Quantum Drops in a Glass Matrix. *J Lumin* **1990,** *47* (3), 113-127.

6. Delerue, C.; Lannoo, M.; Allan, G.; Martin, E.; Mihalcescu, I.; Vial, J. C.; Romestain, R.; Muller, F.; Bsiesy, A., Auger and Coulomb Charging Effects in Semiconductor Nanocrystallites. *Phys Rev Lett* **1995,** *75* (11), 2228-2231.

7. Vaxenburg, R.; Rodina, A.; Shabaev, A.; Lifshitz, E.; Efros, A. L., Nonradiative Auger Recombination in Semiconductor Nanocrystals. *Nano Lett* **2015,** *15* (3), 2092-2098.

8. Landau, L. D.; Lifshits, E. M., *Quantum mechanics: non-relativistic theory.* 2d ed.; Pergamon Press; sole distributors in the U.S.A., Addison-Wesley Pub. Co., Reading, Mass.: Oxford, New York,, 1965; p xiii, 616 p.

9. Cragg, G. E.; Efros, A. L., Suppression of Auger Processes in Confined Structures. *Nano Lett* **2010,** *10* (1), 313-317.

10. Schulz, S.; Schumacher, S.; Czycholl, G., Tight-binding model for semiconductor quantum dots with a wurtzite crystal structure: From one-particle properties to Coulomb correlations and optical spectra. *Phys Rev B* **2006,** *73* (24), 245327.

11. Lee, S.; Jönsson, L.; Wilkins, J.; Bryant, G.; Klimeck, G., Electron-hole correlations in semiconductor quantum dots with tight-binding wave functions. *Phys Rev B* **2001,** *63* (19).

12. Leung, K.; Whaley, K. B., Electron-hole interactions in silicon nanocrystals. *Phys Rev B* **1997,** *56* (12), 7455.

13. Kambhampati, P.; Cooney, R. R.; Sewall, S. L.; Anderson, K. E. H.; Dias, E. A., Breaking the phonon bottleneck for holes in semiconductor quantum dots. *Phys Rev Lett* **2007,** *98* (17).

14. Prezhdo, O. V.; Kilina, S. V.; Kilin, D. S., Breaking the Phonon Bottleneck in PbSe and CdSe Quantum Dots: Time-Domain Density Functional Theory of Charge Carrier Relaxation. *Acs Nano* **2009,** *3* (1), 93-99.

15. Efros, A. L.; Rosen, M., The electronic structure of semiconductor nanocrystals. *Annu Rev Mater Sci* **2000,** *30*, 475-521.

16. Shim, M.; Guyot-Sionnest, P., n-type colloidal semiconductor nanocrystals. *Nature* **2000,** *407* (6807), 981.

17. Szabo, A.; Ostlund, N. S., *Modern quantum chemistry: introduction to advanced electronic structure theory*. Courier Corporation: 1989.

18. Zhao, J.; Nair, G.; Fisher, B. R.; Bawendi, M. G., Challenge to the Charging Model of Semiconductor-Nanocrystal Fluorescence Intermittency from Off-State Quantum Yields and Multiexciton Blinking. *Phys Rev Lett* **2010,** *104* (15).

19. Jha, P. P.; Guyot-Sionnest, P., Trion Decay in Colloidal Quantum Dots. *Acs Nano* **2009,** *3* (4), 1011-1015.

20. Wang, L.-W.; Califano, M.; Zunger, A.; Franceschetti, A., Pseudopotential Theory of Auger Processes in CdSe Quantum Dots. *Phys Rev Lett* **2003,** *91* (5).

21. Park, Y.-S.; Bae, W. K.; Pietryga, J. M.; Klimov, V. I., Auger Recombination of Biexcitons and Negative and Positive Trions in Individual Quantum Dots. *Acs Nano* **2014,** *8* (7), 7288-7296.

22. Efros, A., Auger Processes in Nanosize Semiconductor Crystals. *arXiv preprint cond-mat/0204437* **2002**.

23. Achermann, M.; Hollingsworth, J. A.; Klimov, V. I., Multiexcitons confined within a subexcitonic volume: Spectroscopic and dynamical signatures of neutral and charged biexcitons in ultrasmall semiconductor nanocrystals. *Phys Rev B* **2003,** *68* (24), 245302.

24. Benkert, T., Franke, K and Standish, R SciDAVis. Available at http://scidavis.sourceforge.net/. **2007**.

Table 4.1 The matrix of overlap integral of a Cd atom and a Se atom

A Cd atom as the center atom						
		Lobe 1	Lobe 2	Lobe 3	Lobe 4	s*
The two atomic orbitals on the same atom (on-site)	Lobe 1	1.0	0.0	0.0	0.0	0.00045
	Lobe 2	0.0	1.0	0.0	0.0	0.00045
	Lobe 3	0.0	0.0	1.0	0.0	0.00045
	Lobe 4	0.0	0.0	0.0	1.0	0.00045
	s*	0.00045	0.00045	0.00045	0.00045	1.0
The Nearest neighbor (Se) in Vector 1	Lobe 1	0.299	0.425	0.425	0.425	0.0163
	Lobe 2	0.148	-0.264	0.181	0.181	0.0541
	Lobe 3	0.148	0.181	-0.264	0.181	0.0541
	Lobe 4	0.148	0.181	0.181	-0.264	0.0541
	s*	-0.00001	0.00010	0.00010	0.00010	0.212
The Nearest neighbor (Se) in Vector 2	Lobe 1	-0.264	0.148	0.181	0.181	0.0541
	Lobe 2	0.425	0.299	0.425	0.425	0.0163
	Lobe 3	0.181	0.148	-0.264	0.181	0.0541
	Lobe 4	0.181	0.148	0.181	-0.264	0.0541
	s*	0.00010	-0.00001	0.00010	0.00010	0.212
The Nearest neighbor (Se) in Vector 3	Lobe 1	-0.264	0.181	0.148	0.181	0.0541
	Lobe 2	0.181	-0.264	0.148	0.181	0.0541
	Lobe 3	0.425	0.425	0.299	0.425	0.0163
	Lobe 4	0.181	0.181	0.148	-0.264	0.0541
	s*	0.00010	0.00010	-0.00001	0.00010	0.212
The Nearest neighbor (Se) in Vector 4	Lobe 1	0.330	-0.116	-0.116	0.148	0.0541
	Lobe 2	-0.116	0.330	-0.116	0.148	0.0541
	Lobe 3	-0.116	-0.116	0.330	0.148	0.0541
	Lobe 4	0.425	0.425	0.425	0.298	0.0163
	s*	0.00010	0.00010	0.00010	-0.00001	0.212

The values (in atomic unit) in the table are for various combinations of sp^3 lobes/s* orbital of a Se atom and the matrices of the Cd and its neighbor Se's in the three Cartesian coordinates.

(contd.)

Table 4.1 (*contd.*) The matrix of overlap integral of a Cd atom and a Se atom

An Se atom as the center atom						
		Lobe 1	Lobe 2	Lobe 3	Lobe 4	s*
The two atomic orbitals on the same atom (on-site)	Lobe 1	1.0	0.0	0.0	0.0	0.00551
	Lobe 2	0.0	1.0	0.0	0.0	0.00551
	Lobe 3	0.0	0.0	1.0	0.0	0.00551
	Lobe 4	0.0	0.0	0.0	1.0	0.00551
	s*	0.00551	0.00551	0.00551	0.00551	1.0
The Nearest neighbor (Cd) in Vector 1	Lobe 1	0.299	0.148	0.148	0.148	-0.00001
	Lobe 2	0.425	-0.264	0.181	0.181	0.00010
	Lobe 3	0.425	0.181	-0.264	0.181	0.00010
	Lobe 4	0.425	0.181	0.181	-0.264	0.00010
	s*	0.0163	0.0541	0.0541	0.0541	0.212
The Nearest neighbor (Cd) in Vector 2	Lobe 1	-0.264	0.425	0.181	0.181	0.00010
	Lobe 2	0.148	0.299	0.148	0.148	-0.00001
	Lobe 3	0.181	0.425	-0.264	0.181	0.00010
	Lobe 4	0.181	0.425	0.181	-0.264	0.00010
	s*	0.0541	0.0163	0.0541	0.0541	0.212
The Nearest neighbor (Cd) in Vector 3	Lobe 1	-0.264	0.181	0.425	0.181	0.00010
	Lobe 2	0.181	-0.264	0.425	0.181	0.00010
	Lobe 3	0.148	0.148	0.299	0.148	-0.00001
	Lobe 4	0.181	0.181	0.425	-0.264	0.00010
	s*	0.0541	0.0541	0.0163	0.0541	0.212
The Nearest neighbor (Cd) in Vector 4	Lobe 1	0.330	-0.116	-0.116	0.425	0.00010
	Lobe 2	-0.116	0.330	-0.116	0.425	0.00010
	Lobe 3	-0.116	-0.116	0.330	0.425	0.00010
	Lobe 4	0.148	0.148	0.148	0.298	-0.00001
	s*	0.0541	0.0541	0.0541	0.0163	0.212

The values (in atomic unit) in the table are for various combinations of sp^3 lobes/s* orbital of a Se atom and the matrices of the Se and its neighbor Cd's in the three Cartesian coordinates.

Table 4.2 The calculated chemical potentials of CdSe QDs with different sizes.

	Chemical Potential (eV)	
	Negative Trion	Positive Trion
Radius (nm)	Electron	Hole
1.76	2.623	-0.3349
1.85	2.556	-0.3074
2.03	2.484	-0.2747
2.17	2.418	-0.2503
2.41	2.370	-0.2317
3.34	2.162	-0.1550
3.81	2.103	-0.1325

The values are for the electrons in a negative trion or the holes in a positive trion.

Radius (nm)	Conduction band	Valence band
1.76	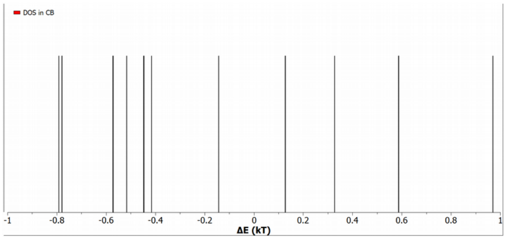	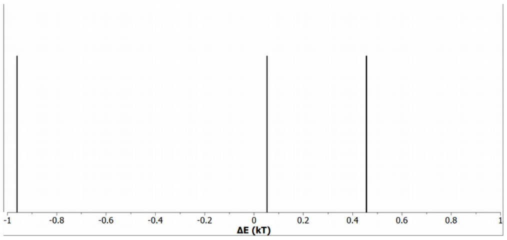
1.85	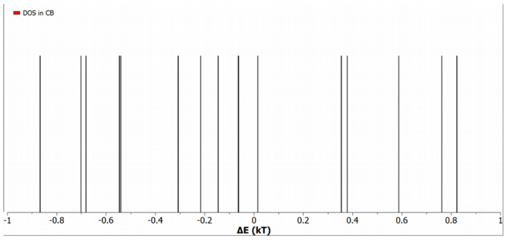	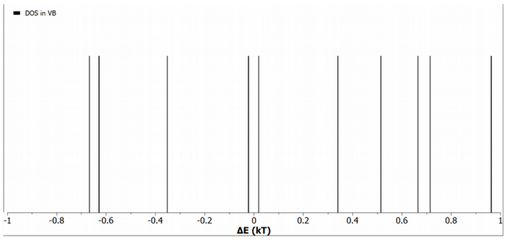
2.03	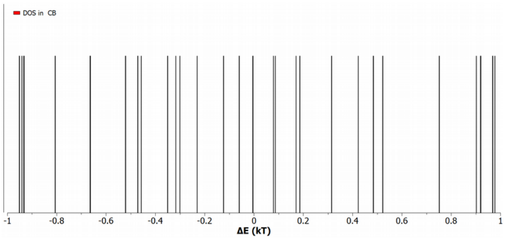	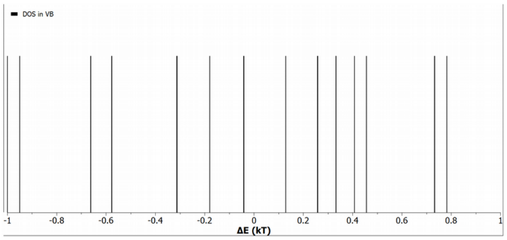
2.17	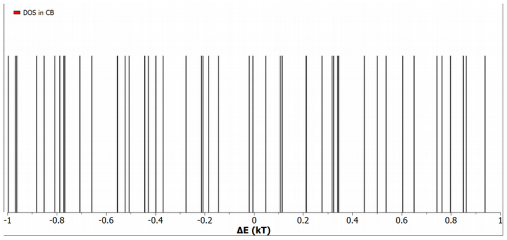	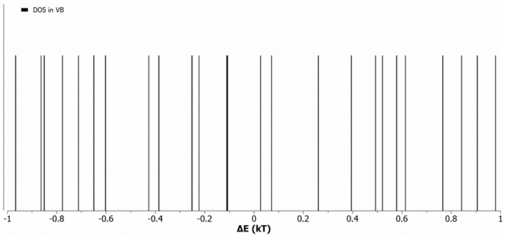

Fig. 4.1 Density of states (DOS) around the state of band gap above (below) the conduction (valence) band edge in various sizes of CdSe QD. ΔE in each graph indicates the energetic difference (in kT) of a given state from the resonance energy. The figures are plotted by SciDAVis.[24]

Table 4.3 The Comparison of the Log-Log slopes between the Different Calculated Auger Lifetime in the literature

Semiconductor	Calculation method	Log-Log slope of the Auger lifetimes		Range of radius (nm)	Reference
Si	Tight-binding	T^+	4.95[2]	1.10 – 2.00	Delerue *et al.*[6]
		T^-	8.25[2]		
CdSe	Effective-mass	T^-	6.5[3]	1.20 – 8.00	Vaxenburg *et al.*[7]
CdSe	Tight-binding	T^+	6.44 – 18.7[4]	1.76 – 2.41	This dissertation
		T^-	7.17 – 8.53[4]		
		BX	7.89 – 11.5[4]		

1. T+ denotes a positive trion, T- denotes a negative trion, and BX denotes a biexciton
2. Deduced from the data reported by Delerue *et al.*[6]
3. The single-molecule result in Vaxenburg *et al.*[7].
4. The radii of the QDs are the original radii.

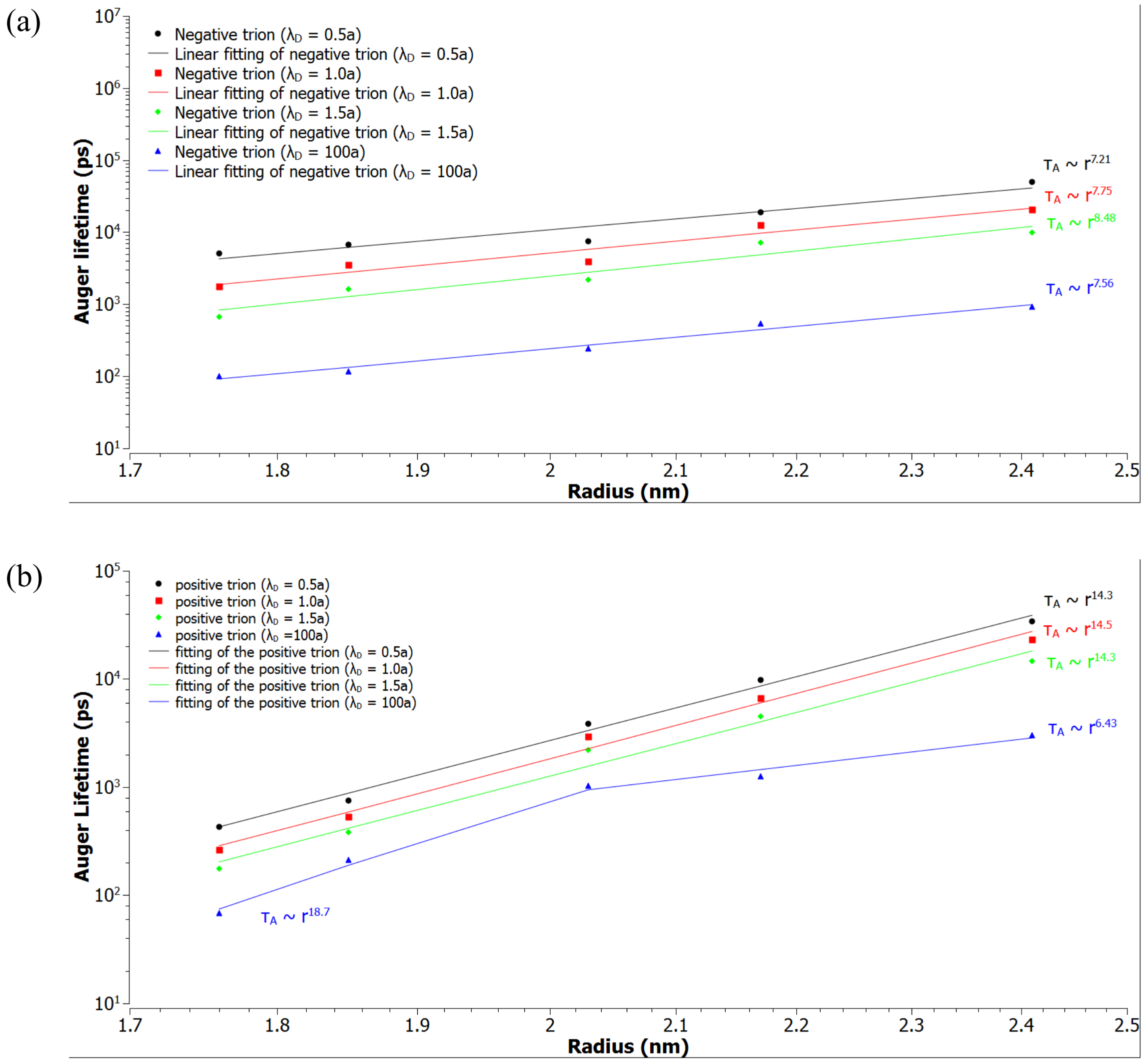

Fig. 4.2 The log-log plots of the Auger lifetimes of (a) the negative trion, and (b) the positive trion for various sizes of CdSe QDs at different Debye shielding lengths (λ_D). The figures are plotted by SciDAVis.[24]

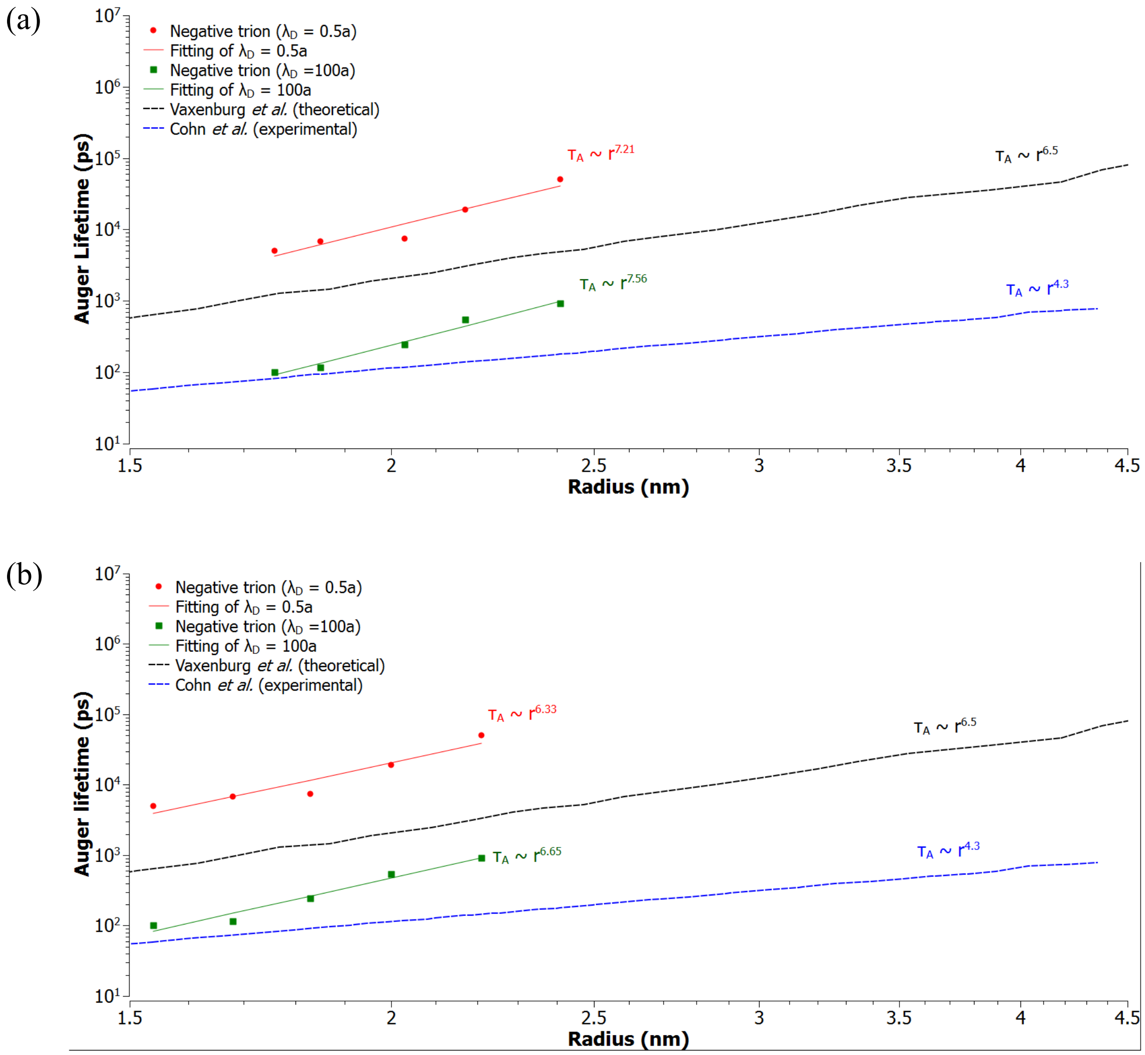

Fig. 4.3 The comparison of the Auger lifetimes of a negative trion between theoretical and experimental results. The results contains the QD sizes of (a) the original radii and (b) one-monolayer less than the original radii. For the case of λ_D = 100a (olive squares), the point away from the other four points, namely the point around 1.85 nm in (a) or around 1.7 nm in (b), was not considered in the linear fitting of the slope. The figures are plotted by SciDAVis.[24]

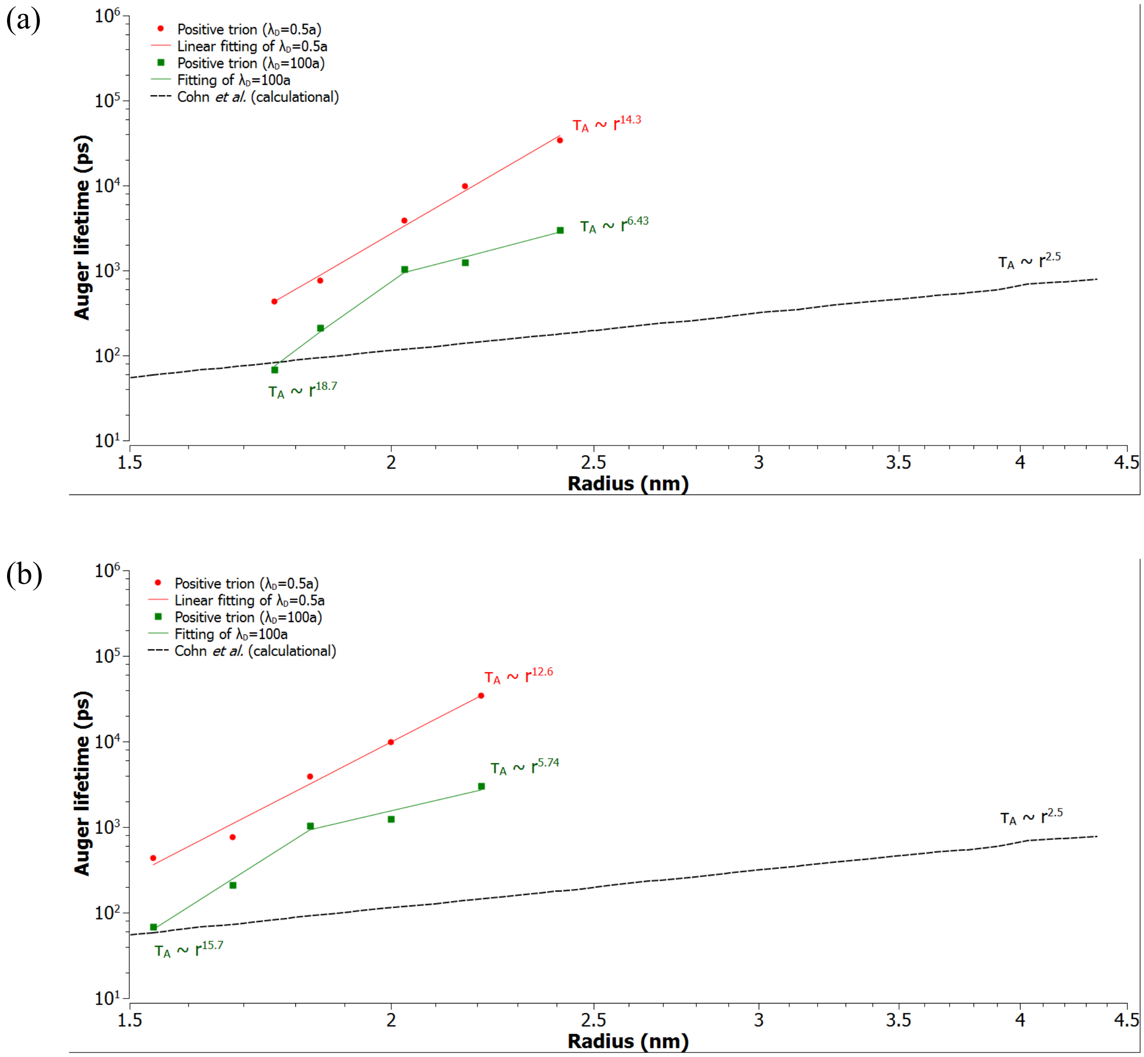

Fig. 4.4 The comparison of the Auger lifetimes of a positive trion between theoretical and experimental results. The results contain the QD sizes of (a) the original radii and (b) one monolayer less than the original radii. The figures are plotted by SciDAVis.[24]

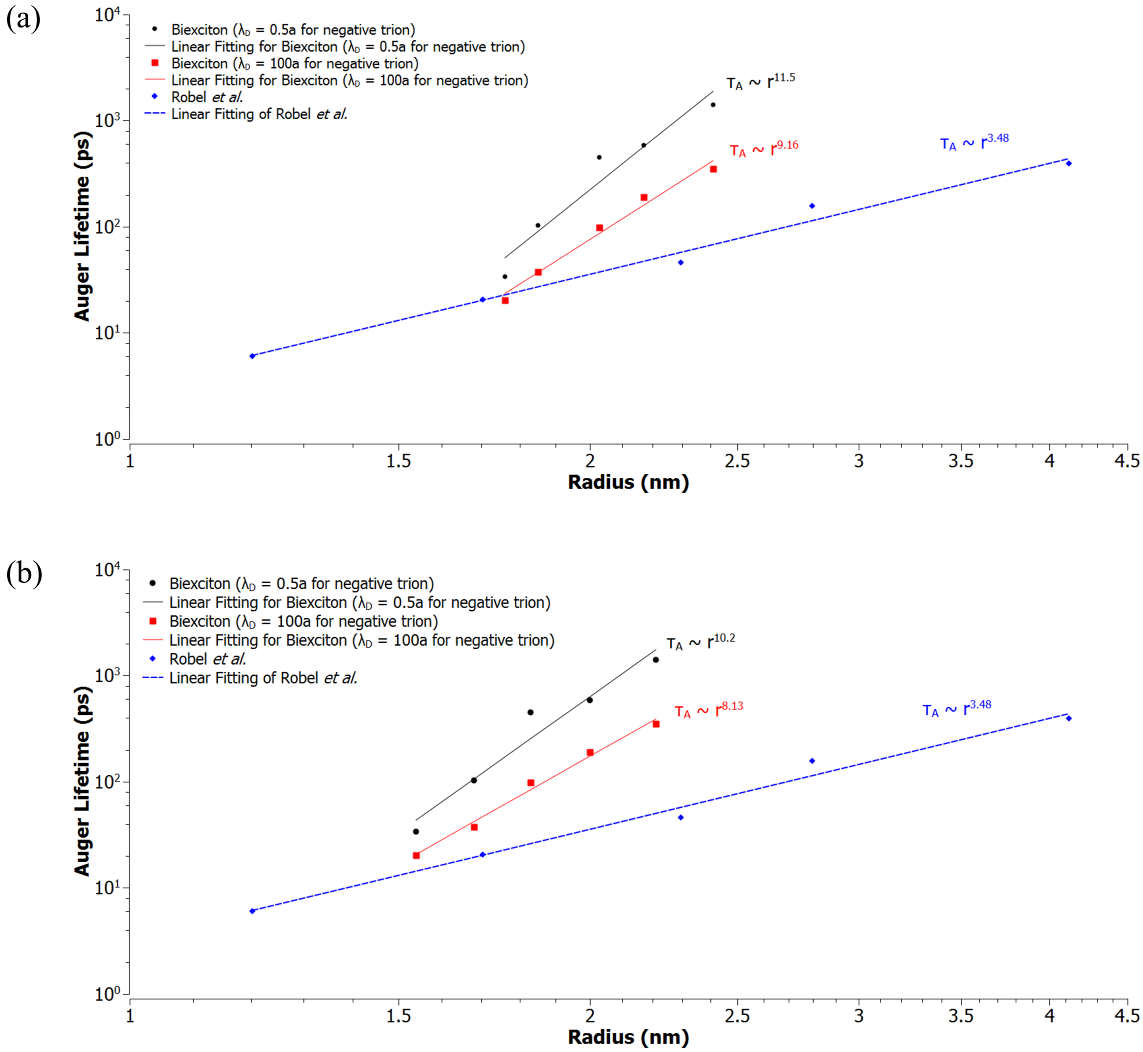

Fig. 4.5 The comparison of the Auger lifetimes of a biexciton between the calculated and experimental[3] results. The results contain the QD sizes of (a) the original radii and (b) one-monolayer less than the original radii. The figures are plotted by SciDAVis.[24]

Table 4.4 The size dependence of the ratio of the Auger lifetime ($\lambda_D = 100a$) of a positive trion to that of a negative trion.

Radius (nm)	Auger lifetime of positive trion, $\tau_A^{T^+}$, (ps)	Auger lifetime of negative trion, $\tau_A^{T^-}$, (ps)	$\tau_A^{T^+} / \tau_A^{T^-}$
1.76	68.500	100.38	0.68
1.85	212.10	116.60	1.82
2.03	1029.6	242.89	4.24
2.17	1252.2	544.80	2.30
2.41	3006.4	914.14	3.29

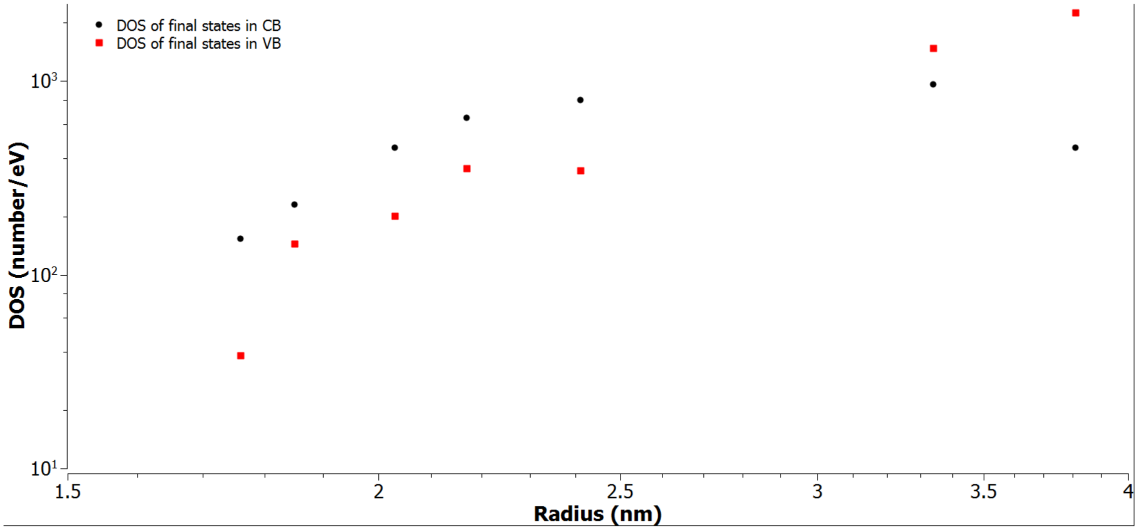

Fig. 4.6 The log-log plot of the size dependence of the density of states (DOS) around the state one-band-gap above the edge of CB (black circle) and the state one-band-gap below the edge of VB (red squares). The figure is plotted by SciDAVis.[24]

Chapter 5

Summary and Perspectives

Summary

This dissertation used the concept of the symmetry-adapted linear combination (SALC)[1] of atomic orbitals to construct various sizes of Wurtzite[2] CdSe quantum dots (QDs). The electronic wave functions of those constructed CdSe QDs were obtained by direct diagonalization[3] of the tight-binding (TB) Hamiltonian[4,5,6] of the whole dots. Modifications have been made to the original TB method to meet the author's need for the calculation of Auger rates in the QDs, and the details are given in Chapter 2.

The calculated QDs and their electronic wave functions were used to calculate the basic properties of QDs, such as the structure, the dipole moment, the electronic band gap, the molecular orbitals (MOs), the density of states (DOS), and the absorption spectrum, as discussed in Chapter 3. The comparison of the above calculated results and the literature, including both experimental[7,8] and theoretical[5-6,9,10,11] findings, suggested that the calculated wave functions in this dissertation can be considered as reliable.

In Chapter 4, the size dependence of the Auger process of negative trion, positive trion and biexciton were calculated using the calculated TB wave functions. In this dissertation, the nature of the TB wave functions was set to terminate at the boundary of QDs, while the other reference[11], using an effective-mass-approximation (EMA) other than an atomistic treatment, allowed the wave functions to extend beyond the boundary. This restriction on the TB wave functions could be one of the sources of the discrepancy between the calculated results and experimental[12] findings, in both the size dependence of the Auger lifetimes and the absolute values of lifetimes. Although the calculation settings in Chapter 4 didn't reproduce the experimental results[12], the *ad doc* approach of reducing the effective radii of QDs pointed out a potential path to improve the calculation methodology, as discussed before. The second route to be explored for the Auger computation involves a surface state mechanism[13].

Perspectives

To improve the calculated results of the Auger process in Chapter 4, modifications to the TB wave functions, especially to the excited electrons, to allow them extend outside the boundary of QDs, such as adding a layer of shell outside the core of a QD, is necessary so the calculation setting would be closer to reality. Moreover, the multipole expansion used in Chapter 4 only considered the leading term, while the multipole expansion in Vaxenburg *et al.*'s work[11] in their effective mass study contained up to 36 terms. Therefore, including the contribution from higher-order terms to the current Auger matrix elements is a focus of future TB studies.

The calculation method mentioned in Chapter 4 can be further applied to the study of other types of Auger process occurred in semiconductor QDs, listed as follows:

I. the Auger-based trapping and “detrapping” processes in semiconductor QDs

The specific Auger-type processes of trapping and “detrapping” mentioned in Chapter 1 were proposed in an article by Marcus[14]. These two processes are involved in the transition from a light state to a dark state, and the restoration of a light state from a dark state[14]. The calculation of the Auger rate could help us understand the detailed dynamics of the QD blinking.

II. the Suppression of Blinking due to in CdZnSe/ZnSe QDs

The suppression of blinking was reported by Wang *et al.*[15] in CdZnSe/ZnSe QDs. By controlling the deposition process and the processing temperature, a layer of alloy was able to form, and the sharp boundary was able to blur between the core and shell in the typical QDs.[15] Wang *et al.* suggested that the smoothly changing potential of confinement due to the blurring of the boundary significantly reduces the chance of the Auger process because the conservation of the momentum is hard to achieve[14]. A further explanation to this phenomenon was provided by Cragg and Efros[16] with a one-dimensional model. On the other hand, however, the calculation of the Auger rate could provide a three-dimensional atomistic perspective to understand the role of the composition-gradually-changed shell in reducing the Auger rate.

III. the B-type Blinking Occurrence in the Giant QDs of CdSe/CdS

The “B-type blinking” is observed in Galland *et al*.'s study in CdSe/CdS giant QD (g-QD)[16]. The distinction between the B-type blinking and the typical blinking (or referred as the A-type blinking in Galland *et al.*'s work[17]) is the lifetime: the lifetime of the B-type blinking (around 15 ns) is longer than that of the A-type blinking (around 5 ns). Although the lifetime of B-type blinking is comparable to that of a light state (the fluorescent state), its photoluminescence (PL) intensity is only about ¼ of a light state. Moreover, the B-type blinking was significant suppressed when the thickness of the CdS shell increased from 7 monolayers (MLs) to 15 MLs[17]. Galland *et al.* proposed a model of electron trapping to explain the phenomona.[17] The calculation of the Auger lifetimes for the both A-type and B-type blinking could help explain Galland *et al.*'s proposed model[17] in more molecular-level detail.

Reference

1. Cotton, F. A., *Chemical applications of group theory.* 3rd ed.; Wiley: New York, 1990; p xiv, 461 p.
2. Shim, M.; Guyot-Sionnest, P., Permanent dipole moment and charges in colloidal semiconductor quantum dots. *J Chem Phys* **1999,** *111* (15), 6955-6964.
3. Lippens, P. E.; Lannoo, M., Calculation of the band gap for small CdS and ZnS crystallites. *Phys Rev B* **1989,** *39* (15), 10935.
4. Vogl, P.; Hjalmarson, H. P.; Dow, J. D., A Semi-Empirical Tight-Binding Theory of the Electronic-Structure of Semiconductors. *J Phys Chem Solids* **1983,** *44* (5), 365-378.
5. Lippens, P. E.; Lannoo, M., Comparison between Calculated and Experimental Values of the Lowest Excited Electronic State of Small Cdse Crystallites. *Phys Rev B* **1990,** *41* (9), 6079-6081.
6. Albe, V.; Jouanin, C.; Bertho, D., Confinement and shape effects on the optical spectra of small CdSe nanocrystals. *Phys Rev B* **1998,** *58* (8), 4713-4720.
7. Katari, J. E. B.; Colvin, V. L.; Alivisatos, A. P., X-ray Photoelectron Spectroscopy of CdSe Nanocrystals with Applications to Studies of the Nanocrystal Surface. *J Phys Chem* **1994,** *98* (15), 4109-4117.
8. Murray, C. B. Synthesis and characterization of II-IV quantum dots and their assembly into 3D quantum dot superlattices. Massachusetts Institute of Technology, 1995.
9. Pokrant, S.; Whaley, K., Tight-binding studies of surface effects on electronic structure of CdSe nanocrystals: the role of organic ligands, surface reconstruction, and inorganic capping shells. *Eur Phys J D -Atomic, Molecular, Optical and Plasma Physics* **1999,** *6* (2), 255-267.
10. Kilina, S. V.; Craig, C. F.; Kilin, D. S.; Prezhdo, O. V., Ab Initio Time-Domain Study of Phonon-Assisted Relaxation of Charge Carriers in a PbSe Quantum Dot. *J Phys Chem C* **2007,** *111* (12), 4871-4878.
11. Vaxenburg, R.; Rodina, A.; Shabaev, A.; Lifshitz, E.; Efros, A. L., Nonradiative Auger Recombination in Semiconductor Nanocrystals. *Nano Lett* **2015,** *15* (3), 2092-2098.
12. Cohn, A. W.; Rinehart, J. D.; Schimpf, A. M.; Weaver, A. L.; Gamelin, D. R., Size Dependence of Negative Trion Auger Recombination in Photodoped CdSe Nanocrystals. *Nano Lett* **2014,** *14* (1), 353-358.
13. Beane, G. A.; Gong, K.; Kelley, D. F., Auger and Carrier Trapping Dynamics in Core/Shell Quantum Dots Having Sharp and Alloyed Interfaces. *Acs Nano* **2016,** *10* (3), 3755-3765.
14. Marcus, R. A., Interaction of theory and experiment: examples from single molecule studies of nanoparticles. *Philos T R Soc A* **2010,** *368* (1914), 1109-1124.
15. Wang, X.; Ren, X.; Kahen, K.; Hahn, M. A.; Rajeswaran, M.; Maccagnano-Zacher, S.; Silcox, J.; Cragg, G. E.; Efros, A. L.; Krauss, T. D., Non-blinking semiconductor nanocrystals. *Nature* **2009,** *459* (7247), 686-689.
16. Cragg, G. E.; Efros, A. L., Suppression of Auger Processes in Confined

Structures. *Nano Lett* **2010,** *10* (1), 313-317.
17. Galland, C.; Ghosh, Y.; Steinbruck, A.; Sykora, M.; Hollingsworth, J. A.; Klimov, V. I.; Htoon, H., Two types of luminescence blinking revealed by spectroelectrochemistry of single quantum dots. *Nature* **2011,** *479* (7372), 203-207.